

LTE Transmit Diversity Techniques using Software-Defined Radios

Gerardo Moreno-Crespo

School of Electrical Engineering

Thesis submitted for examination for the degree of Master of
Science in Technology.

Espoo 13.02.2017

Thesis supervisor:

Prof. Riku Jäntti

Thesis instructor:

D.Sc. (Tech.) Kalle Ruttik

Author: Gerardo Moreno-Crespo

Title: LTE Transmit Diversity Techniques using Software-Defined Radios

Date: 13.02.2017

Language: English

Number of pages:8+67

School of Electrical Engineering

Department of Communication and Networking Technologies

Professorship: Communication Engineering

Code: S-72

Supervisor: Prof. Riku Jäntti

Instructor: D.Sc. (Tech.) Kalle Ruttik

This thesis presents a simple software-defined radio implementation of an LTE FDD testbed that employs two transmit antennas at the eNB for the purpose of achieving transmit-diversity BER performance benefits at the UE side. The testbed uses a pair of USRP N210 remote radio heads (RRH) which include an RF board and a digital-front-end (DFE). The RRHs are connected to a Linux computer, via ethernet, which does all the post-processing and decodes the raw IQ samples from the DFE output. We've provided a detailed description of the downlink physical layer LTE procedures performed inside the Linux computer, in order to assess the BER rate at the receiving end. To validate our platform and compute the BER curves, we've created two different test environments in the lab at Aalto ComNet: 1) under static channel conditions and 2) under multipath rich environment. For the static channel test environment, BER measurement results were collected inside an RF Anechoic chamber, where the wireless channel is essentially multipath fading free, thus BER diversity benefits were not attained. Under multipath rich channel environment, we created a multipath-induced channel in the lab and computed BER curves. For this latter case, BER performance benefits were achieved and the details are included in Chapter 6.

Keywords: Software-Defined Radio, LTE, FDD, MIMO, Transmitter Diversity, USRP

Acknowledgement

Para mis padres Gerardo e Iliana.

I want to deeply thank the Comnet Team at Aatlo: Jussi, Anil, Tewodros, Vishnu, Yihenew, Chen, Kalle, and Riku.

List of Figures

1	Multi-carrier system with non-overlapping channels	2
2	Multi-carrier system with overlapping channels	3
3	Multi-carrier system with overlapping sync pulses	4
4	OFDM system with IFFT/FFT implementation	5
5	BER for QPSK in AWGN, Rayleigh fading, and Rician fading	9
6	Receiver Diversity Model	11
7	The Alamouti transmit diversity scheme of a 2x1 wireless communication system	13
8	System diagram for 2x2 MIMO	15
9	BER comparison of diversity techniques in Rayleigh flat-fading channels	17
10	BER comparison of diversity techniques in Rician flat-fading channels	18
11	BER performance of the 2x2 Alamouti scheme in Rayleigh and Rician flat-fading channels	19
12	System architecture for LTE network	23
13	2x1 MISO LTE downlink testbed block diagram	25
14	FDD 10 millisecond frame	26
15	Downlink physical channels frequency-domain processing	27
16	BPSK, 16-QAM, and 64-QAM I-Q mapping	28
17	Time-frequency resource grid corresponding to one subframe	30
18	Mapping of different physical signals onto the time-frequency grid	31
19	The OFDM baseband signal generation procedure	33
20	Example of a Zadoff-Chu sequence with root index = 29	35
21	Length-31 Gold code structure used for generation of cell-specific reference signals	37
22	Length-31 Gold code structure used for generation of cell-specific reference signals	38
23	Cell-specific reference signal mapping for transmit diversity using 2 antennas	39
24	Definition of channel bandwidth and transmission bandwidth configuration for one E-UTRA carrier [1]	40
25	Transmission bandwidth adjustments due to the actual sampling rates defined in Table 4.	41
26	MISO LTE receiver testbed block diagram	42
27	MISO LTE receiver testbed setup with RF anechoic chamber	43
28	VSWR of the 3 dBi vertical antennas used in our setup	44
29	Block diagram of the time-domain processing at the receiver	44
30	Magnitude of the PSS correlation plot for received samples with antenna transmission timing mismatch	46
31	Magnitude of the PSS correlation plot for received samples with antenna transmission timing mismatch compensated	46
32	Block diagram of the frequency-domain processing at the receiver	47
33	Frequency and time domain linear interpolation procedure for pilot-based channel estimation [2]	49

34	Channel coefficient estimates for tx antenna 1 and tx antenna 2 using reference pilots when the SNR is approximately 10 dB	50
35	Instantaneous SNR, in terms of γ_b , captured over the first 5 seconds during the BER measurements	53
36	BER measurements results of the MISO system depicted in Figure 26	54
37	MISO multipath setup inside Comnet Laboratory	56
38	The picture on the right hand shows a sketch of the setup used during the measurements. The pictures on the left show the transmit antennas with the rotating metallic sheets (bottom) and the receive antenna (top)	57
39	Rapidly fading time-selective channel [3]	58
40	Magnitude of the channel coefficient estimates for tx antenna 1 and tx antenna 2 when the average SNR of the data is approximately 12 dB	59
41	Instantaneous SNR, in terms of γ_b , for the SISO case using transmit antenna 1	60
42	Instantaneous SNR, in terms of γ_b , for the SISO case using transmit antenna 2	60
43	Instantaneous SNR, in terms of γ_b , for the MISO case	61
44	BER measurements results of the multipath fading setup depicted in Figures 37 and 38	62

List of Tables

1	Comparison between LTE SFBC and the Alamouti diversity technique	29
2	Allowable channel bandwidth configurations	29
3	CP length for different channel bandwidth configurations	34
4	Sampling rate supported by the USRP N200 when the DUC interpolation factor is a multiple of 4.	41

List of Abbreviations

3G	Third Generation
3GPP	Third Generation Partnership Project
4G	Fourth Generation
API	Application Programming Interface
ARQ	Automatic Repeat Request
AWGN	Additive White Gaussian Noise
BER	Bit Error Rate
BS	Base Station
CAZAC	Constant-Amplitude, and Zero Auto-Correlation
CIC	Cascaded Integrator-Comb
CoP	Control Plane
CoMP	Coordinated Multi-Point
CP	Cyclic Prefix
CSI	Channel State Information
DC	Direct Current
DFT	Discrete Fourier Transform
DUC	Digital Up-Conversion
eNodeB	Evolved Node B
EPC	Evolved Packet Core
EPS	Evolved Packet System
EUTRAN	Evolved Universal Terrestrial Radio Access Network
FDD	Frequency Division Duplexing
FFT	Fast Fourier Transform
GSM	Global System for Mobile Communications
HB	Half-Band
HSDPA	High-Speed Downlink Packet Access
HSS	Home Subscriber Server
HSUPA	High-Speed Uplink Packet Access
ICI	Inter-Carrier Interference
IFFT	Inverse Fast Fourier Transform
I-Q	In-Phase and Quadrature
IMT-2000	International Mobile Telecommunication - 2000
IMT-A	International Mobile Telecommunication - Advanced
IP	Internet Protocol
ISI	Inter-Symbol Interference
ITU	International Telecommunication Union
ITU-R	ITU Radio
LO	Local Oscillator
LOS	Line-of-Sight
LTE	Long-Term Evolution
MAC	Medium Access Control
MGF	Moment Generating Function
MIMO	Multiple-Input, Multiple-Output

MISO	Multiple-Input, Single-Output
ML	Maximum-Likelihood
MME	Mobile Management Entity
MMSE	Minimum Mean Square Error
MRRC	Maximal-Ratio Receiver Combining
OFDM	Orthogonal Frequency Division Multiplexing
OFDMA	Orthogonal Frequency Division Multiple Access
PCC	Policy and Charging Control
PCRF	Policy and Charging Resource Function
PDCP	Packet Convergence Protocol
PDF	Probability Density Function
P-GW	Packet Data Network Gateway
PSD	Power Spectral Density
PSS	Primary Synchronization Signal
QAM	Quadrature Amplitude Modulation
QoS	Quality-of-Service
QPSK	Quadrature Phase Shift Keying
RAN	Radio Access Network
RE	Resource Element
RF	Radio Frequency
RLC	Radio Link Control
RRC	Radio Resource Control
RRM	Radio Resource Management
SAE	System Architecture Evolution
SC-FDMA	Single-Carrier Frequency Division Multiple Access
SDR	Software Defined Radio
SFBC	Space-Frequency Block Coding
SFTD	Space-Frequency Transmit Diversity
S-GW	Serving Gateway
SISO	Single-Input, Single-Output
SMA	SubMiniature version A
SNR	Signal-to-Noise Ratio
S/P	Serial-to-Parallel
SSS	Secondary Synchronization Signal
TDD	Time Division Duplexing
TR	Technical Report
TSG	Technical Specification Group
UE	User Equipment
UHD	Universal Hardware Driver
UP	User Plane
USRP	Universal Software Radio Peripheral
VSWR	Voltage Standing Wave Ratio
WiFi	"Wireless Fidelity" (IEEE 802.11)
WCDMA	Wideband Code Division Multiple Access

1 Introduction

Historically, wireless solutions are meant and designed for a specified purpose - data, voice, video, broadcasting, command and control, or emergency response communications. Typically, once the final product makes it to the market or reaches its final design iteration, it can only deliver the capabilities and performance dictated by its original design goals. Enhancing the performance or extending to new capabilities typically requires new hardware and, in the worst-case, a fresh design cycle.

Software defined radio (SDR) technology aims to bring flexibility, cost-efficiency, and power-efficiency to the design and implementation of wireless solutions by offering these benefits with low or zero need of physical hardware intervention. It does so primarily by implementing some of all of the physical layer functionalities in a flexible and configurable way such that the same hardware can be repurposed to enhance performance, extend wireless capabilities, or offer a completely different wireless solution (e.g. LTE/WiFi).

1.1 Thesis objective

The objective of this thesis work is to demonstrate the implementation of a multiple-transmit antenna LTE testbed using USRP N200 software defined radios and demonstrate its performance in line-of-sight (multipath free) and multipath rich environments.

1.2 Thesis organization

This thesis is divided in the following way:

- **Chapter 1** Introduction
- **Chapter 2** Description of OFDM communications and BER performance formulation for Rician and Rayleigh Flat-Fading Channels .
- **Chapter 3** Brief description on MIMO techniques. Emphasis on transmitter and receiver diversity schemes. MMSE and Alamouti's transmit diversity techniques described. BER performance curves also included in the chapter.
- **Chapter 4** Overview of the LTE Testbed using the USRP Hardware. Chapter describes the physical channels processing procedures.
- **Chapter 5** This chapter describes and presents the BER measurement results of the MISO LTE Receiver Testbed inside an RF Anechoic Chamber.
- **Chapter 6** This chapter describes and presents the BER measurement results of the MISO LTE Receiver Testbed in a multipath-fading-induced environment.
- **Chapter 7** Concluding remarks and future research directions.

2 OFDM Communications

2.1 Multi-Carrier Modulation

A typical multi-carrier modulated signal with all the sub channels summed together to form the transmitted signal is given by,

$$\mathbf{s}(t) = \sum_{i=0}^{N-1} s_i g(t) \cos(2\pi f_i t + \phi_i) \quad (2.1)$$

where s_i is the complex modulated symbols associated with the i th subcarrier whose phase offset is denoted by ϕ_i . Each symbols s_i is transmitted at a rate of R/N bits per second yielding an occupied subchannel bandwidth of B_N . With such configuration of subchannel bandwidths, subcarriers can be separated by $f_i = f_0 + \frac{i}{T_N}$, $i = 0, \dots, N$ where $T_N = (1 + \beta)/B_N$. The term $g(t)$ is generally a narrowband raised cosine pulse shaping filter with roll-off factor β .

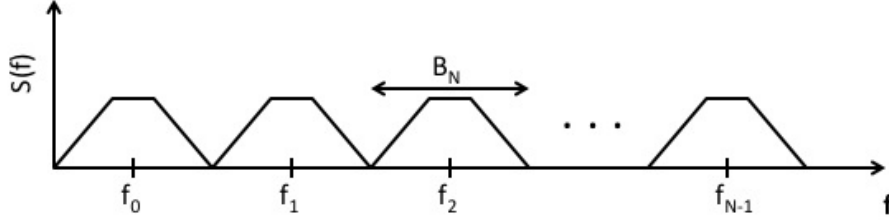


Figure 1: Multi-carrier system with non-overlapping channels

The frequency spectrum associated with equation (2.3) is shown in Figure 1. The idea is that each narrowband subcarrier is much smaller than the coherence bandwidth of the channel so $B_N \ll B_C$, where B_C is coherence bandwidth of the channel. If this condition holds, each subchannel experiences relatively flat fading and consequently, the Inter-symbol Interference (ISI) on each subchannel is small.

Although this system could be used to mitigate channel-induced ISI, each subchannel in a realistic implementation will occupy a larger bandwidth because the pulse shaping must be time limited. In fact, in a realistic implementation the subchannels are separated by $(1 + \beta + \epsilon)/T_N$, where the band penalty for having time limited shaping filters extends to total bandwidth by $\epsilon N/T_N$. Using this form of multi-carrier modulation with non-overlapping channels can bring some benefits to combat frequency-selective channels yet it can be spectrally inefficient when it comes to the implementation.

2.1.1 Orthogonal Frequency-Division Multiplexing (OFDM)

One way to efficiently utilise the spectrum while maintaining robustness against ISI is to use orthogonal subcarriers that have overlapping bandwidths. The frequency spectrum of a system with this property is shown in Figure 2.

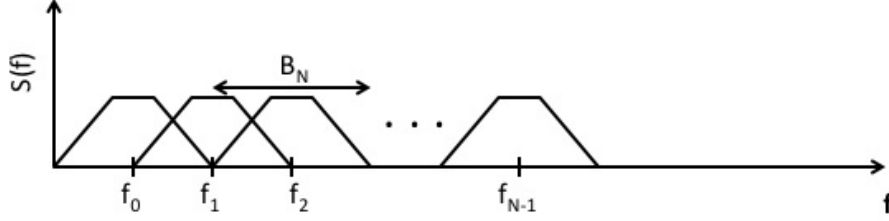


Figure 2: Multi-carrier system with overlapping channels

The basic premise of using orthogonal overlapping channels is to efficiently utilise the frequency spectrum while the orthogonality permits the coexistence of all the subbands in an overall shorter bandwidth. The overlapping of the subchannels works due to the fact that a set of orthogonal basis functions with frequencies f_i and f_j with $i \neq j$ yield a zero product when multiplied to each other so they can be separated out by the demodulator at the receiver. To be more specific, let the subcarriers $\{\cos(2\pi(f_0 + i/T_o)t + \phi_i), i = 0, \dots, N-1\}$ form a set of orthogonal basis functions over the interval $[0, T_o]$ for any given phase offset ϕ_i . So they are orthogonal basis function because,

$$\int_0^{T_o} \cos(2\pi(f_0 + i/T_o)t + \phi_i) \cos(2\pi(f_0 + j/T_o)t + \phi_j) dt = 0 \quad (2.2)$$

The implementation with this form of overlapping orthogonal subcarriers makes it feasible to add some flexibility to the pulse shaping filters with longer transition time to converge to zero. Generally, a set of sinc pulses can be used to generate the overlapping bandwidths where the separation between each pulse is $1/T_o$ (see Figure 3). Recall that a sinc pulse, $p(f) = \sin(\pi f T_o) / \pi f T_o$, follows the Nyquist criteria for zero ISI where $p(0) = 1$ and $p(n/T_o) = 0$ for all possible values of n [4]. Therefore, a train of sinc pulses separated by $1/T_o$ can contain information of every subcarrier at the centre of the pulse with no interference from any of the other pulses. Naturally, some time limitations still affect some of the subcarriers at the edges where sharp discontinuities can lead to an excess bandwidth of ϵ/T_o . However, if the number of subcarriers is kept relatively large, this excess bandwidth adds a negligible effect to the total system bandwidth. Also note that a sinc pulse located at DC is conventionally not used in order to avoid any unwanted artefacts at the DC level when demodulating.

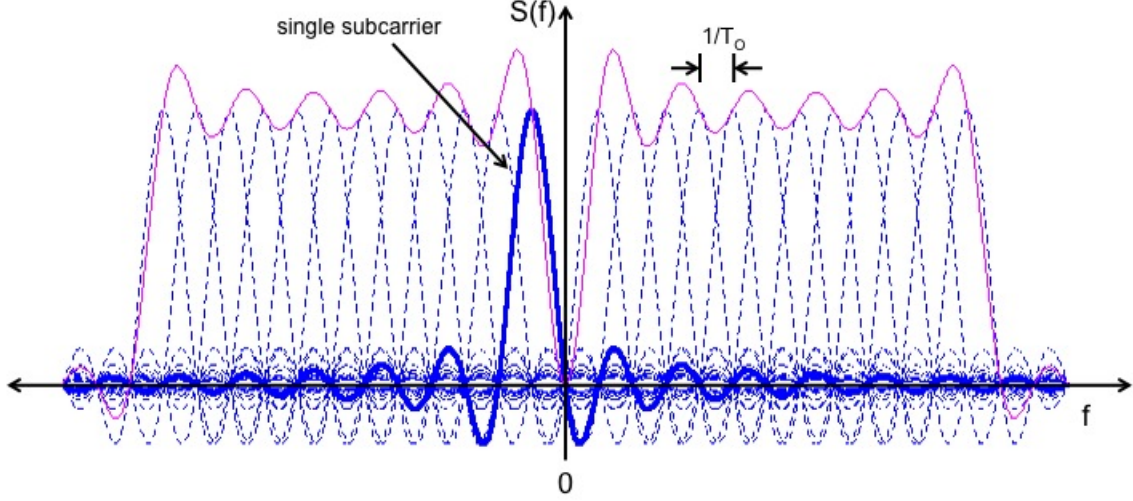


Figure 3: Multi-carrier system with overlapping sinc pulses

An OFDM system is generally done in hardware using a fast Fourier transform (FFT) which is the practical implementation of the discrete Fourier Transform (DFT). However, since the subcarriers need to be placed orthogonally to each other and then converted to time samples, an inverse FFT (IFFT) is used at the transmitter and the decoupling of the subcarriers is performed by an FFT at the receiver. An IFFT/FFT OFDM system is shown in Figure 4. The IFFT operation is performed by,

$$\mathbf{x}[n] = \frac{1}{\sqrt{N}} \sum_{i=0}^{N-1} X[i] e^{j2\pi ni/N}, \quad 0 \leq n \leq N-1 \quad (2.3)$$

The sequence $\mathbf{x}[n]$ corresponds to the time domain discrete representation of the subcarriers $X[0], X[1], \dots, X[N-1]$ where each subcarrier can be represented by the center sample in the sinc pulse shown in Figure 3. So, if we have signal with a rate of R bps and bit duration of $1/R$ seconds, such signals must be sampled at a rate of at least $2R$ samples per second in order to not violate the Nyquist sampling rate. The IFFT operation provides N number of samples where each sample has a rate of R_o , so $NR_o = R$. At first glance it may seem that having only N samples in $\mathbf{x}[n]$ may violate Nyquist sampling rate, however, it should be pointed out that each sample is in complex form, with both real and imaginary parts having their own rate R_o . Therefore, Nyquist sampling criteria is satisfied since the sequence $\mathbf{x}[n]$ has actually $2NR_o$ samples for an input rate R .

The transmitter block diagram depicted in Figure 4 shows the need to append a cyclic prefix (CP) before the parallel-to-serial (S/P) conversion of the time samples. This CP operation is added to each OFDM symbol where an OFDM symbol is represented by the sequence $\mathbf{x}[n]$. Appending the CP is required since the signal $s(t)$ bearing OFDM processed data is linearly convoluted with channel impulse response, $h(n)$. The linearly convoluted output from the channel can be turned into a circular convolution by appending a group of $\mathbf{x}[N-\mu], \dots, \mathbf{x}[N-1]$ samples from $\mathbf{x}[n]$ at

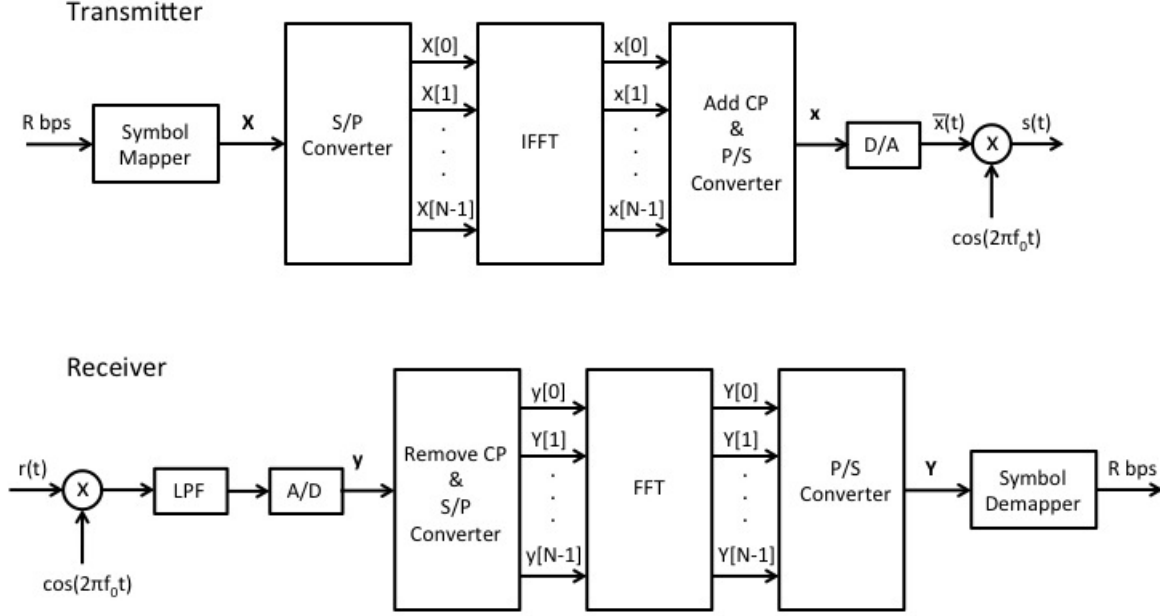


Figure 4: OFDM system with IFFT/FFT implementation

the beginning of output sequence provided after the S/P operation. By inducing circular convolution of the input and the channel impulse response, and provided that $h[n]$ is known at the receiver, then the original sequence can be recovered using the IFFT/DFT combination described in Figure 4 [5]. Moreover, the cyclic prefix adds an important defence mechanism against ISI because the first μ samples of an OFDM symbol are prone to ISI from previous OFDM symbols. Yet the CP samples are discarded before the FFT operation at the receiver and not used to demodulate the original data.

2.2 Channel Model

OFDM systems are designed such that the CP appended to the beginning or end of an OFDM symbol can effectively mitigate the detrimental effects of channel-induced ISI distortion and the need of a time equalizer at the receiver to remedy such effects is not necessary [7], [8]. With this assumption, the baseband mathematical expression for the received signal at time t , can be described by the equation,

$$r(t) = h(t)s(t) + w(t) \quad (2.4)$$

where $h(t)$ represents the channel response (or fading parameter), $s(t)$ the transmitted signal, and $w(t)$ accounts for receiver noise. Before transmission, information

bits contained in $s(t)$ are mapped into a set of M constellation points and then phase-shift keying modulated. For simplicity, we restrict our analysis to QPSK modulation and note that generalizing our analysis to higher modulation schemes requires slight modifications to the mathematical formulations to be presented later in this section.

In order to characterise the flat-fading multipath fading effects experienced in the channel, there are two channel models typically used in the analysis of wireless communications system: the Rayleigh and the Rician fading model [10], [6].

The Rician fading channel model is often used when the received signal is composed of multiple reflective paths plus a significant line-of-sight (non-fading) component. This line-of-sight (LOS) component is referred to as the specular component and is typically described in terms of a fading parameter K , defined by

$$K = \frac{a_0^2}{2\sigma_{mp}^2} \quad (2.5)$$

where K represents the ratio of the power of the specular component to the power of the multipath components. The multipath components of the Rician channel response are generally considered to be a complex Gaussian random process with zero mean and variance σ_{mp} per dimension.

Rayleigh fading results from having no specular component in the received signal; hence, the received signal is strictly composed of multipath components arriving at different phases and different signal strengths. This type of fading typically accounts for the worst case flat-fading channel and can be obtained from the Rician fading distribution when K approaches zero (i.e. $a_0^2 = 0$) [10]. Just like the Rician channel, the multipath components in the channel response are generally considered to be a complex Gaussian random process with zero mean and variance σ_{mp} per dimension.

Last but not least, the noise component $w(t)$ in (2.4) represents receiver noise and it is typically defined as additive white Gaussian noise (AWGN) with zero mean and variance $N_o/2$ where N_o is the one-sided noise power spectral density (PSD).

2.2.1 BER Performance in Flat-Fading Channels

Bit error rate (BER) is one of the most important performance metrics used to evaluate the end-to-end efficiency of communications systems at the radio link level. We will consider the average probability of bit error rate, \tilde{P}_b , to be the foremost system performance metric when evaluating the systems described later in this chapter. In this section, however, we concentrate on the theoretical formulation of the average bit error rate performance of communication systems under Rayleigh and Rician fading channels. For now on, when referring to the average bit error rate, the word average will be omitted so average bit error rate and bit error rate bear the same

meaning.

In order to compute the probability of bit error due to flat-fading, the integral whose integrand consist of the product of AWGN probability of error and the fading probability density function (PDF) must be evaluated [11]

$$\tilde{P}_b = \int_0^\infty P_b^{AWGN}(\gamma) p_\gamma(\gamma) d\gamma \quad (2.6)$$

The bit error probability of QPSK in AWGN is given by $\tilde{P}_b^{AWGN} = Q(\sqrt{2\gamma})$, however, obtaining a closed-form solution of (2.6) using the conventional Q function expression (equation 4.1 in [11]) is difficult to evaluate. A more attractive form of the Q function is given by equation 4.2 in [11],

$$Q(x) = \frac{1}{\pi} \int_0^{\frac{\pi}{2}} \exp\left(\frac{x^2}{2\sin^2\theta}\right) d\theta \quad (2.7)$$

This form of the Q function can be evaluated at $\sqrt{2\gamma}$ and applied to equation (2.6).

$$\tilde{P}_b = \frac{1}{\pi} \int_0^{\frac{\pi}{2}} \left[\int_0^\infty \exp\left(\frac{-\gamma}{\sin^2\theta}\right) p_\gamma(\gamma) d\gamma \right] d\theta \quad (2.8)$$

Note that the term inside the brackets is in the form of the moment generating function (MGF), $M_\gamma(\gamma)$, which is just the Laplace transform of the distribution $p_\gamma(\gamma)$ with the argument $-1/\sin^2\theta$.

$$\tilde{P}_b = \frac{1}{\pi} \int_0^{\frac{\pi}{2}} M_\gamma\left(\frac{-1}{\sin^2\theta}\right) d\theta \quad (2.9)$$

This form of the average probability of bit error is very useful since it only requires the Laplace transform of the fading distribution being considered evaluated with the argument shown above.

BER Performance of QPSK in Rayleigh Fading

The Rayleigh fading PDF and its Laplace transform are given by equations

$$p_\gamma(\gamma) = \frac{1}{\tilde{\gamma}_b} \exp\left(\frac{-\gamma}{\tilde{\gamma}_b}\right) \quad , \quad \gamma \geq 0 \quad (2.10a)$$

$$M_\gamma(s) = \frac{1}{1 - s\tilde{\gamma}_b} \quad , \quad s > 0 \quad (2.10b)$$

where $\tilde{\gamma}_b$ denotes the average bit energy to noise spectral density ratio, E_b/N_o . If we evaluate (2.10b) with $-1/\sin^2\theta$ and then insert the evaluated expression into (2.9)

we obtain the following,

$$\begin{aligned}\tilde{P}_b &= \frac{1}{\pi} \int_0^{\frac{\pi}{2}} \frac{d\theta}{1 + \frac{\tilde{\gamma}_b}{\sin^2 \theta}} = \frac{\pi}{2} \left[\theta - \sqrt{\frac{\tilde{\gamma}_b}{\tilde{\gamma}_b + 1}} \tan^{-1} \left(\frac{\tan \theta}{\sqrt{\frac{\tilde{\gamma}_b}{\tilde{\gamma}_b + 1}}} \right) \right] \Big|_0^{\frac{\pi}{2}} \\ &= \frac{1}{2} \left(1 - \sqrt{\frac{\tilde{\gamma}_b}{1 + \tilde{\gamma}_b}} \right) \approx \frac{1}{4\tilde{\gamma}_b}\end{aligned}\quad (2.11)$$

caution should be taken when evaluating the integral limits since $\tan(\frac{\pi}{2})$ is undefined, however, taking the appropriate limits makes the evaluation possible. Equation (2.11) is an elegant expression for the average BER probability of QPSK in Rayleigh flat-fading channels. A simplified form of this expression, restricted to high E_b/N_o , is given by $1/4\tilde{\gamma}_b$.

BER Performance of QPSK in Rician Fading

The BER performance of QPSK in Rician fading can be evaluated using the same convention described above. The Laplace transform of the Rician fading PDF is given by equation (5.11) in [11]

$$M_\gamma(s) = \frac{1 + K}{1 + K - s\tilde{\gamma}_b} \exp\left(\frac{Ks\tilde{\gamma}_b}{1 + K - s\tilde{\gamma}_b}\right), \quad s > 0 \quad (2.12)$$

substituting this equation in (2.9) yields,

$$\tilde{P}_b = \frac{1}{\pi} \int_0^{\frac{\pi}{2}} \frac{(1 + K)\sin^2 \theta}{(1 + K)\sin^2 \theta + \tilde{\gamma}_b} \exp\left(\frac{-K\tilde{\gamma}_b}{(1 + K)\sin^2 \theta + \tilde{\gamma}_b}\right) d\theta \quad (2.13)$$

evaluation of equation (2.13) in closed-form is non-trivial so in order to solve the integral, some form of numerical approximation can be employed.

The average probability of BER for QPSK in AWGN, Rayleigh and Rician fading channels is depicted in Figure 5. It can be observed that the BER of Rician fading converges to the BER of Rayleigh fading when K approaches $-\infty$ dB. Similarly, the BER of Rician fading converges to the BER of AWGN when K approaches $+\infty$ dB. For an average BER of 10^{-4} , the required SNR for QPSK in the AWGN channel is roughly 8.4 dB whereas the same performance level is achieved at 34 dB in the worst-case fading environment (Rayleigh channel), so a 25.6 dB increase in transmit power is required to keep up with the non-fading environment and the gap in SNR between the two BER performance curves increases abysmally when the BER is reduced. In Rayleigh fading, the difference on BER between fading and non-fading environments depends on the value of K , which relies on the difference in power between LOS path and the sum of the multipath components. Evidently, the detrimental effects of multipath fading can jeopardize the integrity of any wireless communication system with a weak LOS link. It's imperative to employ efficient

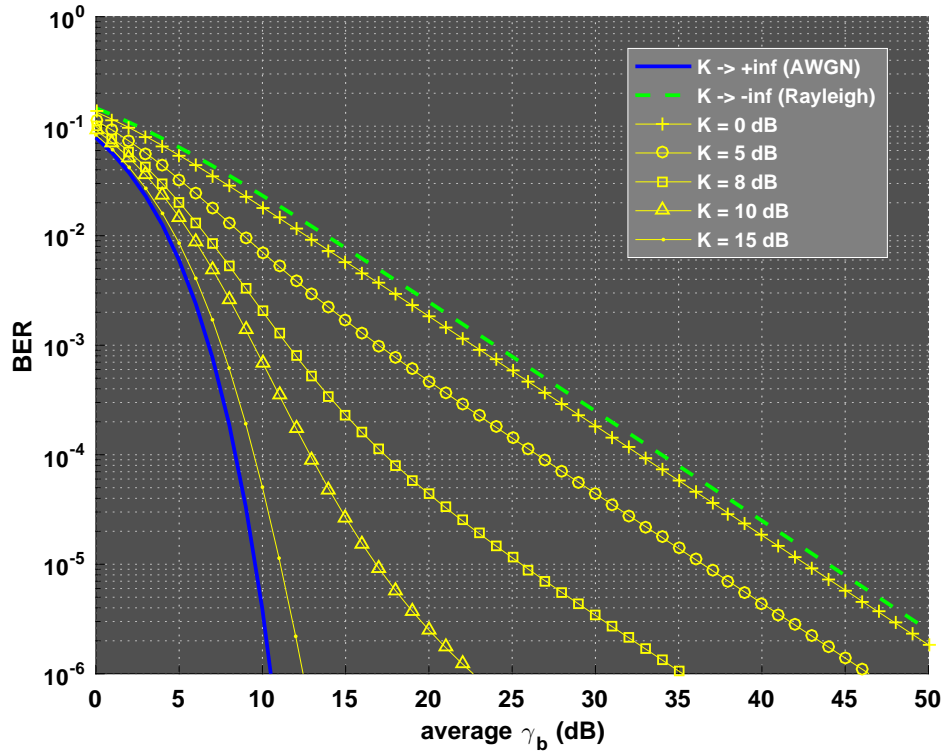


Figure 5: BER for QPSK in AWGN, Rayleigh fading, and Rician fading

performance improving mechanisms at the transmitter and the receiver in order to reduce multipath effects. MIMO antenna techniques offer an attractive solution that improves the BER performance in fading environments. These techniques will be outline in the following chapter.

3 MIMO Techniques in Wireless Communications

MIMO techniques in wireless communications can be divided into two categories: space diversity techniques and spatial multiplexing techniques [9]. Space diversity techniques are used in communications systems primarily to combat the effects of multipath fading in wireless channels. The idea behind space diversity is to transmit replicas of the same signal from the same transmitter such that the transmitted signals experience independent fading environments as they travel through the air. Typically, the probability that the signals suffer periods of deep fading simultaneously is low so, at the receiver, the signals can be combined coherently to average out the effects of those signals that inherited fading from the channel; thus, improving the quality of reception. Spatial multiplexing techniques are used for a different goal; improve the capacity (increase the data rates) of the wireless channel. In spatial multiplexing, independent signal streams are transmitted from each available transmit antenna so that more information can be simultaneously sent to the receiver at any given time.

The potential system capacity improvement in spatial multiplexing is dependent on the number of available transmit and receive antennas. This capacity improvement is commonly referred to as multiplexing gain. A similar performance improving metric can also be achieved with space diversity techniques.

Section 3.1 will focus on the most commonly used transmit and receive antenna diversity techniques. Maximal-ratio receiver combining (MRRC), in section 3.1.1, describes a single-input-multiple-output (SIMO) diversity scheme with 2 receive antennas. Section 3.1.2 will then follow to outline transmit diversity techniques, mainly the well-known Alamouti transmit diversity scheme for multiple-input-single-output (MISO) antenna system. An extension of the Alamouti scheme for 2x2 MIMO systems will also be described in the same section.

3.1 Diversity Techniques

Multi-antenna diversity techniques can take different forms depending on the number of antennas available at the transmitter and receiver, also called an antenna array. The idea is that the elements in the antenna array have enough distance separation so that the signals transmitted from each antenna element experience independent fading. The minimum distance separation required for independent fading on each antenna is approximately 0.5λ (or 0.38λ to be precise [5]). The diversity gain is maximized once this minimum antenna separation is met and the transmission paths from the antenna elements become highly correlated once this separation is reduced yielding a lower diversity gain.

The impact of diversity gain is reflected in BER curves as a change in slope of

the error rate probability with respect to SNR. Examples on how the slope of the BER curves changes with the increase in diversity gain will be shown in section 3.1.3.

3.1.1 Maximal-Ratio Receiver Combining

The baseband model of a system that employs MRRC to achieve diversity gain is shown in Figure 6. We make the assumptions that the two receiver branches go through their own RF front-end but experience identical noise PSD (i.e. $|n_1(t)|^2 = |n_2(t)|^2$), so in a non-fading environment, each branch has the same SNR, $\gamma_i = E_b/N_o$. The channel estimation block in Figure 6 has two very-important functionalities. First, it estimates the SNR for each of the branches and second, it computes estimates of the channel coefficients, $h_1(t) = \alpha_1(t)e^{j\theta_1(t)}$ and $h_2(t) = \alpha_2(t)e^{j\theta_2(t)}$, in time. It does so by capturing changes in the pilot (or references) sequences included in $s(t)$ that the receiver knows a priori.

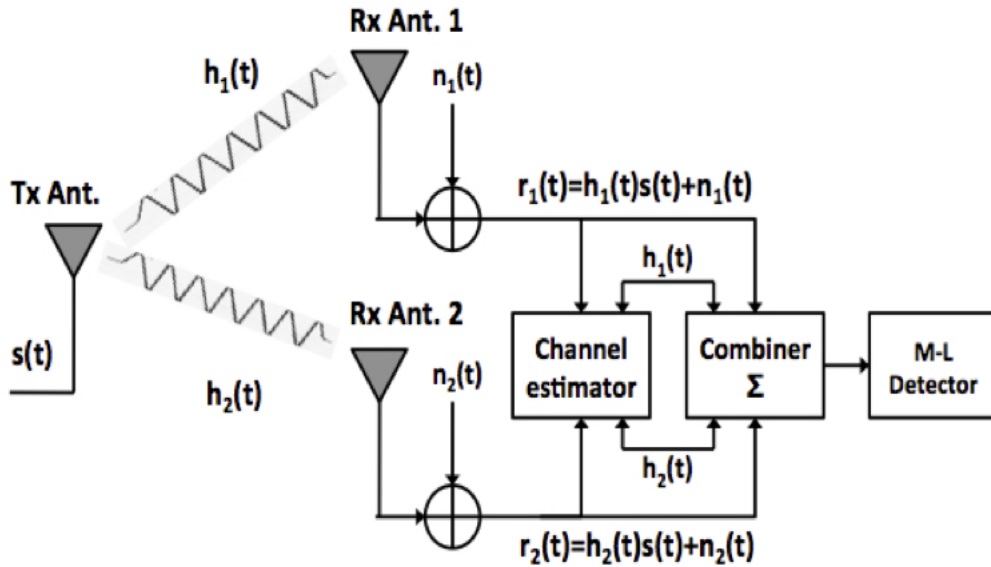


Figure 6: Receiver Diversity Model

The role of the combiner is to use the information provided by the channel estimator and weight each one of the branches according to their branch SNR and channel state information, $h_i(t)$. It multiplies each branch by a factor g_i so to maximize the combined SNR, γ_Σ , observed at the output of the combiner. In section 7.2.4 of [5], it has been shown that the optimal value of g_i should be $h_i^*(t)\sqrt{\gamma_i}$. The factor g_i , not only makes appropriate weighting on each branch but also co-phases all received signals so they can be coherently combined.

With receiver diversity, there are actually two types of gain that can be obtained. The first gain relates to the power gain attained by combining all the signals from the branches. This gain is typically referred to as array gain. Array gain can be understood by noting that $\gamma_{\Sigma} = \sum_{i=1}^2 \gamma_i = \frac{1}{N_o} \sum_{i=1}^2 E_b^i$ in the absence of fading (i.e. $\alpha_1(t) = \alpha_2(t) = 1$), thus by appropriately combining the signal strength from all branches, we increase the SNR at the output of the combiner. The second gain relates to diversity gain which is achieved by having independent fading paths.

3.1.2 The Alamouti Transmit Diversity Technique

When comparing the error rate improvement of diversity techniques over SISO systems, the total transmission power should be the same for the two cases. Therefore, in the MISO case, the transmission power should be divided amongst the available transmit antennas. By constraining the transmission power on each transmit antenna, the combined signals at the receiver yield no improvement in signal strength if compared to the SISO case; moreover, weighting and co-phasing each transmission path according to their own SNR and channel state information (CSI) is not a straight forward operation since the signals combine over-the-air and to de-entangle them at the receiver is difficult.

Most transmit diversity techniques require CSI at the transmitter so the receiver must use some way to measure each individual transmission channel and feed this information back to the transmitter. The transmitter uses the CSI to compensate for the channel effects so the receiver can coherently combine the signals. Feedback of the CSI requires an additional and reliable channel between the receiver and the transmitter which may not always be available. One easy solution to obtain transmit diversity gain without CSI at the transmitter is to utilize the space and time domain. By transmitting the same information over different transmit antennas and over consecutive time intervals, we get the diversity benefits desired.

In this section we will describe a space-time diversity technique called the Alamouti transmit diversity scheme. The Alamouti transmit diversity scheme introduced by Siavash M. Alamouti [12] is a simple space-time diversity technique meant to combat the detrimental effects of channel fading and improve error rate performance of wireless communication systems by employing two antennas at the transmitter. The basic premise of this scheme is that it does not require the transmitter to have knowledge of the CSI. By doing some simple processing at the transmitter, Alamouti showed that this novel technique is capable of achieving same diversity gain benefits as MRRRC.

In order to demonstrate how this scheme works let us consider symbols s_1 and s_2 which represent data symbols to be transmitted using two transmit antennas. The scheme works over two transmission intervals, where each transmission interval last T seconds. During the first transmission interval, the symbols s_1 and s_2 will be transmitted from antenna 1 and antenna 2 respectively. On the second symbol

interval, the same symbols will also be transmitted but this time symbol $-s_2^*$ is transmitted from antenna 1 while symbol s_1^* is transmitted from antenna 2 (see Figure 7). This transmission scheme assumes the the channel remains unchanged during the two transmission intervals where s_0 , s_1 and their conjugated replicas are transmitted.

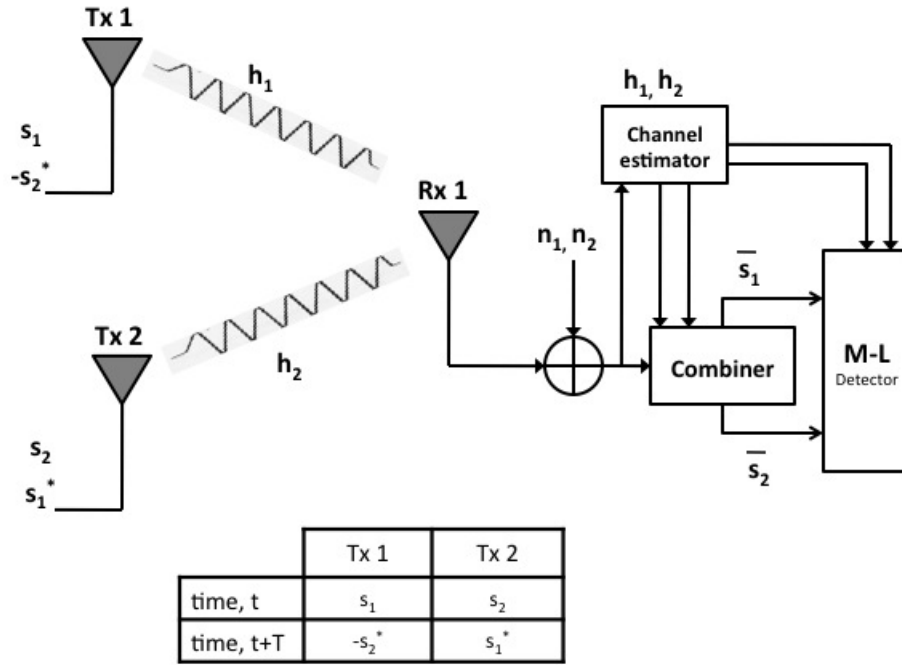


Figure 7: The Alamouti transmit diversity scheme of a 2x1 wireless communication system

The received signals using the Alamouti technique can be described in the following manner,

$$\begin{bmatrix} r_1 \\ r_2^* \end{bmatrix} = \begin{bmatrix} h_1 & h_2 \\ h_2^* & -h_1^* \end{bmatrix} \begin{bmatrix} s_1 \\ s_2 \end{bmatrix} + \begin{bmatrix} n_1 \\ n_2^* \end{bmatrix} = \mathbf{H}\mathbf{s} + \mathbf{n} \quad (3.1)$$

where r_1 represents the received signal $r(t)$ and r_2 represents the conjugate of the received signal $r(t + T)$, \mathbf{s} represents the transmitted signal vector, and \mathbf{n} represent the noise vector composed of two complex Gaussian random variables with zero mean and variance $N_o/2$. In Figure 7, after the channel estimator sends the estimated channel responses to the Alamouti combiner, the combiner generates the matrix \mathbf{H}^H and performs the following operations in order to extract s_1 and s_2 from the received

signals.

$$\begin{bmatrix} \tilde{s}_1 \\ \tilde{s}_2 \end{bmatrix} = \mathbf{H}^H \begin{bmatrix} r_1 \\ r_2^* \end{bmatrix} = \begin{bmatrix} h_1^* & h_2 \\ h_2^* & -h_1 \end{bmatrix} \begin{bmatrix} r_1 \\ r_2^* \end{bmatrix} = \begin{bmatrix} h_1^* r_1 + h_2 r_2^* \\ h_2^* r_1 - h_1 r_2^* \end{bmatrix} \quad (3.2)$$

By substituting 3.1 into 3.2 we obtain,

$$\begin{bmatrix} \tilde{s}_1 \\ \tilde{s}_2 \end{bmatrix} = \begin{bmatrix} (|h_1|^2 + |h_2|^2)s_1 + h_1^* n_1 + h_2 n_2^* \\ (|h_1|^2 + |h_2|^2)s_2 - h_1 n_2^* + h_2^* n_1 \end{bmatrix} \quad (3.3)$$

After the combiner, the combined signals are sent to an ML detector which makes a decision on \tilde{s}_1 and \tilde{s}_2 .

The Alamouti scheme for 2x2 MIMO

The system diagram for 2x2 MIMO is shown in Figure 8. If we incorporate an additional receive antenna to the analysis of the Alamouti scheme described above, the received signals can be described by the following vector of equations,

$$\begin{bmatrix} {}^1r_1 \\ {}^2r_1 \\ {}^1r_2^* \\ {}^2r_2^* \end{bmatrix} = \begin{bmatrix} h_1 & h_2 \\ h_3 & h_4 \\ h_2^* & -h_1^* \\ h_4^* & -h_3^* \end{bmatrix} \begin{bmatrix} s_1 & s_2 \end{bmatrix}^T + \begin{bmatrix} n_1 \\ n_2 \\ n_3^* \\ n_4^* \end{bmatrix} = \mathbf{H}\mathbf{s}^T + \mathbf{n} \quad (3.4)$$

${}^i r_1$ represents the received signal $r(t)$ for receive antenna $i = 1, 2$. Similarly, ${}^i r_2$ represents the received signal $r(t + T)$ for the pair of received antennas. At the combiner, the following operation takes place,

$$\begin{aligned} \begin{bmatrix} \tilde{s}_1 \\ \tilde{s}_2 \end{bmatrix} &= \mathbf{H}^H \begin{bmatrix} {}^1r_1 & {}^2r_1 & {}^1r_2^* & {}^2r_2^* \end{bmatrix}^T \\ &= \begin{bmatrix} h_1^* & h_3^* & h_2 & h_4 \\ h_2^* & h_4^* & -h_1 & -h_3 \end{bmatrix} \begin{bmatrix} {}^1r_1 & {}^2r_1 & {}^1r_2^* & {}^2r_2^* \end{bmatrix}^T \\ &= \begin{bmatrix} {}^1r_1 h_1^* + {}^2r_1 h_3^* + {}^1r_2^* h_2 + {}^2r_2^* h_4 \\ {}^1r_1 h_2^* + {}^2r_1 h_4^* - {}^1r_2^* h_1 - {}^2r_2^* h_3 \end{bmatrix} \\ &= \begin{bmatrix} (|h_1|^2 + |h_2|^2 + |h_3|^2 + |h_4|^2)s_1 + h_1^* n_1 + h_3^* n_2 + h_2 n_3^* + h_4 n_4^* \\ (|h_1|^2 + |h_2|^2 + |h_3|^2 + |h_4|^2)s_2 - h_1 n_3^* + h_2^* n_1 - h_3 n_4^* + h_4^* n_2 \end{bmatrix} \end{aligned} \quad (3.5)$$

After the combiner performs these operations, the combined signals are sent to an ML detector to make decisions on \tilde{s}_1 and \tilde{s}_2 . By looking at the equations for \tilde{s}_1 and \tilde{s}_2 in (3.5), it's clear how path diversity aid on the detection of \tilde{s}_1 and \tilde{s}_2 . The term $(|h_1|^2 + |h_2|^2 + |h_3|^2 + |h_4|^2)$ demonstrates the essential idea about diversity techniques. If any of the individual components experiences deep fading, its effect can be diminished by the combined strength of the other components. A similar condition is shown in equation(3.3).

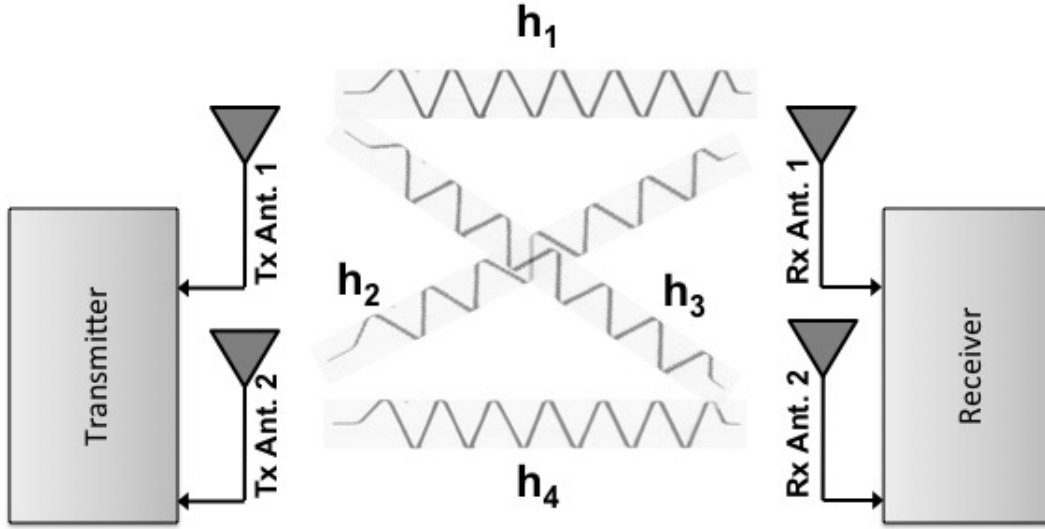


Figure 8: System diagram for 2x2 MIMO

3.1.3 BER Performance of Diversity Techniques

In order to evaluate the BER performance of the various diversity techniques mentioned previously, we can make use of the analytical framework described in section 2.2.1. More specifically, the integral in equation (2.9) can be used to evaluate the average probability of bit error using the MGF of the fading distribution being considered. The same MGF for Rayleigh fading and Rician fading channels can be used to evaluate the BER performance of multi-antenna links. In section 9.2.3 of [11], it is shown that the BER curve for a system employing diversity techniques can be derived using the following expression of products of MGFs ,

$$M_{\Pi}(s) = \prod_{i=1}^{L_T L_R} M_{\gamma_i}(s) \quad (3.6)$$

where L_T represents the number of transmit antennas and L_R is the number of receive antennas. The MGF of each transmit and receive antenna pair (or branch) is denoted by $M_{\gamma_i}(s)$. If all the branches experience the same fading environment and observe the same SNR, γ , at the receiving end, equation (3.6) becomes,

$$M_{\Pi}(s) = [M_{\gamma}(s)]^{L_T L_R} \quad (3.7)$$

This form of the MGF can then be substituted in (2.9) in order to evaluate the BER performance of multi-antenna communication systems using diversity techniques in flat-fading channels. The BER integral takes the following form,

$$\begin{aligned} \tilde{P}_b &= \frac{1}{\pi} \int_0^{\frac{\pi}{2}} M_{\Pi} \left(-\frac{1}{\sin^2 \theta} \right) d\theta \\ &= \frac{1}{\pi} \int_0^{\frac{\pi}{2}} \left[M_{\gamma} \left(-\frac{1}{\sin^2 \theta} \right) \right]^{L_T L_R} d\theta \end{aligned} \quad (3.8)$$

BER Performance of MRRC in Rayleigh and Rician Fading

The BER performance of an MRRC system employing 2 receive antennas in Rayleigh fading is given by,

$$\tilde{P}_b = \frac{1}{\pi} \int_0^{\frac{\pi}{2}} \left(\frac{1}{1 + \frac{\tilde{\gamma}_b}{\sin^2 \theta}} \right)^2 d\theta = \frac{1}{2} \left(1 - \sqrt{\frac{\tilde{\gamma}_b(2\tilde{\gamma}_b + 3)^2}{4(\tilde{\gamma}_b + 1)^3}} \right) \quad (3.9)$$

It is important to note that the equation in the integrand is the same as in SISO Rayleigh fading and the exponent of the integrand is determined by $L_T L_R = 2$.

In Rician fading channels, the BER curve of the MRRC system can be evaluated using the following integral,

$$\tilde{P}_b = \frac{1}{\pi} \int_0^{\frac{\pi}{2}} \left(\frac{(1 + K)\sin^2 \theta}{(1 + K)\sin^2 \theta + \tilde{\gamma}_b} \right)^2 \exp \left(\frac{-2K\tilde{\gamma}_b}{(1 + K)\sin^2 \theta + \tilde{\gamma}_b} \right) d\theta \quad (3.10)$$

Again, as in equation (2.13), this integral needs to be evaluated numerically.

BER of the Alamouti Scheme in Rayleigh and Rician Fading

The BER performance curves of the Alamouti Scheme in Rayleigh fading and Rician fading channels can be evaluated using equations (3.9) and (3.10). In the 2x1 Alamouti case, the total transmission power is divided into half the power to antenna one and the other half to the second antenna, therefore, in order to evaluate the BER performance integrals we should replace $\tilde{\gamma}_b$ by $\tilde{\gamma}'_b = \tilde{\gamma}_b/2$

The last set of BER integrals in our diversity analysis are for the 2x2 Alamouti case which was briefly described in section 3.1.2. Equation (3.11), shows the BER performance for the 2x2 Alamouti diversity scheme in Rayleigh fading so the integrand in this case is raised to the power of $L_T L_R = 4$.

$$\tilde{P}_b = \frac{1}{\pi} \int_0^{\frac{\pi}{2}} \left(\frac{1}{1 + \frac{\tilde{\gamma}'_b}{\sin^2 \theta}} \right)^4 d\theta = \frac{1}{2} \left(1 - \sqrt{\frac{\tilde{\gamma}'_b(16\tilde{\gamma}'_b{}^3 + 56\tilde{\gamma}'_b{}^2 + 70\tilde{\gamma}'_b + 35)^2}{256(\tilde{\gamma}'_b + 1)^7}} \right) \quad (3.11)$$

For Rician fading, the BER integral is shown in equation (3.12)

$$\tilde{P}_b = \frac{1}{\pi} \int_0^{\frac{\pi}{2}} \left(\frac{(1 + K)\sin^2 \theta}{(1 + K)\sin^2 \theta + \tilde{\gamma}_b} \right)^4 \exp \left(\frac{-4K\tilde{\gamma}_b}{(1 + K)\sin^2 \theta + \tilde{\gamma}_b} \right) d\theta \quad (3.12)$$

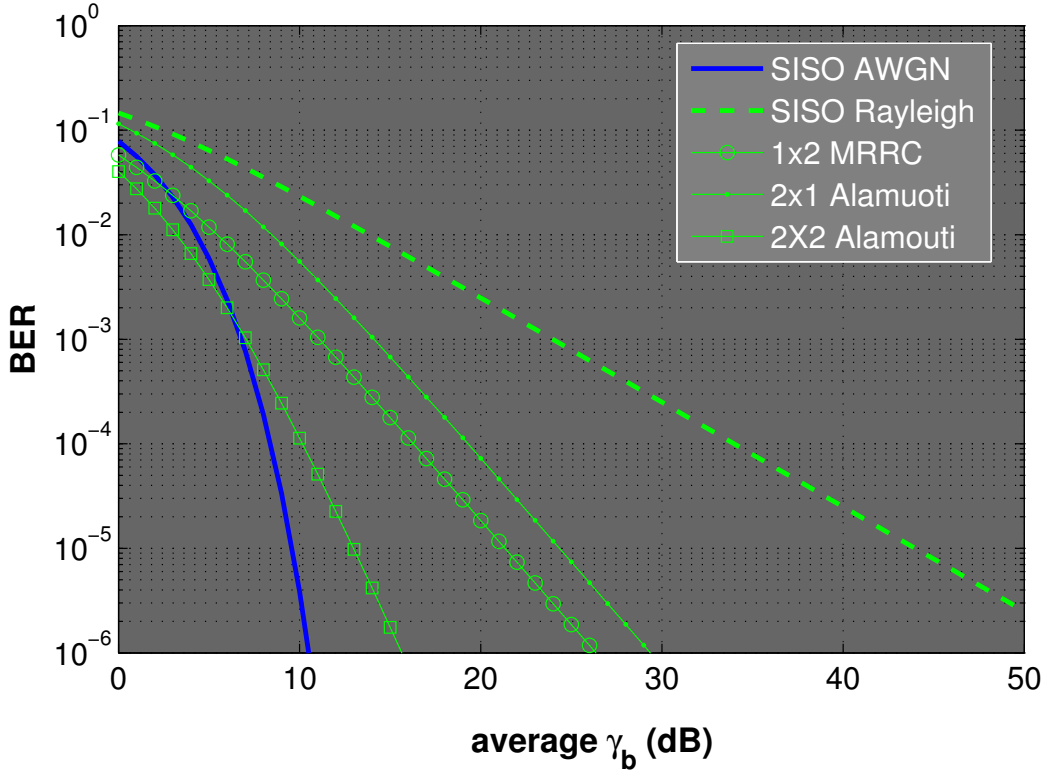


Figure 9: BER comparison of diversity techniques in Rayleigh flat-fading channels

Figure 9, shows the Rayleigh fading BER of the different diversity techniques discussed in this section. For comparison, the BER of SISO under Rayleigh fading and under no fading (AWGN) are also included in the figure. The figure clearly depicts the advantages of using diversity techniques in multiple-antenna systems. For example, to achieve an error rate performance of 10^{-5} in Rayleigh fading, it requires approximately 44 dBs in SNR if no diversity scheme is used. Adding an extra antenna into the system yields an approximate 20 dB improvement in SNR if we use Alamouti's transmit diversity technique; we could get an additional 3 dB improvement if we add the antenna to the receiving end and employ MRRC. In order to achieve the same performance using the 2x2 Alamouti scheme, the required SNR should be approximately 13 dB.

To illustrate the diversity gain achieved by each diversity technique, we can calculate the slope of the green curves shown in the figure. The slope of the BER curve for SISO in Rayleigh fading shows that the error rate decreases an order of magnitude for every 10-dB increase in SNR. So this one-to-one relationship between error rate and SNR (in the dB scale) is said to have a diversity gain of one (or 0 dB gain) which is obvious since no diversity benefits can be attained in this case. Similarly, the BER curves for both MRRC and the 2x1 Alamouti scheme show a slope with diversity gain of 2 which means that the error rate decreases two orders of magnitude over a 10 dB increase in SNR. The BER curve with the highest diversity

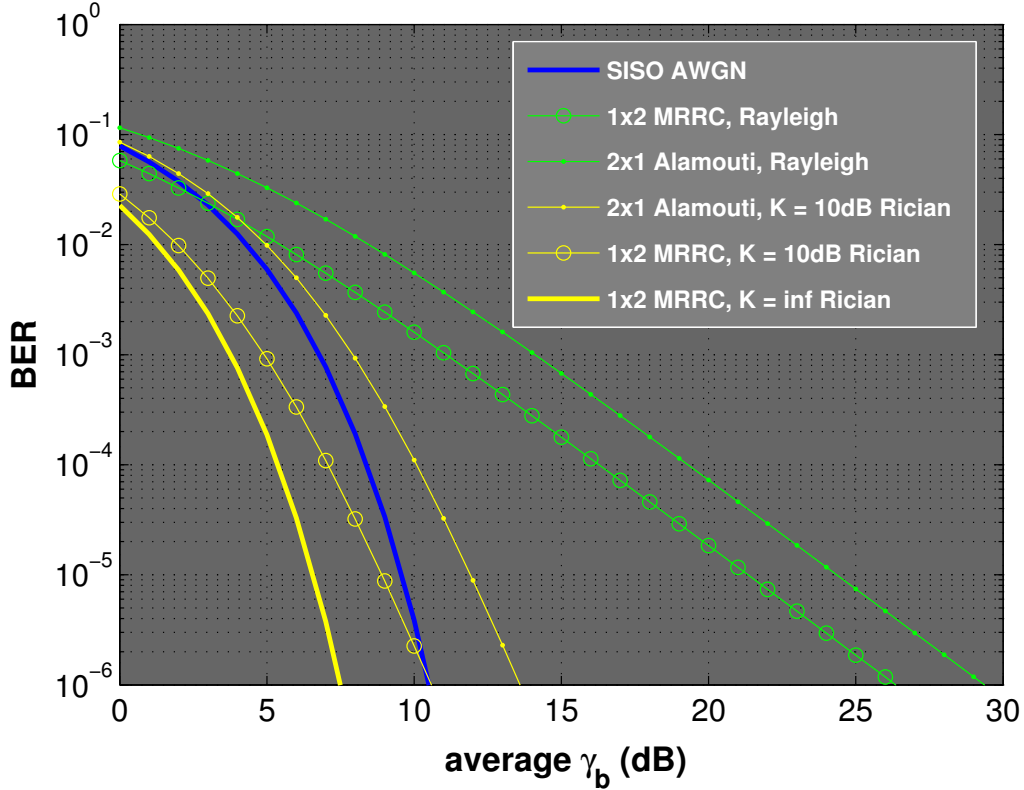


Figure 10: BER comparison of diversity techniques in Rician flat-fading channels

gain in the figure is the 2x2 Alamouti curve which achieves a diversity gain of 4, i.e. the error rate decrease by a factor of 10^4 over a span of 10 dBs in SNR.

The last important observation to be made about Figure 9 is the 3-dB SNR shift between MRRC and the 2x1 Alamouti scheme. This SNR gain of MRRC over the 2x1 Alamouti scheme is the array gain advantage of MRRC which was discussed in section 3.1.1.

The BER performance curves of both MRRC and the Alamouti scheme in Rician fading channels are depicted in Figure 10. There are few observations to be made about these set of graphs. First, when the K factor approaches $+\infty$ in the Rician channel (i.e. the effects of multipath components become negligible), the 2x1 Alamouti BER curve converges to the SISO AWGN curve and the MRRC curve exhibits the same performance of SISO in AWGN as well in addition to a 3-dB array gain. On the other hand, when the K factor approaches $-\infty$ in the Rician channel, i.e. the strength of the line-of-sight component mixes with the rest of the multipath components and its effect is imperceptible, the 2x1 Alamouti curve exhibits the performance as in Rayleigh fading. The same can be said about the BER curve for MRRC which converges to the its Rayleigh fading counterpart as well. An example where $K = 10$ dB is also shown in this figure for both MRRC and the 2x1 Alamouti

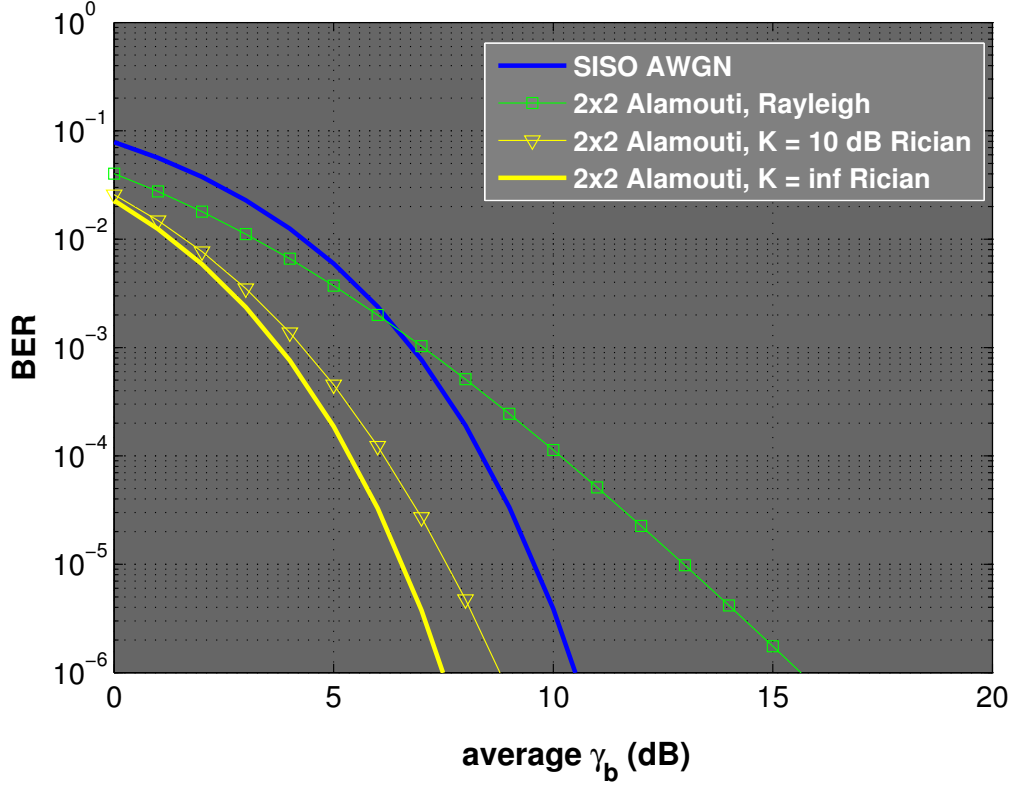


Figure 11: BER performance of the 2x2 Alamouti scheme in Rayleigh and Rician flat-fading channels

scheme.

The plots in Figure 11 show the BER performance of the 2x2 Alamouti scheme in both Rayleigh and Rician fading channels. Similar to Figure 10, the Alamouti scheme in Rician fading converges to Rayleigh when K approaches $-\infty$ and also converges to AWGN SISO BER curve plus an additional 3 dB array gain when K approaches $+\infty$. One important thing to note in this figure is that the BER performance of the Alamouti scheme when $K \rightarrow +\infty$ is identical to the BER performance of MRRC in Rician fading when $K \rightarrow +\infty$ (see Figure 10).

4 LTE Testbed using USRP Hardware

4.1 LTE Standardization

Long-Term Evolution (LTE) is a radio access network technology standard leading wireless technologies worldwide beyond Third Generation (3G) mobile telecommunications technology. LTE standardization is carried out and handled by The 3rd Generation Partnership Project (3GPP). 3GPP unites seven telecommunications standard development organizations around the globe and provides their members with a stable environment to produce the Reports and Specifications that define 3GPP technologies [13]. 3GPP helps to develop and maintain most of the key cellular standards in the global market today. In doing so, it focuses on future cellular technology data and connectivity needs and demands, often conforming with relevant International Telecommunication Union (ITU) requirements such as International Mobile Telecommunications-2000 (IMT-2000) for 3G systems and IMT-Advanced (IMT-A) for systems classified as fourth generation (4G).

4G work initiated in 3GPP during 2004. At the time it was forecasted that 3G data rates and spectral efficiency would not meet future wireless demands. Consequently, a new system on the evolution of 3G had to be developed to keep 3GPP mobile communication systems competitive over 10 years and beyond, by delivering the high data rates, spectral efficiency, and low latencies that would be needed in the years to come. 3GPP TSG RAN approved the start of the study for LTE in December 2004. First running in the RAN plenary level to define the requirements, followed by moving to the working groups for detailed technical discussions for multiple access, protocol solutions, and architecture [14][15]. In a somewhat bold move, it was decided to completely change both the air interface and the core network. The air interface was set to use OFDM as modulation, Orthogonal Frequency Division Multiple Access (OFDMA), and some support for MIMO antenna technology. The core network was to evolve into a pure packet-switched network [7].

The main output of the 3GPP study into LTE was a requirements specification and targets for the air interface. These targets/requirements are documented in 3GPP Technical Report (TR) 25.913. The technical report requires LTE to support a flexible transmission bandwidth of up to 20MHz , a peak *downlink/uplink* data rate of $100/50\text{Mbps}$ when using *2-receive/1-transmit* antenna at the UE, a round-trip time not exceeding 10msec , and an improved *downlink/uplink* average spectrum efficiency 3-to-4/2-to-3 times better relative to HSDPA/HSUPA release 6 [16]. In addition to these air interface requirements, LTE systems must be packet-switched optimized, provide high level of mobility and security, and the terminal power consumption must be minimized to enable more usage of multimedia appli-

cations without recharging the battery [15].

LTE was first standardized in Release 8 and was frozen in December 2008. The eventual system exceeded the peak data rate requirements outlined in TR 25.913 and delivered peak data rates of 300Mbps in the downlink and 75Mbps in the uplink. To achieve such requirements, the first release of LTE offers Frequency and Time Division Duplexing (FDD/TDD) for all supported bandwidths up to 20MHz . It uses QPSK, 16QAM, and 64QAM modulation in conjunction with OFDMA in the downlink and SC-FDMA in the uplink to improve spectral efficiency and combat channel-induced ISI. Furthermore, it utilizes 4×4 MIMO antenna technology in the downlink [14][15]. In the core network and overall system architecture side, LTE does not follow traditional circuit-switched telephony service, but all-Internet Protocol (IP) based communication such as IP telephony. LTE aims to minimize the number of network elements by having a flat architecture. Release 8 also facilitates radio level inter-working with GSM, WCDMA, and cdma2000® [15].

During March of 2008, The ITU- Radio communications sector (ITU-R) launched a set of requirements for a 4G communication system under the name IMT-A specification. According to these requirements, 4G peak data rates service should deliver 100Mbps for high mobility communication (such as from trains and cars) and 1Gbps for low mobility communication (such as pedestrians and stationary users) [14]. IMT-A systems comprise new capabilities and new services, migrating towards an all- IP network. IMT-A is expected to become, through a continuous evolution, the dominant technology designed to support new applications, products and services [17].

Since LTE first release, it supports much less than 1Gbps peak data rate. Therefore, it is not fully IMT-A compliant, yet it is often branded 4G by service providers. However, there is a clear technical transition in the move from 3G systems like UMTS to LTE. So despite the technical inferiority, in October 2010, the ITU gave its blessing to brand LTE as a 4G system, and also any other technology with substantially better performance than the early 3G systems [14].

Driven by IMT-A's 4G requirements, 3GPP started a study in order to boost the capabilities of LTE. The main product from the study was a specification for a system called LTE-A. The goal of LTE-A is to augment LTE radio access capabilities and system performance such that LTE not only fulfills but exceeds all the requirements defined in IMT-A. To achieve such goals, LTE-A was required to deliver a peak data rate of 1Gbps in the downlink, and 500Mbps in the uplink. In practice, however, the system can potentially deliver peak data rates of 3000 and 1500Mbps respectively, using a total bandwidth of 100MHz that is made from five separate components of 20MHz each [14].

LTE-A starts from 3GPP release 10. The specific technical details of LTE-A improvements over earlier LTE releases are described below [18]:

- **Carrier Aggregation:** Multiple component carriers of up-to 20MHz can aggregated to support transmission bandwidths of up to 100MHz .
- **Extended MIMO:** Increase the number of downlink transmission layers to 8 and the number of uplink transmission layers to 4, in order to increase the data rates.
- **Coordinated Multipoint (CoMP) Transmission/Reception:** Transmission/Reception is performed jointly across multiple cell sites to improve cell-edge performance.
- **Relays:** Improve coverage and reduce deployment cost.

4.2 LTE Architecture

Release 8 of LTE provides a new flat radio-network architecture designed to simplify the operation and minimize costs. It is intended to deliver packet-switched traffic with seamless mobility, high Quality-of-Service (QoS), and minimal latency. The architecture is comprised of four level domains (illustrated in Figure 12): User Equipment (UE), Evolved Universal Terrestrial Radio Access Network (E-UTRAN), Evolved Packet Core Network (EPC), and the Services domain. However, the new architectural development is limited to the radio access (E-UTRAN) and the core network (EPC). UE and Services domain are architecturally the same but functional evolution has also continued in these domain[15].

UE, E-UTRAN, and EPC combined represent the Internet Protocol (IP) Connectivity Layer, commonly referred to as Evolved Pack System (EPS). The main role of this layer is to provide IP based connectivity to higher layers. Moreover, circuit-switched elements and interfaces are completely eliminated inside E-UTRAN and EPC [15].

The development in E-UTRAN is focused on the Evolved Node B (eNodeB), which serves as the end point for all radio related protocols. E-UTRAN is simply a web of eNodeBs connected together through X2 interfaces. An eNodeB primarily acts as the Layer 2 bridge between UE and EPC. It terminates all radio protocols from UE to EPC, and provides IP data packets from the radio connection to the EPC. The eNodeB performs many control plane functions as well. It is responsible for Radio Resource Management (RRM), function that controls access and utilization of the radio resources and interfaces. eNodeBs have a critical role in Mobility Management when it comes to making decision to handover UE's between eNodeBs. It controls and analyses signal level measurements which are performed by the UE and by itself to determine the handovers [15].

Inside the EPC there are entities such as the Mobile Management Entity (MME), the Serving Gateway (S-GW) and the Packet Data Network Gateway (P-GW) which are part of the System Architecture Evolution (SAE), the Policy and Charging Resource Function (PCRF), and the Home Subscriber Server (HSS). The MME

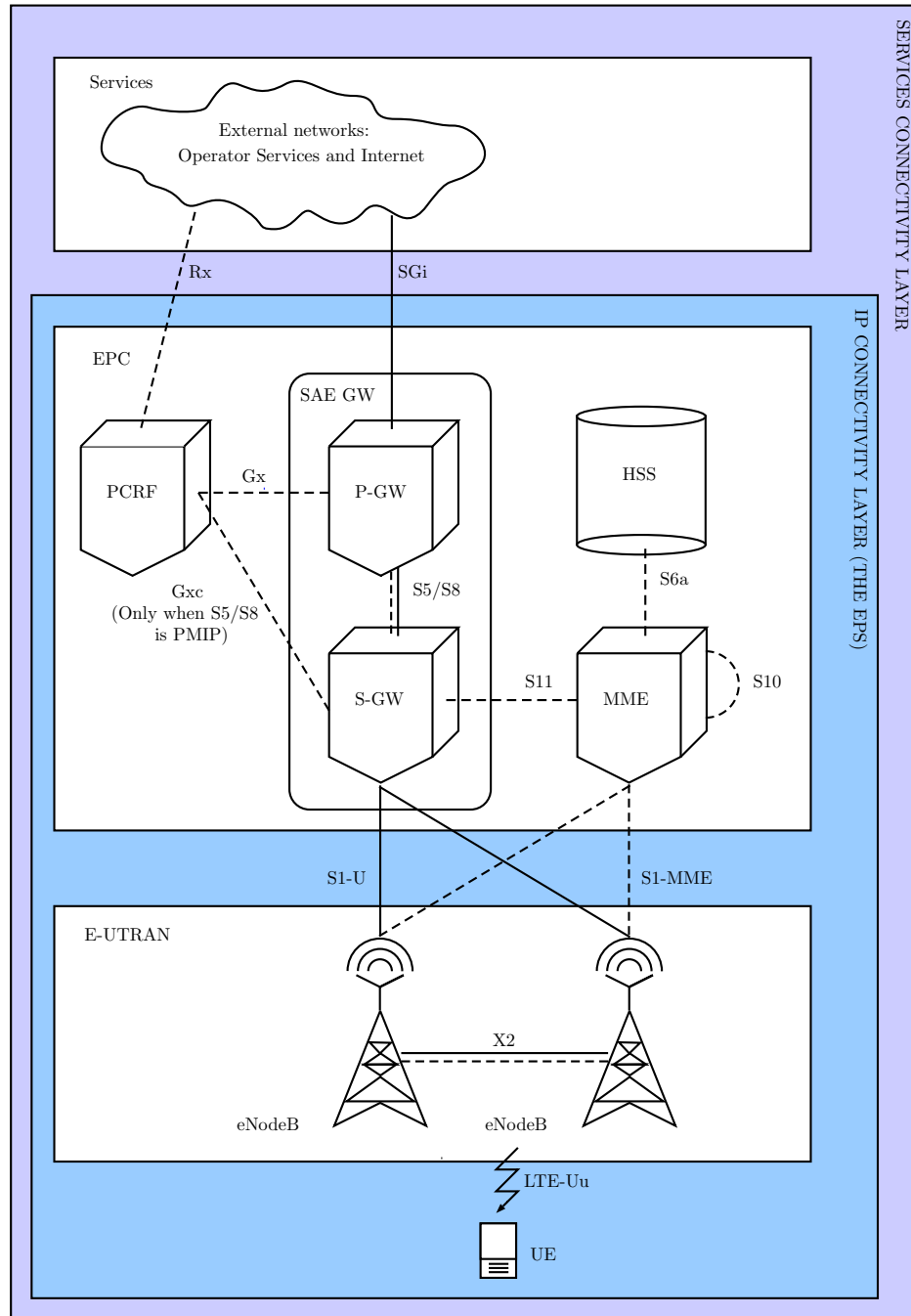


Figure 12: System architecture for LTE network

is the main control plane element in the EPC and its primary functions relate to

- 1) Authentication and Security when a UE registers to the network for the first time,
- 2) Mobility Management which keeps track of the location of all UEs in the area, and
- 3) Managing Subscription Profile and Services Connectivity for UEs.

The S-GW main functionality is to control and manage user plane tunnels for uplink and downlink data delivery. The P-GW sits at the edge between the EPS and the outside packet data network. It functions as the IP point of attachment for the UE and performs

traffic gating and filtering for various services. The PCRF performs Policy and Charging Control (PCC) by making decision on how to handle services in terms of QoS, and provides information to other entities in the EPC so that appropriate bearers and policies can be created. Finally, the HSS is the subscription data storage for all permanent user data. It stores the master copy of the subscriber profile, which provides the information about the services that are applicable for the user [15].

4.3 LTE Protocol Stack

The network elements in the system architecture described previously follow specific set of rules to communicate through the various interfaces depicted in Figure 12. These set of rules are commonly referred to as the protocol stack. The LTE protocol stack contain two planes: Control Plain (CoP) and User Plane (UP). The CoP is intended for signaling purpose within network elements while the UP is intended to handle the user data. The LTE-Uu Air interface is the main focus of this chapter. Both the CoP and UP in the LTE-Uu Air interface consist of the following sub-layers:

- **PDCP (Packet Convergence Protocol):** Responsible of IP packet header compression, encryption, and integrity protection.
- **RLC (Radio Link Control):** Performs concatenation, segmentation, and re-assembly. RLC is also responsible for some level of error correction through ARQ (Automatic Repeat Request).
- **Medium Access Control (MAC):** Responsible for scheduling and multiplexing data to the physical layer based on priorities. It also performs error correction through Hybrid ARQ.
- **Physical Layer:** Carries all information from higher layers through the air interface.
- **Radio Resouce Control (RRC):** Controls the radio resources usage. It manages signaling and data connections to/from UE. This sublayer is exsisting only in the CoP.

Through the rest of the Chapter the Physical layer downlink procedure will be described. The LTE testbed MISO downlink procedure only includes a subset of the physical channels described in [20].

4.4 LTE FDD Testbed: Downlink Description

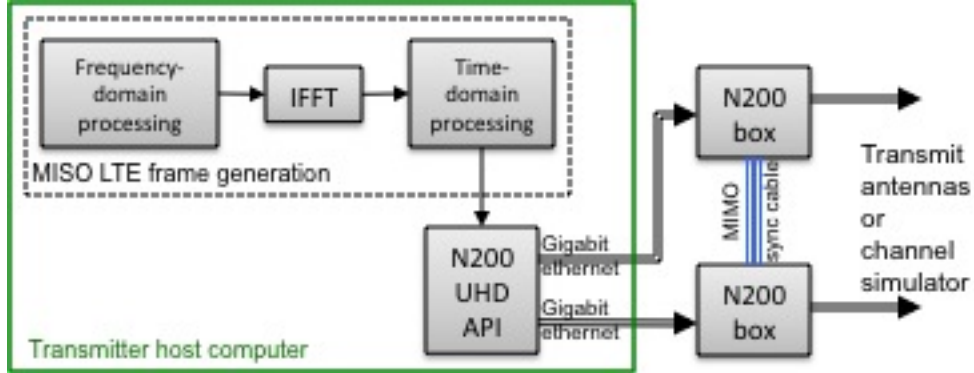


Figure 13: 2x1 MISO LTE downlink testbed block diagram

The top-level block diagram of the downlink LTE transmitter testbed with two antennas is shown in Figure 13. The transmitter host computer is connected to two N200 USRP boxes via gigabit ethernet cable. The hardware in the USRP boxes is configured using Ettus Research Universal Hardware Driver (UHD). If required, reference timing and reference local oscillator clock are provided via an external SubMiniature version A (SMA) connection and the MIMO sync cable (see [19]) located in the front of the USRP boxes. The transmitter host computer does all the frequency- and time-domain signal processing required to generate the LTE frames. THE UHD API provides the functionality to interact with the hardware inside the USRP boxes.

This chapter provides the details on how the transmitter implementation of the LTE testbed was carried out. The testbed being described is meant to evaluate the error rate performance of diversity techniques under various channel conditions using an LTE signalling framework. The LTE implementation provided in this chapter is only a small subset of the full-flesh system description provided in the LTE standard. To be precise, the following set of assumptions are defined in the implementation of the testbed.

FDD Type 1 Frame Structure

The frame structure of Type I, frequency division duplexing (FDD), ten millisecond frames is depicted in Figure 14. The frame is divided into ten subframes which are 1 millisecond each and each subframe is further divided into two 0.5 millisecond time slots. The generation of time slots, subframes, and entire frames is performed by the LTE frame generation block shown in Figure 13. The description of the frame generation procedure will be outlined in section 4.5.

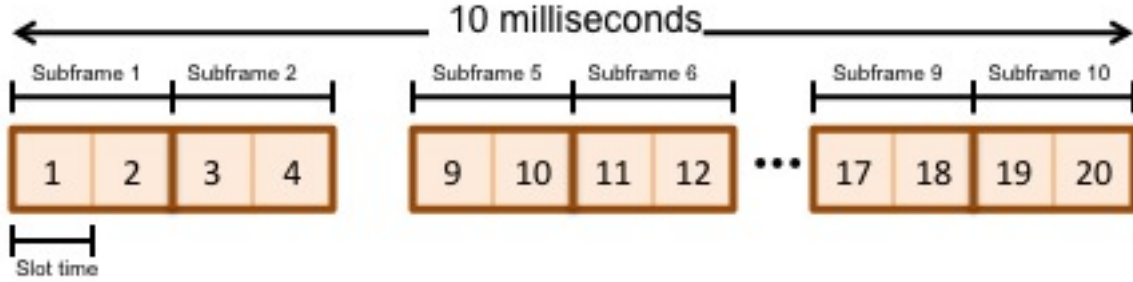


Figure 14: FDD 10 millisecond frame

One-way Single-BS-to-Single-User Downlink Signalling

The error rate performance of the LTE testbed is evaluated for the downlink where a single serving base station (BS) streams data to a single user equipment (UE). Although most LTE MIMO transmission modes defined for downlink use feedback from the UE to allocate resources to the different transmission chains, we do not incorporate any feedback channel, so the BS allocates resources evenly to all the transmit antenna chains.

Simplified Physical Channel and Physical Signals

The LTE standard defines various physical channels and physical signals such as reference signals and synchronization signals. The definition of physical channels and their corresponding mapping into resource blocks is very extensive in the LTE standard. In this version of the testbed, we have restricted the definition and the mapping of physical channels. To be precise, we followed a much different and simpler approach to generate data and to map such data to resource blocks. Our goal is to assess the error rate performance using simple LTE signalling, so our implementation of the physical channel generation and the mapping procedure is set apart from the one defined in the standard; more details will be describe later in the next section.

For the case of reference and synchronization signals, we only implement primary and secondary synchronization signals since they are necessary to define timing and frame boundaries, and restricted reference signals to cell-specific reference signals, which will be used for channel estimation.

No Error Correction Coding

Error correction coding is an important tool to improve the error rate performance at the radio link level. We are interested to look at the error rate performance for uncoded bits, therefore, the turbo coding procedure will be left out.

4.5 Overview of Physical Channels Processing

The model for processing downlink physical channels in the frequency-domain is shown in Figure 15. The model differs to the block diagram described in Figure 6.3-1 of [20] by omitting the bit pseudo-randomizer (or scrambler) and by simplifying the layer mapping procedure. Scrambling is useful to randomize inter-cell interference and to fully utilise the processing gain provided by the turbo channel coder [21], which will not be incorporated in this version of the testbed. Transmit diversity precoding is based on space-frequency transmit diversity (SFTD). SFTD techniques use one codeword per transmission since the data transmitted over the different transmit antennas is the same, therefore the layer mapping procedure is rather trivial and will be included within the precoding process described later in this chapter

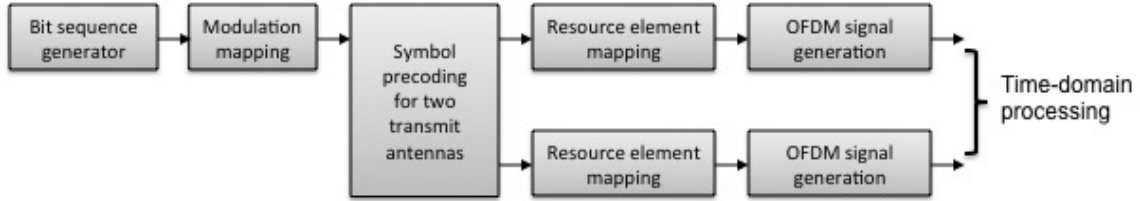


Figure 15: Downlink physical channels frequency-domain processing

4.5.1 Modulation Mapping

Three different modulation schemes are considered for error rate measurements: QPSK, 16-QAM, and 64-QAM. The I-Q cartesian coordinate mapping is shown in the figures below. The exact I-Q coordinate mapping with corresponding bit tables are provided in section 7.1 of [20].

4.5.2 Precoding for Transmit Diversity

This section combines the layer mapping and precoding procedure for two transmit antennas as described in sections 6.3.3.3 and 6.3.4.3 of [20]. Precoding for transmit diversity techniques is done through space-frequency block coding (SFBC). As mentioned previously, SFBC (or SFTD) uses one codeword per transmission on all available transmit antennas. The concept of codeword is most suitable when channel coding is involved. However, since we do not use channel coding, a codeword (for our purpose) represents an uncoded stream of modulated symbols provided by the symbol mapper described in section 4.5.1.

The layer mapping procedure for two transmit antennas, as defined by the LTE standard, uses a single codeword to create two layers. These two layers are then fed to the precoder which generates the SFBC sequences that will be transmitted from each transmit antenna. The standard defines specific layer mapping and precoding

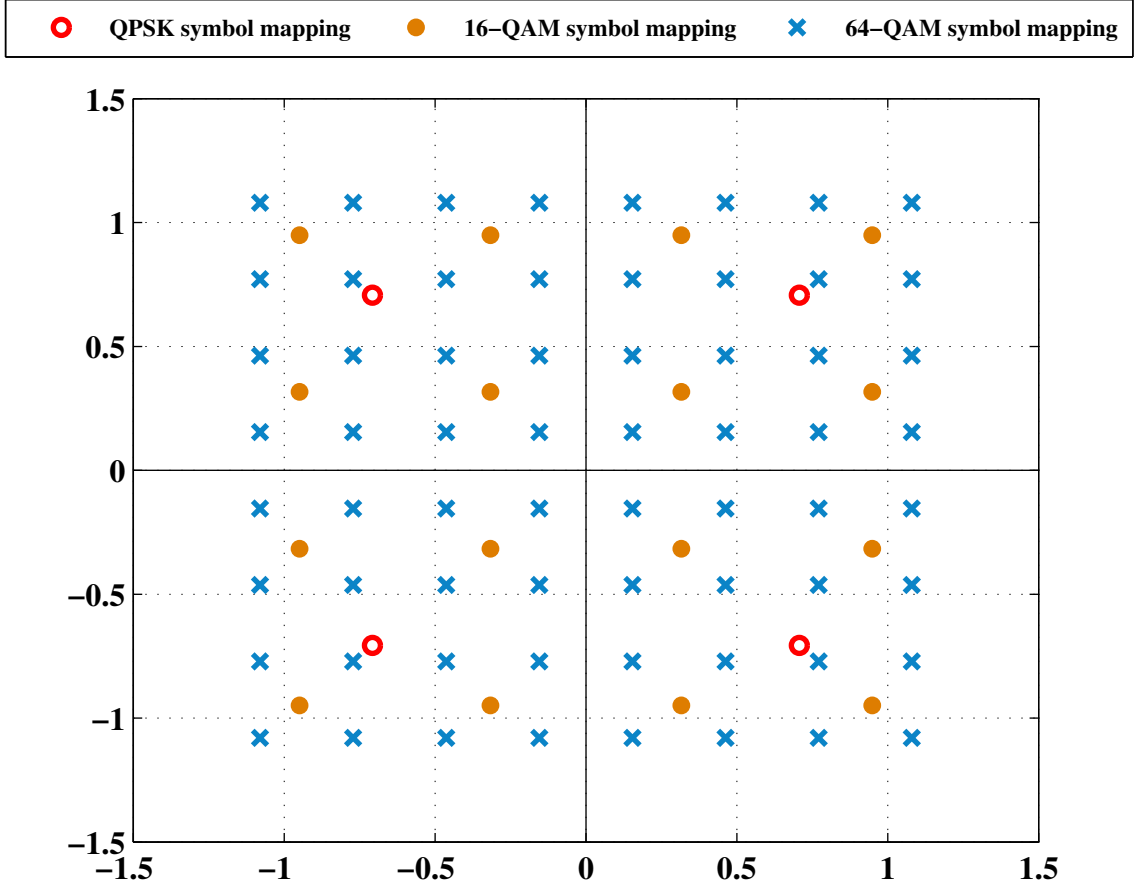


Figure 16: BPSK, 16-QAM, and 64-QAM I-Q mapping

procedures for transmit diversity, yet, we have combined the two steps into one single, equivalent precoding step that takes modulated symbols and generates SFBC sequences for each available transmit antenna and skips the layer mapping step as a whole. This is meant to simplify our computer code and to provide a simpler way to understand the SFBC operation; the concept of layers in LTE can be rather abstract, it is primarily meant for the other MIMO transmission modes defined in the LTE standard (see section 7.1 of [22]).

To understand the SFBC procedure, let us consider vector \mathbf{s} composed of elements $\{s_1, s_2, s_3, s_4, \dots, s_{M_{sympb-1}}, s_{M_{sympb}}\}$ with M_{sympb} symbols coming from the output of the modulation mapper. Also, let us define vectors $^{(1)}\mathbf{d}$ and $^{(2)}\mathbf{d}$ with size M_{sympb} to be the SFBC sequences for antenna 1 and antenna 2 respectively. The output of $^{(1)}\mathbf{d}$ and $^{(2)}\mathbf{d}$ is shown below,

$$^{(1)}\mathbf{d} = [^{(1)}d(1), ^{(1)}d(2), \dots, ^{(1)}d(M_{sympb})]^T = [s_1, s_2, \dots, s_{M_{sympb-1}}, s_{M_{sympb}}]^T \quad (4.1a)$$

$$^{(2)}\mathbf{d} = [^{(2)}d(1), ^{(2)}d(2), \dots, ^{(2)}d(M_{sympb})]^T = [-s_2^*, s_1^*, \dots, -s_{M_{sympb}}^*, s_{M_{sympb-1}}^*]^T \quad (4.1b)$$

It is worth noticing that the only difference between this transmit diversity precoding procedure and the Alamouti space-time coding technique described in the previous chapter is that the SFBC operations are only performed on $^{(2)}\mathbf{d}$, whereas the Alamouti technique performs STBC operations on both transmission sequences. This neat feature simplifies the implementation process at the transmitter. To illustrate the differences between the two diversity schemes, Table 1 shows the comparison.

LTE SFBC		Alamouti		
Ant 1	Ant 2	Ant 1	Ant 2	
s_{2i+1}	$-s_{2i+2}^*$	s_{2i+1}	s_{2i+2}	$\mathbf{d}(2i+1)$
s_{2i+2}	s_{2i+1}^*	$-s_{2i+2}^*$	s_{2i+1}^*	$\mathbf{d}(2i+2)$

Table 1: Comparison between LTE SFBC and the Alamouti diversity technique

4.5.3 Resource Element Mapping

Resource element mapping refers to the process of allocating physical channels and physical signals into specific locations of what has been defined in [20] as the time-frequency resource grid. The resource grid spans across the entire time-frequency space in a 10 millisecond FDD frame. The downlink resource grid corresponding to one subframe in a 10 millisecond FDD frame is shown in Figure 17.

The smallest unit in the resource grid is referred to as a resource element (RE), which is highlighted in blue. A small collection of several REs in time and frequency has been defined as a resource block, which is depicted by the red box in Figure 17. REs across the vertical (frequency) axis represent subcarriers and those on the horizontal (time) axis are referred to as OFDM symbols. There are a total of $N_{RB}^{DL} \times N_{SC}^{RB}$ subcarriers along the frequency axis, where N_{SC}^{RB} represents the number of subcarriers in a resource block and N_{RB}^{DL} represents the total number of downlink resource blocks allocated for the specific channel bandwidth configuration (N_{RB}^{DL} is designated in the standard as the transmission bandwidth configuration). The channel bandwidth configurations supported are described in the table below [1].

Channel Bandwidth (MHz)	1.4	3.0	5.0	10	15	20
Transmission bandwidth configuration, N_{RB}^{DL}	6	15	25	50	75	100

Table 2: Allowable channel bandwidth configurations

The number of downlink OFDM symbols, N_{sym}^{DL} , for normal CP and subcarrier spacing, $\Delta_f = 15kHz$, should be set to 7. Also, under this CP configuration, $N_{SC}^{RB} = 12$. There are 140 OFDM symbols along the time-domain axis in a 10 millisecond FDD frame. Unless specified otherwise, we will keep this configuration

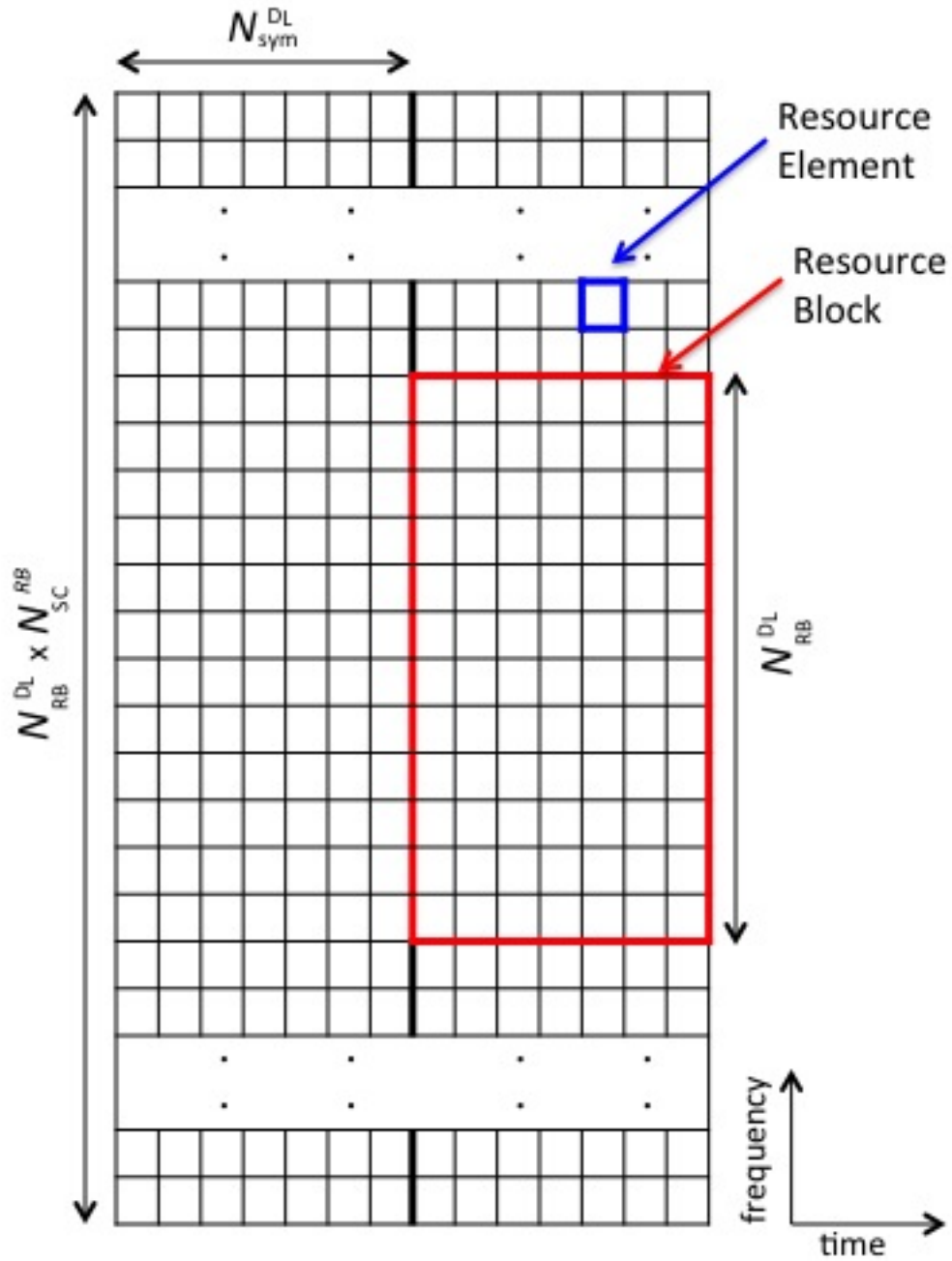


Figure 17: Time-frequency resource grid corresponding to one subframe

throughout our analysis and assessment of the LTE testbed.

In principle all physical signals are mapped to the time-frequency grid once they have been generated by the process described in this section. For our purpose

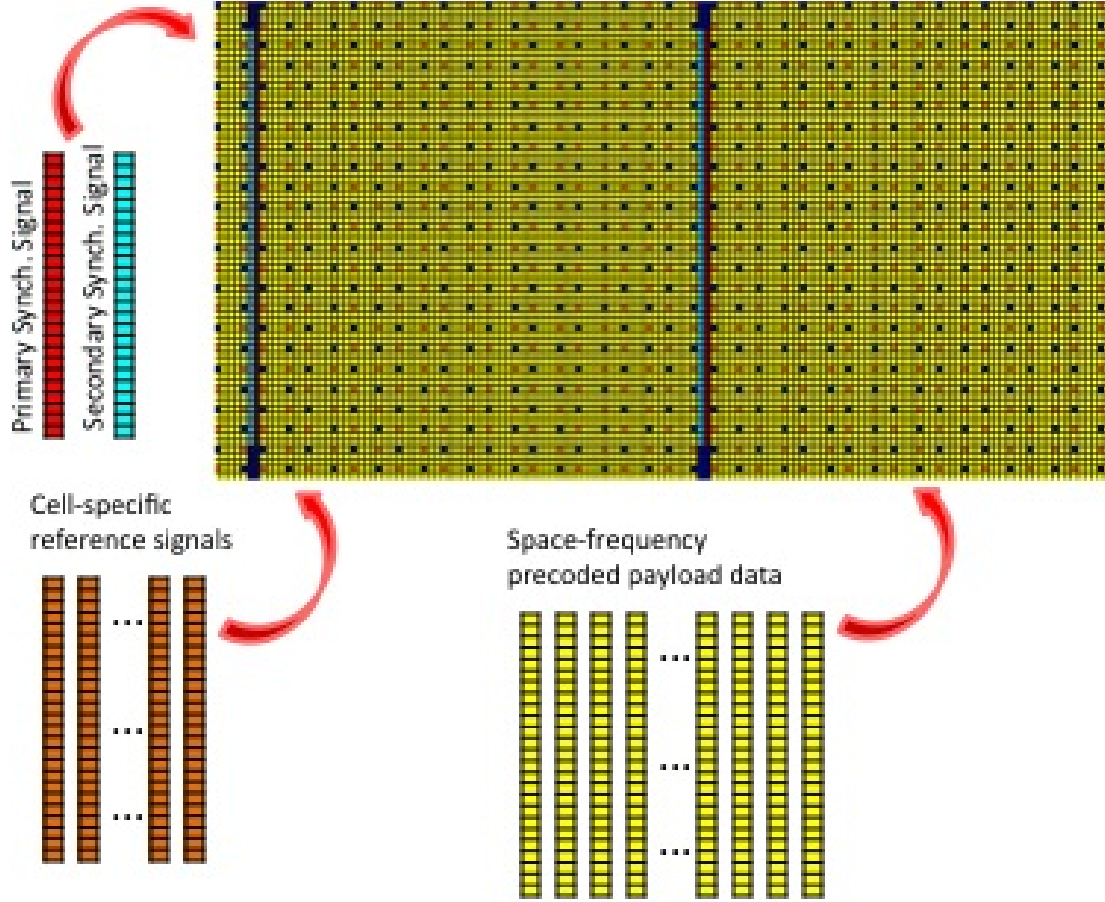


Figure 18: Mapping of different physical signals onto the time-frequency grid

however, this mapping is restricted to SFBC payload data, primary and secondary synchronization signals, and cell-specific reference signals. To illustrate how to map these set of signals onto the time-frequency resource grid, Figure 18 shows an example of the time-frequency resource grid using $N_{RB}^{DL} = 6$ and normal cyclic prefix. The REs in yellow define the SFBC payload data that will be used to compute the error rate measurements at the receiving end. Cell-specific reference signals are scattered throughout the entire grid. These signals are unique to each time slot and they are required for channel coefficient estimation and frequency-domain equalization at the receiver. Note that cell-specific reference signals for each of the antenna ports have to be specifically located in the grid so they don't overlap once combined at the receiver. For example, the resource element mapping depicted in Figure 18 is unique to antenna 1 so the allocation of cell-specific reference signals for antenna 1 is shown in orange and the location of reference signals for antenna 2 (shown in navy blue) are left out empty. Evidently, the resource element mapping for each of the 2 transmission chains is done in parallel and a similar time-frequency grid is constructed for antenna 2.

The last set of physical signals incorporated into the grid are synchronization

signals. Each synchronization signal is allocated once every 5 milliseconds in the FDD frame. The process to generate these signals as well as the cell-specific reference signals will be described in sections 4.6 and 4.7.

4.5.4 OFDM Baseband Signal Generation

The OFDM baseband signal generation sets the boundary between the frequency-domain and time-domain processing of physical channels. The OFDM signal generation at the transmitter is based on the IFFT. In section 6.12 of [20] the definition of the continuous-time OFDM symbol l in a downlink slot is given by,

$$\mathbf{y}_l(t) = \sum_{k=1}^{\lceil N_{RB}^{DL} N_{sc}^{RB} / 2 \rceil} a_{k+\lfloor N_{RB}^{DL} N_{sc}^{RB} / 2 \rfloor - 1, l} e^{j2\pi k \Delta f (t - N_{CP, l} T_s)} + \sum_{k=-\lfloor N_{RB}^{DL} N_{sc}^{RB} / 2 \rfloor}^{-1} a_{k+\lfloor N_{RB}^{DL} N_{sc}^{RB} / 2 \rfloor, l} e^{j2\pi k \Delta f (t - N_{CP, l} T_s)} \quad (4.2)$$

for $0 \leq t < (N_{CP, l} + N)T_s$ and $N_{CP, l}$ is given by Table 6.12-1 in [20]. The variable N is set depending on the IFFT size in use and although the standard defines $N = 2048$, it is possible to use a smaller IFFT size and still retain the same slot duration of 0.5 milliseconds and subcarrier spacing $\Delta f = 15 \text{ kHz}$ by applying a different OFDM sampling frequency [23] and scaling $N_{CP, l}$ according to the desired IFFT size. To obtain a discrete-time representation of (4.2), we could sample the continuous-time expression every T_s and generate a $(N + N_{CP, l})$ -sample representation. This operation can be denoted as,

$$\mathbf{y}_l[n] = \mathbf{y}_l(nT_s) = \sum_{k=1}^{\lceil N_{RB}^{DL} N_{sc}^{RB} / 2 \rceil} a_{k+\lfloor N_{RB}^{DL} N_{sc}^{RB} / 2 \rfloor - 1, l} e^{j2\pi k(n - N_{CP, l})/N} + \sum_{k=-\lfloor N_{RB}^{DL} N_{sc}^{RB} / 2 \rfloor}^{-1} a_{k+\lfloor N_{RB}^{DL} N_{sc}^{RB} / 2 \rfloor, l} e^{j2\pi k(n - N_{CP, l})/N} \quad (4.3)$$

where $0 \leq n < N + N_{CP, l}$ and $T_s = (N\Delta f)^{-1}$. N in this case is treated as the desired IFFT size. This representation of the OFDM baseband signal resembles equation (2.3) where the term $n - N_{CP, l}$ is used to include the cyclic prefix samples.

The samples $a_{k, l}$ are taken from the time-frequency resource grid as shown in Figure 19. Each OFDM symbol column in the resource grid is represented by the sequence $y_l[n]$, and the resource elements are taken sequentially from $k = 0$ and up. After the IFFT operation, the samples are parallel-to-serially converted, as shown in Figure 4, and the results yields a sequence in time-domain that is N samples per T_o seconds, where $T_o = 1/\Delta f$.

The N -point IFFT is commonly implemented with the standard Cooley-Turkey radix-2 FFT algorithm which requires N to be a power of 2 [24]. So if the number of used subcarriers is less than the IFFT size, then the sequence containing the subcarriers samples must be padded with zeros in order to make the sequence length

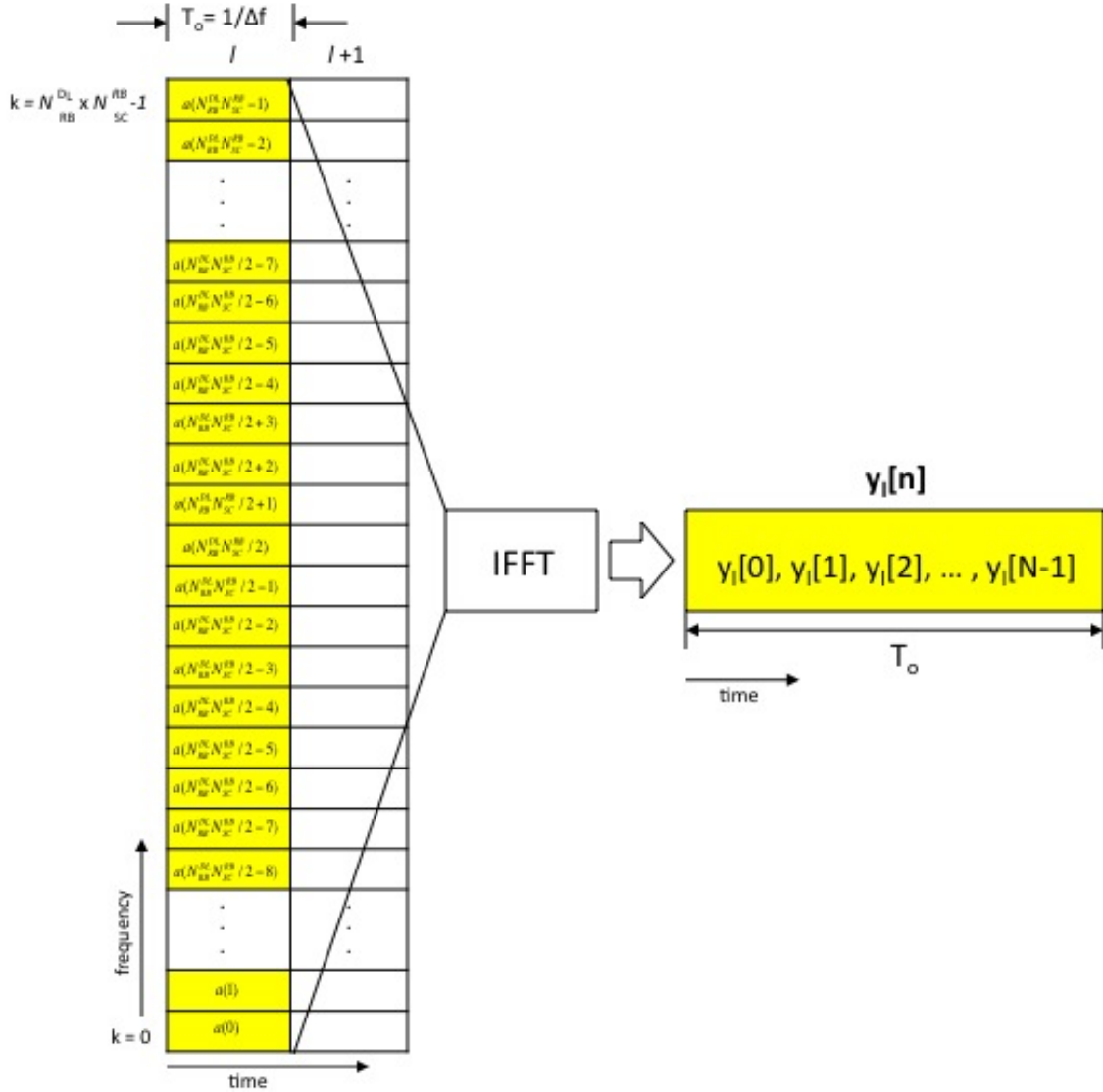


Figure 19: The OFDM baseband signal generation procedure

the same as the IFFT size. For example, if the channel bandwidth is 1.4 MHz, the number of subcarriers in the frequency-domain will be 72 (for normal CP). With these many subcarriers, the IFFT size must be $2^7 = 128$ since it's the minimum size that could fit all 72 subcarriers. This configuration yields $128 - 72 = 56$ subcarriers that will have to be padded with zeros so to fit the FFT size. These zero-padded subcarriers have no effect on the effective bandwidth, and are generally added to the beginning and the end of the occupied subcarriers so that they are as far from DC.

4.5.5 Cyclic Prefix Insertion

The last step of the baseband physical channel processing, before sending the time-domain samples through the USRP boxes, is to append a cyclic prefix to the time-domain samples coming from the OFDM operation. As mentioned in section 2.1.1, the cyclic prefix is an instrumental tool to combat the effects of ISI due to time dispersion of the channel. The cyclic prefix is generated from the last μ samples of $y_l[n]$ and are added at the beginning of $y_l[n]$ so that the newly-formed, time-domain sequence looks like $\{y[N-\mu], y[N-\mu+1], \dots, y[N-1], y[0], \dots, y[N-1]\}$. Table shows the number cyclic prefix samples for different channel bandwidth configurations. Note that there are two definitions for CP length under normal CP as shown in Table 6.12-1 of [20].

Channel BW (MHz)	1.4	3.0	5.0	10.0
N_{RB}^{DL}	6	15	25	50
Occupied subcarriers	72	180	300	600
IFFT size	128	256	512	1024
CP samples for 1 st OFDM sym.	10	20	40	80
CP samples for other OFDM sym.	9	18	36	72

Table 3: CP length for different channel bandwidth configurations

4.6 Overview of Synchronization Signals Processing

Synchronization signals are used to synchronize users in time and frequency, and to allocate 10 millisecond frames streaming down from their serving base station. In LTE, it is possible to uniquely assign 504 cell identities. Each cell identity can be constructed from a pair of primary and secondary synchronization sequences, and each user in a cell must detect these set of sequences from the data received from the base station by a process called cell search procedure.

In order to simplify the cell search process for the users in a cell, the 504 cell identities are grouped into 168 cell-identity groups, with each group containing 3 unique identities. During the cell search operation, users can identify one of the 3 unique identities by correlating the received data to a set of primary synchronization signals that they know and can generate on their own. Correlation can be done both in the time and frequency domain. Once a user has located one of the 3 unique primary synchronization sequences, the user can determine the starting location of one of the two 5 millisecond subframes available within a frame.

The final step of the cell search is performed by identifying one of the 168 cell-identity groups through the secondary synchronization signal. This process is done by generating a scrambling code from the physical-layer identity found through the primary sequence and scrambling it with a set of m-sequences generated using the

cell-identity group numbers. After finding the cell-identity group m-sequence with the strongest response, users can retrieve their cell id and identify the location of an entire frame.

Primary Sequence Generation and Mapping

The set of primary sequences used in the cell search process can be generated from a frequency-domain Zadoff-Chu complex sequence according to,

$$z_p(k) = \begin{cases} e^{-j \frac{\pi u_r k(k+1)}{63}} & \text{for } k = 0, 1, \dots, 30 \\ e^{-j \frac{\pi u_r (k+1)(k+2)}{63}} & \text{for } k = 31, 32, \dots, 61 \end{cases} \quad (4.4)$$

where one of three Zadoff-Chu root indices $u_r = \{25, 29, 34\}$ corresponds to one unique sequence, $N_{ID}^{(2)}$, on the cell-identity groups. Zadoff-Chu sequence are favored over other forms of pseudo-noise sequences due to its constant-amplitude, and zero auto-correlation (CAZAC) properties [25]. Figure 20 shows an example of a Zadoff-Chu sequence generate using a root index = 29. Note that the elements in the sequence lie along the unit-circle in the complex plane thus providing a constant amplitude sequence.

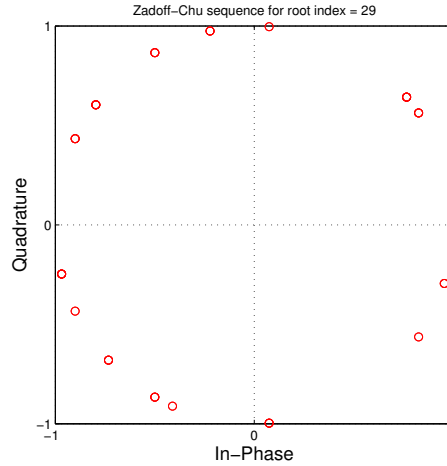


Figure 20: Example of a Zadoff-Chu sequence with root index = 29

Once the primary sequence has been generated using the Zadoff-Chu sequence definition outlined above, the mapping into the resource grid shall be included twice in a 10 millisecond frame; in the last OFDM symbol of slots 1 and 11 (see Figures 14 and Figure 18 to get perspective of such locations).

Secondary Sequence Generation and Mapping

The secondary synchronization sequence is an interleaved concatenation of two length-31 binary sequences, $s_0^{(m_0)}$ and $s_1^{(m_1)}$. The superscripts m_0 and m_1 are based

on the cell-identity group ID and their values can be found in Table 6.11.2.1-1 of [20]. To complete the generation of the secondary synchronization sequence, the concatenated sequence is then scrambled with the scrambling code, c_0 , for even elements in the sequence and with scrambling codes, c_1 , $z_1^{(m_0)}$, and $z_1^{(m_1)}$ for the odd elements. Furthermore, the secondary synchronization sequence differs between subframe 1 and subframe 6 according to,

$$z_s(k_{\text{even}}) = \begin{cases} s_0^{(m_0)}(k)c_0(k) & \text{for subframe 0} \\ s_1^{(m_1)}(k)c_0(k) & \text{for subframe 5} \end{cases} \quad (4.5a)$$

$$z_s(k_{\text{odd}}) = \begin{cases} s_1^{(m_1)}(k)c_1(k)z_1^{(m_0)}(k) & \text{for subframe 0} \\ s_0^{(m_0)}(k)c_1(k)z_1^{(m_1)}(k) & \text{for subframe 5} \end{cases} \quad (4.5b)$$

The sequence generators used to construct the scrambling sequences, and the length-31 sequences $s_0^{(m_0)}$ and $s_1^{(m_1)}$, are depicted in Figure 21. These set of sequences belong to a class of pseudo-random binary sequences called maximum-length sequences (or m-sequences). M-sequences have many desirable properties [26] useful in wireless communications: 1) they are well balanced, meaning that the number of 1s and 0s in the sequence is more-or-less the same, 2) the number of consecutive 0s or 1s (also called run-length) is generally short, 3) and most importantly, they have good autocorrelation response.

One important step when generating the set of binary sequence described above is to apply a fixed cyclic shift to their generator polynomial in order to obtain different outputs. This cyclic shift represents the number of transitions in the shift register after which the output is generated. The two sequences $s_0^{(m_0)}$ and $s_1^{(m_1)}$ are defined as two different cyclic shifts of the sequence $\tilde{s}(k)$ according to,

$$s_0^{(m_0)}(k) = \tilde{s}((k + m_0) \bmod 31) \quad (4.6a)$$

$$s_1^{(m_1)}(k) = \tilde{s}((k + m_1) \bmod 31) \quad (4.6b)$$

where $\tilde{s}(k) = 1 - 2x(k)$ and $x(k)$ is generated using the generator shown at the top of Figure 21 and initialised with 16. The cyclic shifts are represented by m_0 and m_1 which, once again, depend on the value of the cell-identity group ID.

The cyclic shifts on the scrambling sequences $c_0(k)$ and $c_1(k)$ depend on one of the unique physical-layer identities, $N_{ID}^{(2)}$, assigned to the primary synchronization sequence. These two sequence shall be generated according to,

$$c_0(k) = \tilde{c}((k + N_{ID}^{(2)}) \bmod 31) \quad (4.7a)$$

$$c_1(k) = \tilde{c}((k + N_{ID}^{(2)} + 3) \bmod 31) \quad (4.7b)$$

where $\tilde{c}(k) = 1 - 2x(k)$ and $x(k)$ is generated using the generator shown in the middle of Figure 21 and initialised with 16.

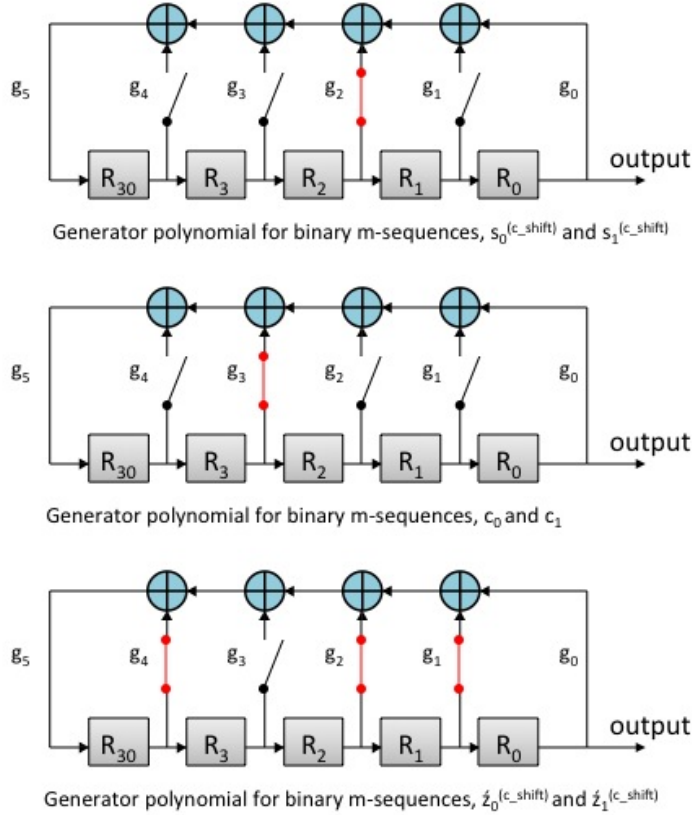


Figure 21: Length-31 Gold code structure used for generation of cell-specific reference signals

The last set of scrambling sequences $z_1^{(m_0)}(k)$ and $z_1^{(m_1)}(k)$ are defined by a cyclic shift of the sequence $\tilde{z}(k)$ according to,

$$z_0^{(m_0)}(k) = \tilde{z}((k + (m_0 \bmod 8)) \bmod 31) \quad (4.8a)$$

$$z_1^{(m_1)}(k) = \tilde{z}((k + (m_1 \bmod 8)) \bmod 31) \quad (4.8b)$$

where $\tilde{z}(k) = 1 - 2x(k)$ and $x(k)$ is generated using the generator shown at the bottom of Figure 21 and initialised with 16.

The mapping of secondary synchronization signals into the resource grid shall be included twice in a 10 millisecond frame; one symbol before the last OFDM symbol of slots 1 and 11, adjacent to the location of the primary synchronization signals (see Figures 14 and Figure 18 to get perspective of such locations).

4.7 Overview of Cell-Specific Reference Signals Processing

As mentioned earlier, cell-specific reference signals are important for channel estimation at the receiving end. Cell-specific reference signals are generated using a

length-31 Gold sequence generator which consist of a pair of m-sequence generators, G_1 and G_2 , as shown in Figure 22. All the arithmetic performed by the gold sequence generator is based on modulo-2 and the output is captured after 1600 cyclic shifts to ensure good transition density and randomness in the code. The first generator shall be initialised with 1 while the second generator must be initialised at the start of each OFDM symbol using the c_{init} coefficient described in section 6.10.1.1 of [20].

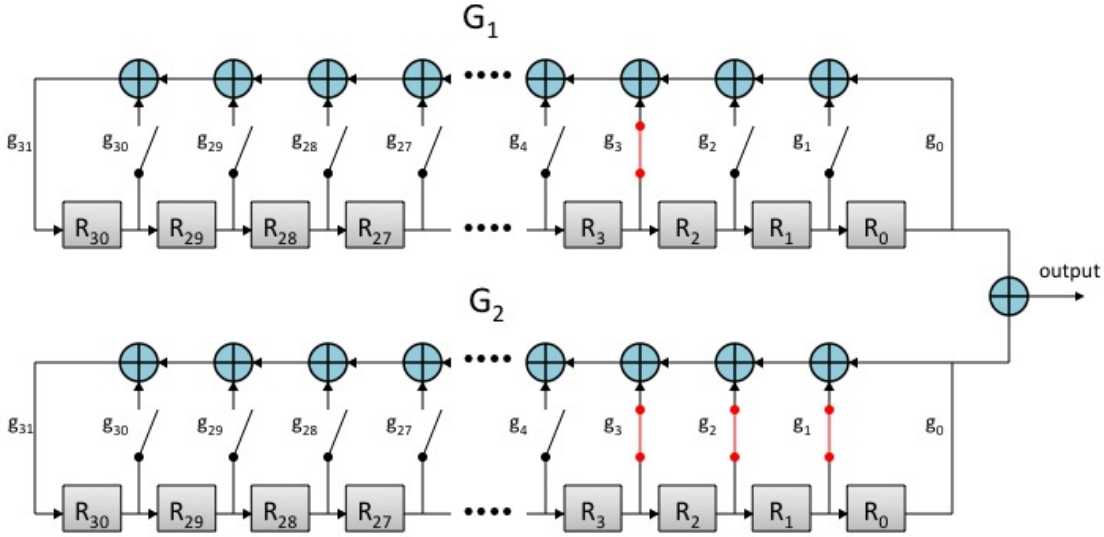


Figure 22: Length-31 Gold code structure used for generation of cell-specific reference signals

There are 140 possible sequences that could be generated using different values of c_{init} , however, only some of these sequences are actually mapped into the resource grid (as shown in 23). The output of the gold-code generator is in binary form, so before mapping the output binary sequence to the resource grid, bits must be converted to a complex form. This step is done by doing a simple modulation mapping operation in the binary sequence similar to the modulation mapping procedure for QPSK (see section 6.10.1.1 in [20]).

The mapping of cell-specific reference signals into resource elements in the resource grid is dependent upon the number of antennas ports in use. For transmit diversity techniques with two antenna ports an example of the reference signals mapping is illustrated in Figure 23. Note that the location across OFDM symbols is the same for both antenna ports and the locations differ across subcarriers in the frequency axis. The REs in dark blue are zero-filled so that the pilots from the other antenna port don't get interference and can be easily extracted at the receiving end.

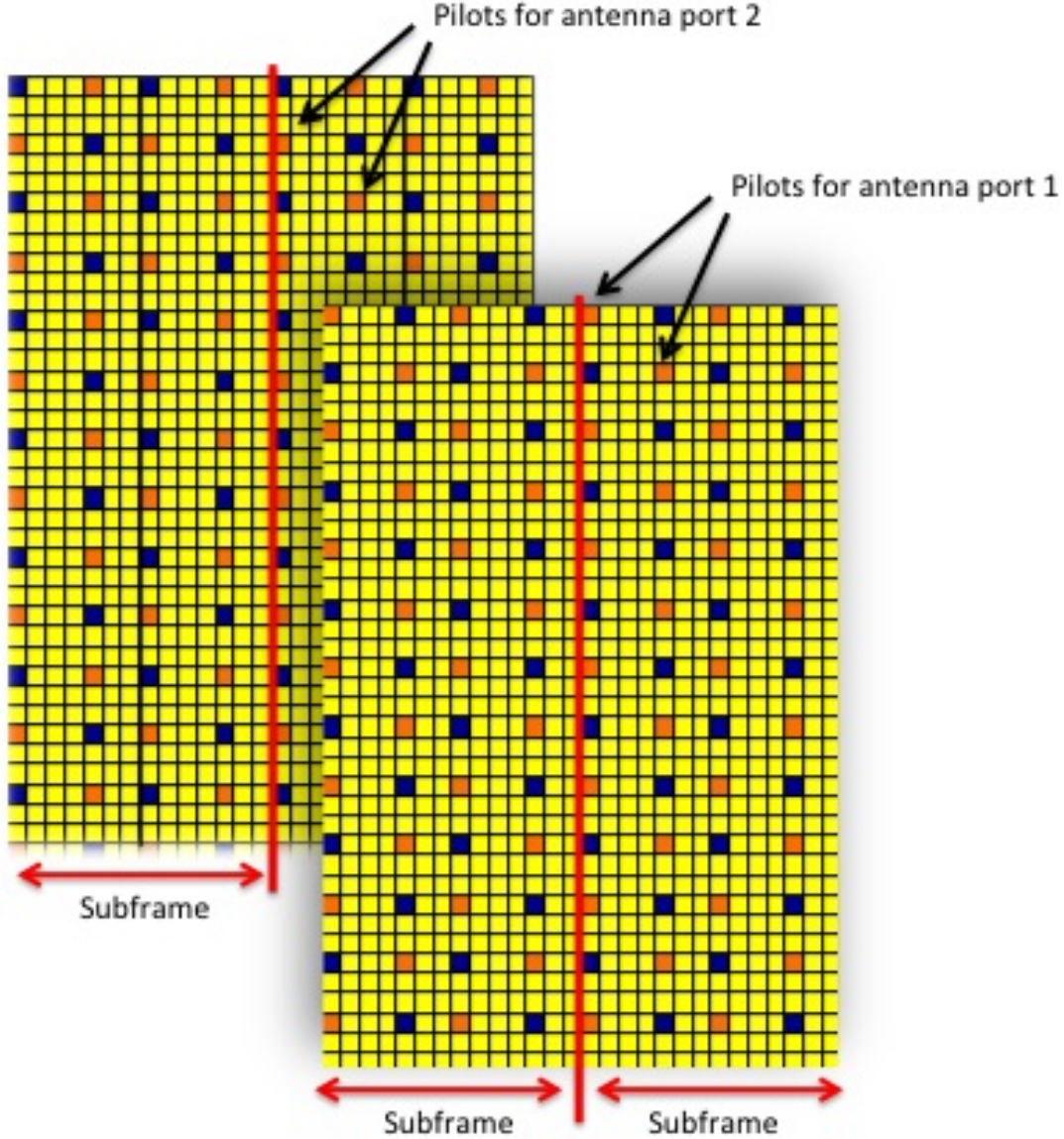


Figure 23: Cell-specific reference signal mapping for transmit diversity using 2 antennas

4.8 Transmission Bandwidth Adjustments

The transmission bandwidth has been defined in [1] according to Figure 24. The transmission bandwidth is the total bandwidth occupied by all the active resource blocks utilised for a given transmission bandwidth configuration, N_{RB}^{DL} (see Table 2). In our setup, we continuously transmit all the resource blocks allowed for a given transmission bandwidth configuration, therefore, the total transmission bandwidth can be formulated by multiplying the subcarriers separation, Δ_f , with N_{SC}^{RB} and N_{RB}^{DL} .

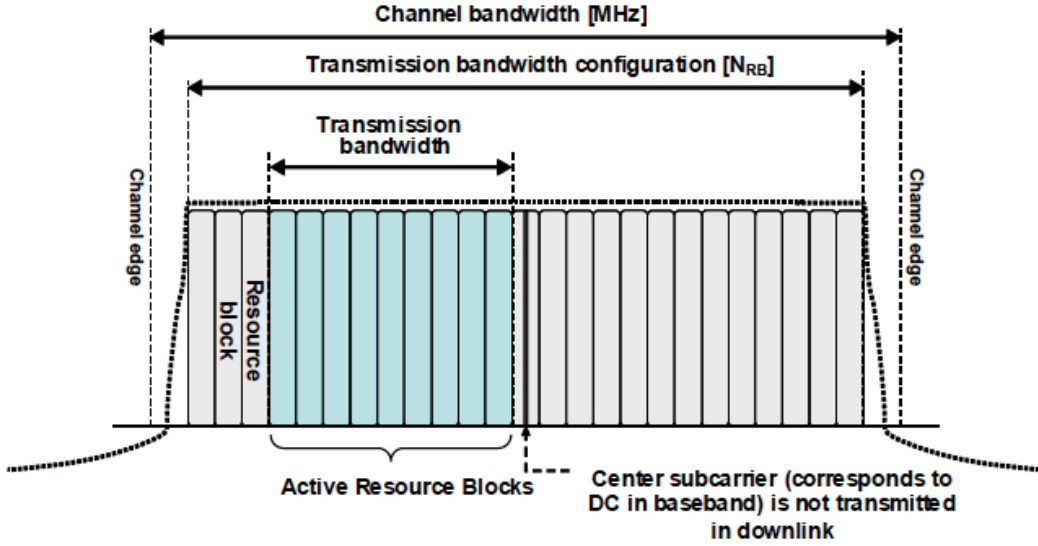


Figure 24: Definition of channel bandwidth and transmission bandwidth configuration for one E-UTRA carrier [1]

To set the sampling rate for a desired transmission bandwidth, one must take into account the number of samples included in a 10 millisecond frame. For example, if we consider a channel bandwidth of 1.4 MHz and normal CP, the transmission bandwidth should be 1.08 MHz since $\Delta_f = 15 \text{ kHz}$, $N_{RB}^{DL} = 6$, and $N_{SC}^{RB} = 12$. The sampling rate for this transmission bandwidth is 1.92 MSps and can be computed using $20 \cdot [(N_{sum}^{DL} - 1) \cdot (N_{FFT} + N_{CP2}) + (N_{FFT} + N_{CP1})] / (10 \text{ milliseconds})$ where $N_{sum}^{DL} = 7$, N_{FFT} is the IFFT size used, N_{CP1} is the number of CP samples in the 1st OFDM symbol, and N_{CP2} is the number of CP samples in the 2nd through 7th OFDM symbols.

The digital up-conversion (DUC) inside the USRP boxes operates on a sampling rate of 100 MSps. The DUC uses a 4 stage cascaded integrator-comb filter (CIC) and 2 half-band (HB) filters each working in interpolation mode [27]. To set the transmission sampling rate of the input signal coming to the USRP boxes, we can divide 100 MSps by the desired interpolation factor, n , which yields a rate close to the desired sampling rate. However, it has been recommended in [27], that the factor n be chosen to be a multiple of 4 so the DUC process makes full utilisation of CIC and HB filters.

If we constrain the transmission sampling rate to $100/n$ MSps, where n is a multiple of 4, it is difficult to exactly match the desired sampling rate (computed using the equation given previously). Consequently, the actual transmission bandwidth for each of the channel configurations expands or contracts relative to the desired transmission bandwidth thus changing the actual subcarrier separation. However, it

is worth mentioning that although the subcarrier spacing is slightly off from 15kHz, the orthogonality in the subcarriers is retain since the OFDM symbol period is kept inversely proportional to the adjusted subcarrier spacing.

Channel BW	Desired Samp. Rate	Desired Tx BW	Actual Samp. Rate
1.4 MHz	1.92 MSps	1.08 MHz	$100/52 = 1.9231$ MSps
3.0 MHz	3.84 MSps	2.7 MHz	$100/28 = 3.5714$ MSps
5.0 MHz	7.68 MSps	4.5 MHz	$100/12 = 8.3333$ MSps
10 MHz	15.36 MSps	9.0 MHz	$100/8 = 12.5$ MSps

Table 4: Sampling rate supported by the USRP N200 when the DUC interpolation factor is a multiple of 4.

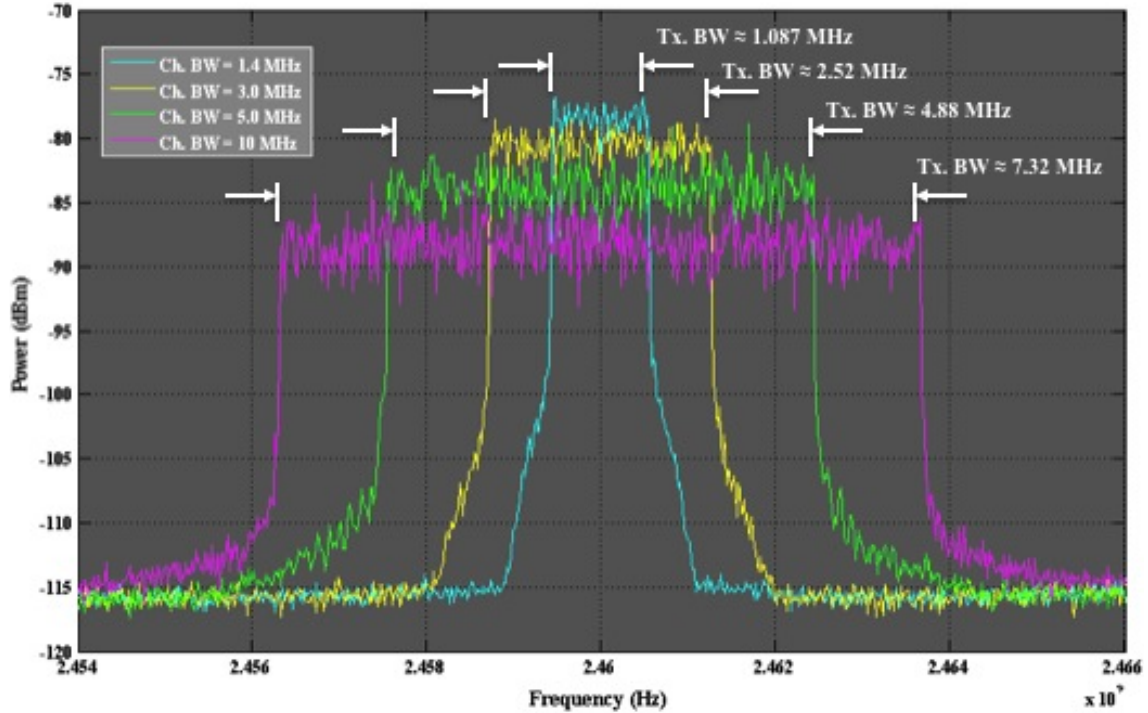


Figure 25: Transmission bandwidth adjustments due to the actual sampling rates defined in Table 4.

Table 4 shows the list of supported transmission sampling rates that use an interpolation factor multiple of 4 in the DUC operation. Similarly, Figure 26 show the adjusted transmission bandwidth for each of supported transmission sampling rates. The power spectrum for each of the channel bandwidth configurations, was measured using a signal spectrum analyser observing the data coming from the the USRP boxes in the transmitter side, and the spectrum plots shown in the figure are averaged over time to get the distinctive OFDM shape observed.

5 MISO LTE Receiver Testbed

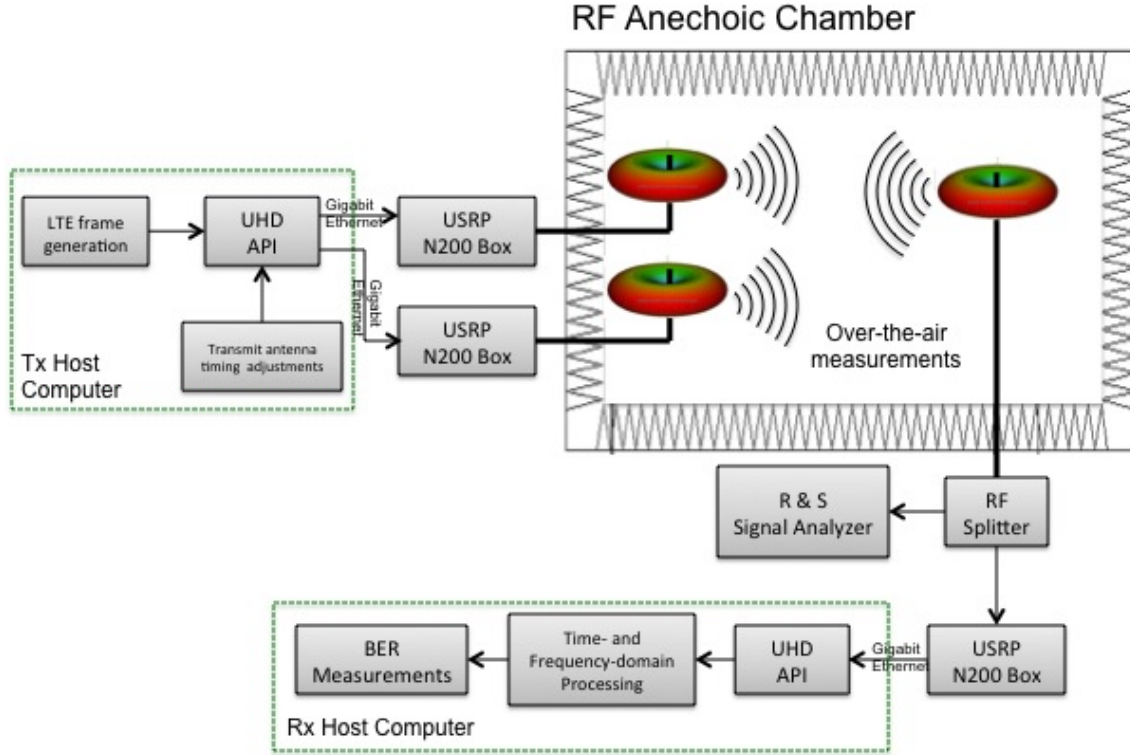


Figure 26: MISO LTE receiver testbed block diagram

This chapter describes the MISO LTE receiver setup with the transmit and receive antennas inside an RF anechoic chamber. The receiving process can be divided into two parts: time- and frequency-domain operations, just like the transmission side described in the previous chapter. The receiver host computer is connected to a single N200 USRP box that collects data transmitted from a pair of USRP boxes. The data from the transmitter is sent over-the-air, inside the anechoic chamber as shown in Figure 26 and at the top of Figure 27. The BER measurements from this setup serve to validate the system in a non-fading environment, which will be compared against the theoretical AWGN BER curves provided in Chapters 2 and 3.

Inside the RF chamber, the transmit antennas are separated 1.7 meters from each other and the separation between transmit antennas and receive antennas is approximately 5.0 meters (see top of Figure 27). The antennas used for the measurements are omni-directional, vertical antennas with a 3 dBi gain and VSWR shown in Figure 28. The centre carrier frequency use in this set of measurements was set to 2.46 GHz. The Rhode & Schwarz[®] FSV Signal and Spectrum Analyser serves to confirm the OFDM spectral shape observed at the receiving end. Furthermore, the transmit and receive USRP reference clock connectors are connected to an external



Figure 27: MISO LTE receiver testbed setup with RF anechoic chamber

sinusoidal signal generator with 15 dBm amplitude and a frequency of 10 MHz. This is to improve the accuracy of the carrier frequency generator inside the USRP boxes (see pictures at the bottom of Figure 27). The set of BER measurements collected inside the RF chamber correspond to a channel bandwidth of 1.4 MHz which occupies 72 subcarriers and normal CP length with 15 kHz subcarrier spacing (see Table 3). Also, the measurements will be restricted to only two modulation schemes: QPSK and 16QAM.

An important characteristic about the transmitter in Figure 26 that was not mentioned in the previous chapter, is the capability of making timing adjustments to one of the transmission chains in order to align the received data streams coming from the transmit USRP boxes. This procedure will be explained later in section 5.1.

The remainder of this chapter includes three main sections. Section 5.1 which provides detailed description of the time-domain processing performed by the receiver host computer, Section 5.2 which outlines the frequency-domain processing, and Section 5.3 which provides the BER measurements results.

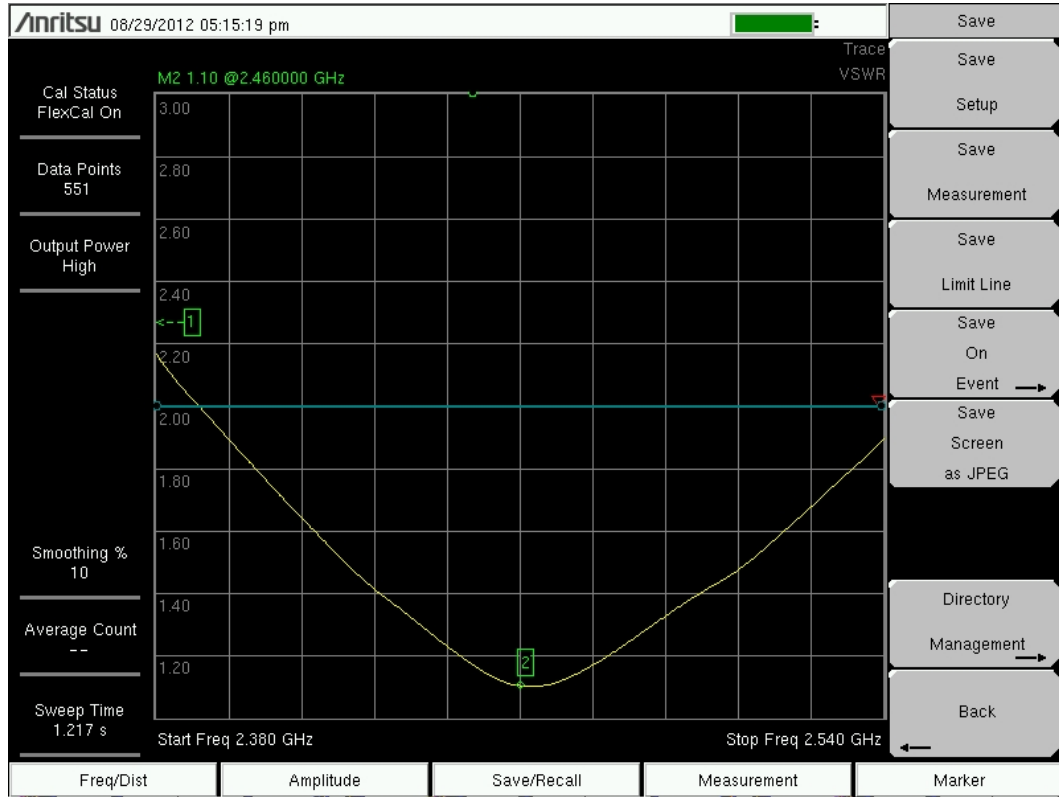


Figure 28: VSWR of the 3 dBi vertical antennas used in our setup

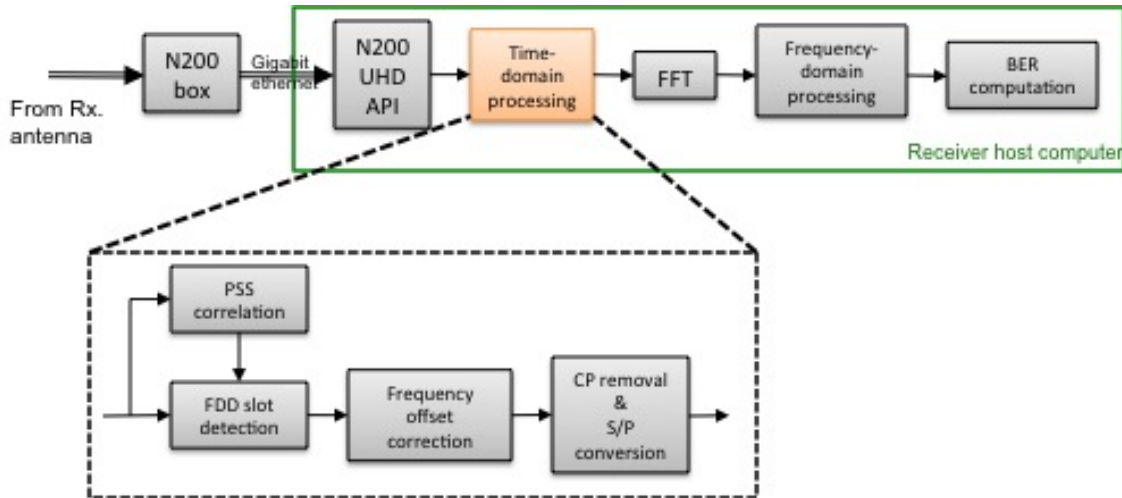


Figure 29: Block diagram of the time-domain processing at the receiver

5.1 Time-domain Processing

The receiver time-domain processing of the MISO LTE testbed is shown in Figure 29. The main task performed in the time-domain is to find the location of the FDD slots containing the PSS so that frame synchronization can be achieved. This is done by correlating the PSS with incoming samples from the receiving USRP box.

Recall from previous chapter that the PSS are located in the 7th OFDM symbol of the 1st and 11th slot. However, once any of the two locations is found through the cross-correlation peak detection procedure, it is not possible to deduce which location the correlation peak belongs to since the PSS used on each 5 millisecond subframe are identical. The SSS helps identify which half of the 10 millisecond frame and more on this will be outlined in Section 5.2

Since we are fully utilising the entire resource grid in our setup to compute BER measurements, slot boundaries can be determined through the PSS correlation but, once again, it is not possible to identify the exact slot number in the 10 millisecond FDD frame. Yet, the detection of slot boundaries is extremely useful for time-domain frequency offset correction. The frequency offset correction subsystem shown in the block diagram of Figure 29 is used to correct any fractional frequency offset with knowledge of the slot boundaries and their corresponding CP [28]. Recall that the frequency offset comes from inaccuracies in the carrier frequency generation or due to the Doppler frequency shift generated in mobility scenarios. In our static case, the frequency offset comes from inaccuracies of the carrier frequency generation process in both the transmitter and receiver. However, the external reference clock used in our setup should minimise or almost eliminate the need for carrier frequency offset correction.

Shall we have not used an external reference clock in our setup, then, according to [29], the USRP N200 has a frequency accuracy of 2.5 ppm, so at 2.46 GHz, we can expect a carrier frequency variation of ± 6.15 kHz. In the worst case condition, the frequency offset experience due to the accuracy of the LO in both transmitter and receiver side could be a little over 12 KHz.

The last step in the time-domain processing is to remove the CP and to do a serial-to-parallel conversion so the FFT operation can reconstruct the time-frequency resource grid.

5.1.1 Transmission Timing Mismatch Calibration

The transmission host computer shown in Figures 26 sends data sequentially to each transmit USRP box. It does so by transmitting small pieces of data containing time-domain OFDM symbols for each transmission chain at a time through a network interface card that connects to each USRP box using a gigabit ethernet port. Therefore, there is an inherit data transmission misalignment between the two chains that propagates all the way to the receiving end.

An additional benefit of the PSS correlation process described above is to provide a measure of the transmission timing mismatch between the USRP boxes at the transmitter side. The timing mismatch can be calculated by computing the difference in time between adjacent correlation peaks observed from the output of the PSS correlator. If a timing mismatch is found, it can then be used to make

timing corrections in the transmitter. Transmitter synchronization at the receiver is important so that the received symbols from the pair of transmit antennas can be properly combined.

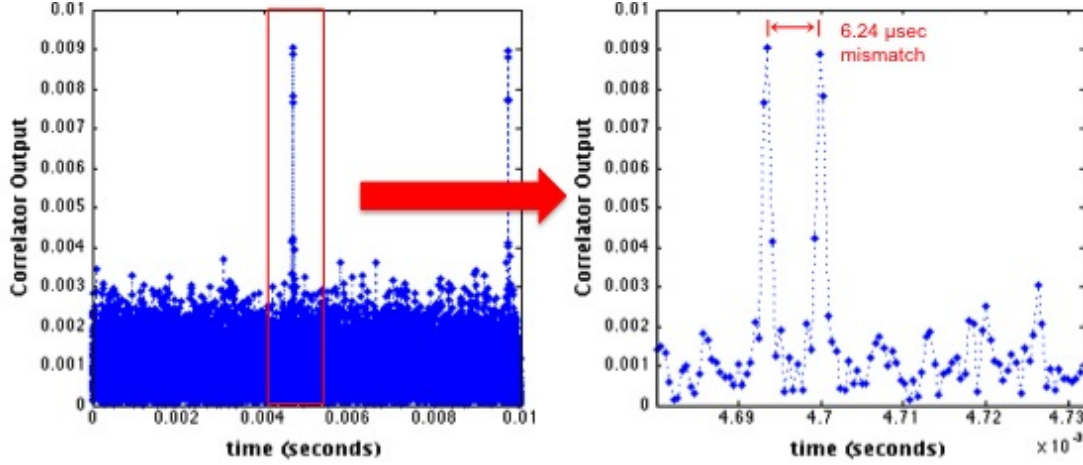


Figure 30: Magnitude of the PSS correlation plot for received samples with antenna transmission timing mismatch

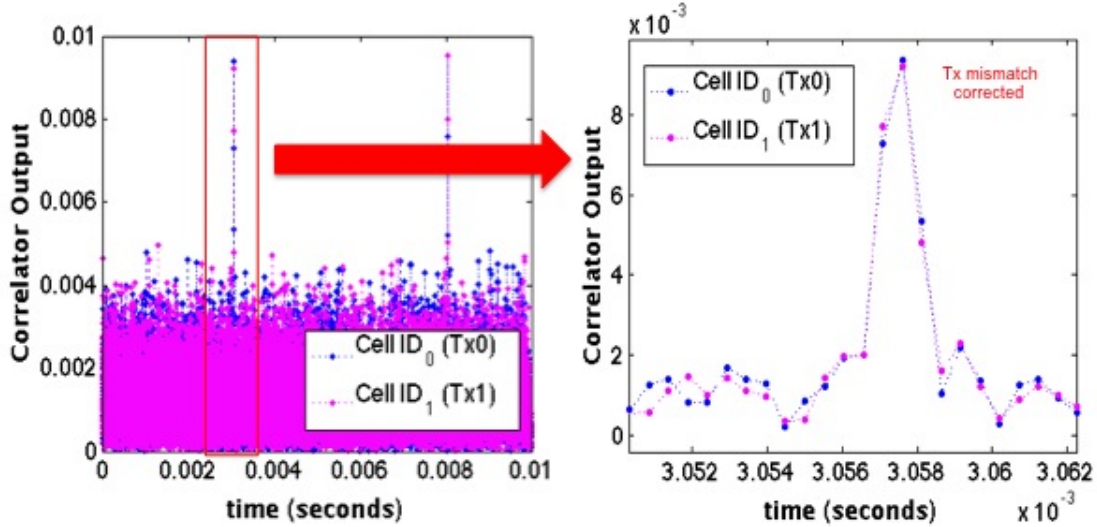


Figure 31: Magnitude of the PSS correlation plot for received samples with antenna transmission timing mismatch compensated

The plots in Figure 30 show the magnitude of the PSS correlation with a typical transmission timing mismatch without any correction. The plot on the left side shows the correlation peaks that represent the location of the PSS which are spaced 5 milliseconds apart from each other. From this correlation output, it is possible to determine the location of the slot boundaries yet it is not possible to label each correlation peak to be from the 1st slot or the 11th slot. Now, the correlation plot on

the right side offers a close-up on the first set of correlation peaks observed and provides a visual representation of the actual timing mismatch. Each correlation peak represents one of the transmission chains and their difference in time can be used to measure and correct the transmission timing mismatch experienced in the system. In this particular example, the transmission timing mismatch observed from the two transmitters using a 1.4 MHz channel bandwidth configuration was 6.24 μ seconds.

Figure 31 shows the magnitude of the PSS correlation once the transmission timing mismatch has been corrected. The timing mismatch calibration procedure is done by simply introducing a delay to the leading transmission chain in the transmitter configuration shown in Figure 26. To illustrate the timing alignment in Figure 31, we have purposely used two different PSS generated using different cell ids and computed two PSS correlations using each one; yet, the system described in this Chapter strictly uses cell id = 0. It is important to note that during our measurements, once the transmission timing mismatch had been calculated in the receiving end and then calibrated (corrected) in the transmitters, the transmitters did not misaligned and when they did, the timing mismatch observed was within one or two samples.

5.2 Frequency-domain Processing

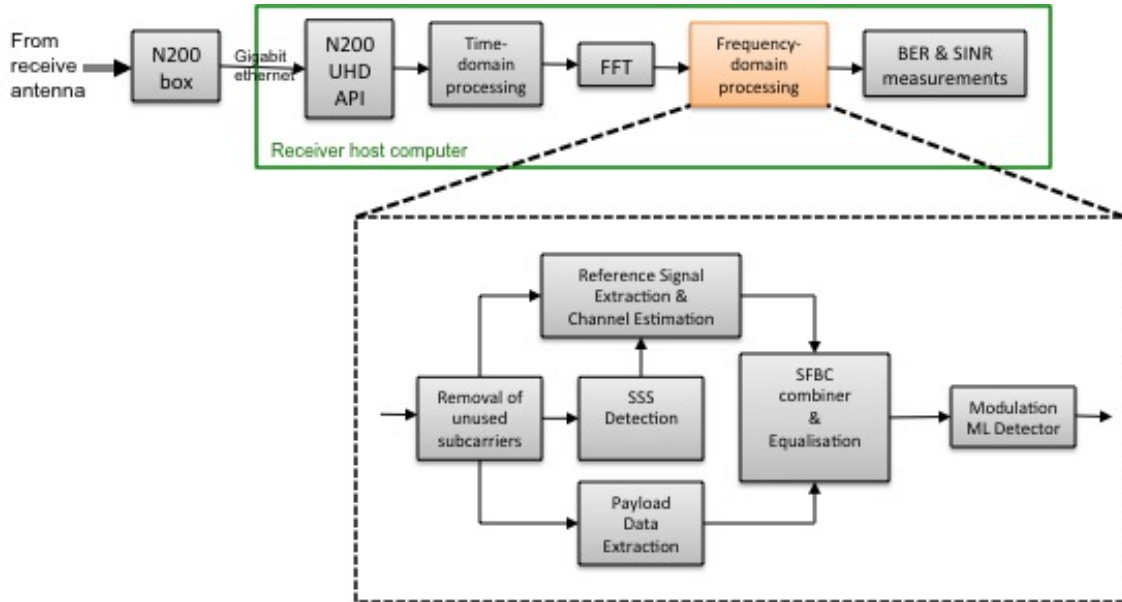


Figure 32: Block diagram of the frequency-domain processing at the receiver

The frequency-domain processing block diagram is depicted in Figure 32. This process starts once the FFT operations has been performed. The first step during the frequency-domain operation is to remove the unused subcarriers that were zero padded in order to fit the allocated subcarriers to the FFT size (see Section 4.5.4).

The next step in the process is to determine which half of the 10 millisecond FDD frame we are processing. The SSS is used for this purpose. Recall from equations (4.5a) and (4.5b) that the SSS is located next to the PSS in the 6th OFDM symbol of the 1st and 11th slot and that the sequences are different at these two locations. Using the cell id, we could generate the SSS and compare it to the one extracted from the current 5 millisecond subframe being processed. The one that provides the greatest response yields the slot numbers that need to be further processed. The operation to determine which half of the 5 millisecond subframe to consider is simple.

First, recall that the SSS is 62 elements long, so let $\mathbf{z}_{s1} = [z_{s1}(1), \dots, z_{s1}(62)]$ represent the SSS of the first half of the 5 millisecond subframe generated using (4.5a) and (4.5b), and let $\mathbf{z}_{s2} = [z_{s2}(1), \dots, z_{s2}(62)]$ represent the other SSS of the second half to the 5 millisecond subframe. Also, let $\mathbf{Y}_{(k,6)} = [Y_{(1,6)}, \dots, Y_{(62,6)}]$ represent the SSS extracted from the 5 millisecond subframe being processed. By selecting the argument with the max response in equation (5.1) we should be able to determine were we are in the 10 millisecond FDD frame.

$$\arg \max \left(\left| \sum_{k=1}^{62} z_{s1}(k) Y_{(k,6)} \right|, \left| \sum_{k=1}^{62} z_{s2}(k) Y_{(k,6)} \right| \right) \quad (5.1)$$

the multiply and add operations in equation (5.1) work fairly well since the SSS are generated using pseudo-random binary m-sequences which have good autocorrelation properties. Therefore, the probability of choosing the wrong SSS location has a low probability of occurrence.

Having identified the slot number to be processed, the next thing in line is the estimation of channel coefficient using Cell-Specific Reference Signals for each of the antenna ports. This approach for channel coefficient estimation is often referred to as pilot-aided channel estimation, where we use the information of resource elements containing known pilots (or reference symbols) to make an educated guess about the channel coefficient response on the subcarriers containing non-pilots or payload data.

Channel estimation is important since it is a required parameter for the SFBC combiner and for time-frequency equalization. So channel estimation is therefore, a two-dimensional problem i.e., channel coefficients need to be estimated both in the frequency and the time axis in the resource grid. Furthermore, channel estimation relies heavily on the type of radio propagation channel, thus it is often designed based on the statistics of the wireless environment to be expected [30].

Consequently there are many flavours and procedures to estimate the channel coefficients ranging from simple linear interpolation techniques, to more robust least-squares methods based on orthogonal polynomials, to highly complex Wiener filtering techniques using two-dimensional statistics of the channel which is optimal in the MMSE sense [2], [31]. In our approach, we favour the channel estimation based on linear interpolation techniques since our goal gravitates more towards improving

the BER using antenna diversity techniques rather than improving it using complex methods for channel estimation. Though it is also an interesting topic that could be investigated in the future.

So as mentioned earlier, channel estimation is a two-dimensional problem. Yet it can be broken down into two one-dimensional approaches: first we do linear interpolation using two adjacent pilot subcarriers in the frequency domain and later we use the two adjacent OFDM columns of pilot subcarriers to do time-domain linear interpolation. It is important to note that this type of pilot-based linear interpolation approach provides limited noise reduction of the channel estimates at data locations; however, some additional gain can be attained by averaging interpolated channel estimates using an averaging sliding window whose length is inversely proportional to the coherence bandwidth of the channel [2].

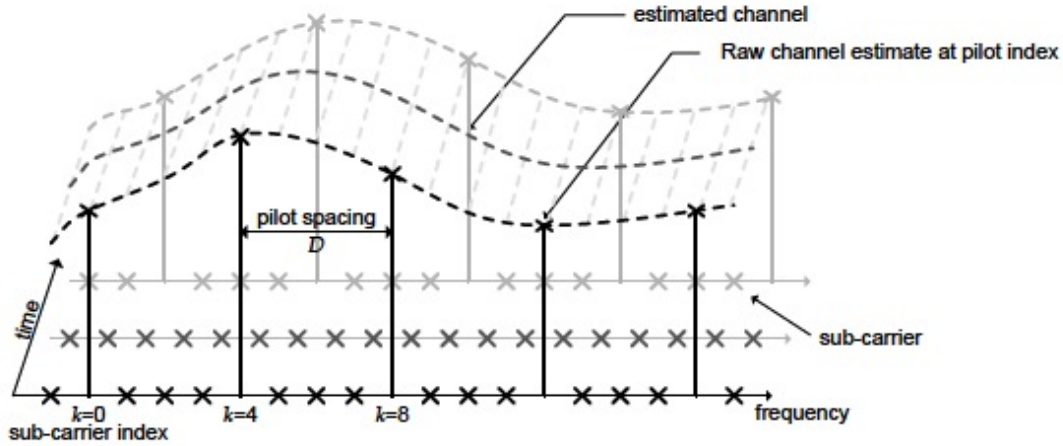


Figure 33: Frequency and time domain linear interpolation procedure for pilot-based channel estimation [2]

Figure 33 illustrates our frequency and time domain approach to perform channel estimation based on pilot subcarriers. To generate the raw channel estimate at pilot index (p, l) in the resource grid let,

$$Y_{(p,l)} = H_{(p,l)}S_{(p,l)} + N_{(p,l)} \quad (5.2)$$

represent the frequency-domain sample value at the p^{th} pilot at a given time index l where $S_{(p,l)}$ is the known pilot (or reference) symbol, $H_{(p,l)}$ is the channel response, which may or may not include any residual phase error from the RF hardware, and $N_{(p,l)}$ account for noise. So the raw channel estimate is constructed using the following operation,

$$\tilde{H}_{(p,l)} = Y_{(p,l)}S_{(p,l)}^* = H_{(p,l)} + N_{(p,l)}S_{(p,l)}^* \quad (5.3)$$

where $S_{(p,l)}S_{(p,l)}^* = 1$ (see section 6.10.1.1 in [20]). From equation (5.3) we generate each of the raw channel estimates at each pilot index and from there we carry on with

the frequency and time linear interpolation procedure described above to estimate the channel coefficient for the data.

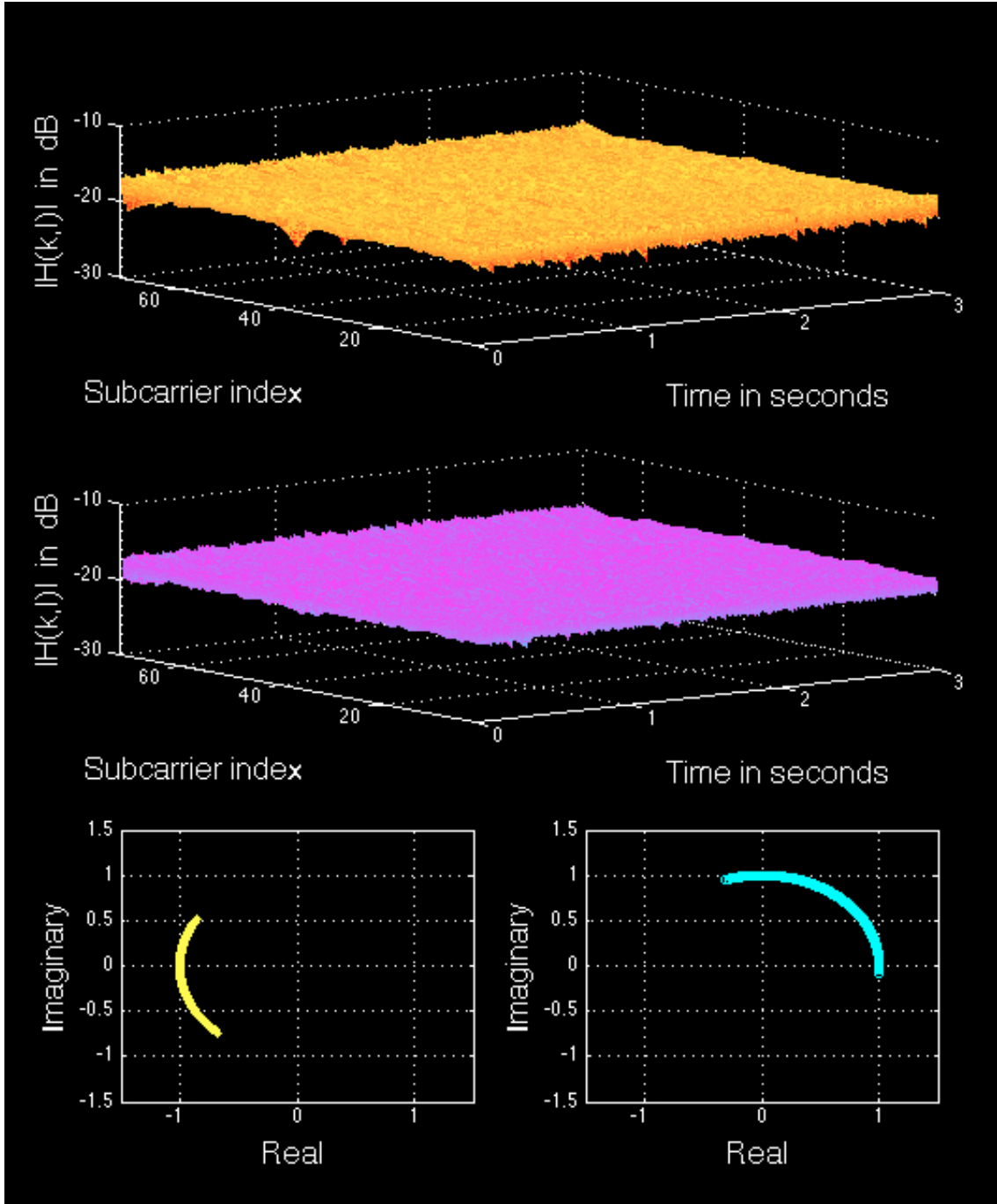


Figure 34: Channel coefficient estimates for tx antenna 1 and tx antenna 2 using reference pilots when the SNR is approximately 10 dB

The set of plots in Figure 34 show an example of the estimated channel coefficients, $\tilde{H}_{(k,l)}$, that the channel estimation module in Figure 32 will deliver to the

SFBC combiner. The channel coefficients were estimated using reference pilots while collecting BER measurements for data modulated using 16QAM with an approximated SNR of 10 dB. The next section will describe the methodology to compute the SNR. In this particular case, no averaging was used to reduce the effects of noise. The two plots at the top show the magnitude of the channel coefficient estimated on all 72 subcarriers for a period of about 3 seconds (or 300 FDD 10 millisecond subframes) and as expected, the channel response is relatively flat over the entire resource grid. The plot at the very top represents the magnitude channel estimates for transmit antenna 1 and the one below it represents the magnitude channel estimates for transmit antenna 2. The two plots at the bottom represent the complex exponential component $e^{j\angle\tilde{H}_{(k,l)}}$ in $\tilde{H}_{(k,l)}$. The plot on the left represents the complex exponential component for transmit antenna 1 while the one on the right corresponds to transmit antenna 2. The reason the phase component of $\tilde{H}_{(k,l)}$ is presented this way instead is to better illustrate the effects of noise and phase offset across all subcarriers in the frequency domain. In time, these effects remained basically the same.

Once the channel estimation coefficients reach the SFBC combiner, the resource elements containing payload data have already been extracted. It is now the SFBC combiner task to perform a set of operations similar to the ones described by equation 3.2, where two consecutive data subcarriers containing data from each of the transmission chains are combined to deliver one estimated data subcarrier from the pair. To illustrate this procedure, consider the following list of equations. From the resource grid, a pair of consecutive SFBC subcarriers with subcarrier indices k and $k + 1$ at column l in the time axis can be expressed in the following manner,

$$Y_{(k,l)} = H_{(k,l)}^{(1)} S_{(k,l)} - H_{(k,l)}^{(2)} S_{(k+1,l)}^* + N_{(k,l)} \quad (5.4a)$$

$$Y_{(k+1,l)} = H_{(k+1,l)}^{(1)} S_{(k+1,l)} + H_{(k+1,l)}^{(2)} S_{(k,l)}^* + N_{(k+1,l)} \quad (5.4b)$$

where $H^{(1)}$ and $H^{(2)}$ represent the actual channel coefficient for transmit antenna 1 and transmit antenna 2 respectively. It has been noted in [12], that in order for the combiner to work, the following criteria must hold, $H_{(k,l)}^{(1)} = H_{(k+1,l)}^{(1)}$ and $H_{(k,l)}^{(2)} = H_{(k+1,l)}^{(2)}$. Which is not such a tight requirement if the channel across two consecutive subcarriers is relatively flat. With these assumptions in mind, the equations in (5.4) can be rewritten to the ones below,

$$Y_{(k,l)} = H_{(k,l)}^{(1)} S_{(k,l)} - H_{(k,l)}^{(2)} S_{(k+1,l)}^* + N_{(k,l)} \quad (5.5a)$$

$$Y_{(k+1,l)} = H_{(k,l)}^{(1)} S_{(k+1,l)} + H_{(k,l)}^{(2)} S_{(k,l)}^* + N_{(k+1,l)} \quad (5.5b)$$

The combiner then uses $Y_{(k,l)}$, $Y_{(k+1,l)}$, and the channel coefficient estimates for transmit antenna 1 and transmit antenna 2 to get data subcarriers estimates $\tilde{S}_{(k,l)}$ and $\tilde{S}_{(k+1,l)}$ the following way,

$$\begin{aligned}
\tilde{S}_{(k,l)} &= Y_{(k,l)} \tilde{H}_{(k,l)}^{*(1)} + Y_{(k+1,l)}^* \tilde{H}_{(k,l)}^{(2)} \\
&= \left(H_{(k,l)}^{(1)} S_{(k,l)} - H_{(k,l)}^{(2)} S_{(k+1,l)}^* + N_{(k,l)} \right) \tilde{H}_{(k,l)}^{*(1)} + \\
&\quad \left(H_{(k,l)}^{(1)} S_{(k+1,l)} + H_{(k,l)}^{(2)} S_{(k,l)}^* + N_{(k+1,l)} \right)^* \tilde{H}_{(k,l)}^{(2)} \\
&= H_{(k,l)}^{(1)} \tilde{H}_{(k,l)}^{*(1)} S_{(k,l)} - H_{(k,l)}^{(2)} \tilde{H}_{(k,l)}^{*(1)} S_{(k+1,l)}^* + \tilde{H}_{(k,l)}^{*(1)} N_{(k,l)} + \\
&\quad H_{(k,l)}^{*(1)} \tilde{H}_{(k,l)}^{(2)} S_{(k+1,l)}^* + H_{(k,l)}^{*(2)} \tilde{H}_{(k,l)}^{(2)} S_{(k,l)} + \tilde{H}_{(k,l)}^{(2)} N_{(k+1,l)}^* \\
&= \left(|H_{(k,l)}^{(1)}|^2 + |H_{(k,l)}^{(2)}|^2 \right) S_{(k,l)} + \tilde{H}_{(k,l)}^{*(1)} N_{(k,l)} + \tilde{H}_{(k,l)}^{(2)} N_{(k+1,l)}^*
\end{aligned} \tag{5.6a}$$

$$\begin{aligned}
\tilde{S}_{(k+1,l)} &= -Y_{(k,l)}^* \tilde{H}_{(k,l)}^{(2)} + Y_{(k+1,l)} \tilde{H}_{(k,l)}^{*(1)} \\
&= - \left(H_{(k,l)}^{(1)} S_{(k,l)} - H_{(k,l)}^{(2)} S_{(k+1,l)}^* + N_{(k,l)} \right)^* \tilde{H}_{(k,l)}^{(2)} + \\
&\quad \left(H_{(k,l)}^{(1)} S_{(k+1,l)} + H_{(k,l)}^{(2)} S_{(k,l)}^* + N_{(k+1,l)} \right) \tilde{H}_{(k,l)}^{*(1)} \\
&= -H_{(k,l)}^{*(1)} \tilde{H}_{(k,l)}^{(2)} S_{(k,l)}^* + H_{(k,l)}^{*(2)} \tilde{H}_{(k,l)}^{(2)} S_{(k+1,l)} - \tilde{H}_{(k,l)}^{(2)} N_{(k,l)}^* \\
&\quad H_{(k,l)}^{(1)} \tilde{H}_{(k,l)}^{*(1)} S_{(k+1,l)} + H_{(k,l)}^{(2)} \tilde{H}_{(k,l)}^{*(1)} S_{(k,l)}^* + \tilde{H}_{(k,l)}^{*(1)} N_{(k+1,l)} \\
&= \left(|H_{(k,l)}^{(1)}|^2 + |H_{(k,l)}^{(2)}|^2 \right) S_{(k+1,l)} - \tilde{H}_{(k,l)}^{(2)} N_{(k,l)}^* + \tilde{H}_{(k,l)}^{*(1)} N_{(k+1,l)}
\end{aligned} \tag{5.6b}$$

the two equations in (5.6) yield the desired outcome provided that the channel coefficient estimates for transmit antenna 1 and transmit antenna 2 are fairly accurate. If not, $\tilde{S}_{(k,l)}$ will suffer ICI from $S_{(k+1,l)}$ and $\tilde{S}_{(k+1,l)}$ will be affected by $S_{(k,l)}$. Also, the combiner provides the role of a zero forcing equalizer, i.e. remove the channel effects, if we divide $\tilde{S}_{(k,l)} / (|H_{(k,l)}^{(1)}|^2 + |H_{(k,l)}^{(2)}|^2)$ and $\tilde{S}_{(k+1,l)} / (|H_{(k,l)}^{(1)}|^2 + |H_{(k,l)}^{(2)}|^2)$.

All data subcarriers estimates are then passed to an ML modulation detector which maps each estimated data subcarrier $\tilde{S}_{(k,l)}$ to one of the possible modulation symbols s_i based on the ML criteria,

$$\arg \min_{s_i} |\tilde{S}_{(k,l)} - s_i|^2 \tag{5.7}$$

5.3 BER Measurements

The BER measurements results in this section were computed by comparing the estimated symbols from the ML detector (converted to bits) against a set of bits generated using the same binary generator seed that the transmitter used to generate its own bits. Each BER point on the plots presented here was computed from the number of errors found on each FDD slot and accumulated over a period of about 10 seconds (or one thousand 10 millisecond FDD frames).

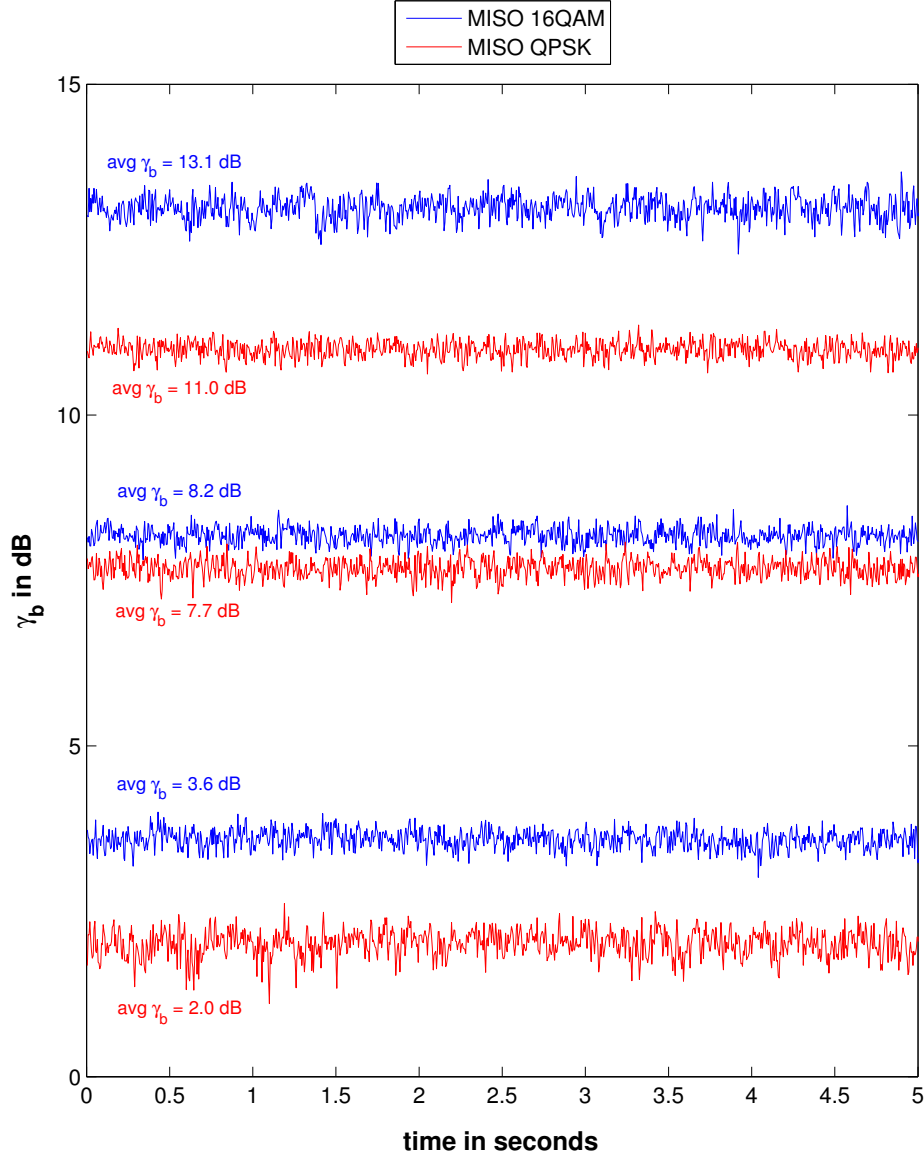


Figure 35: Instantaneous SNR, in terms of γ_b , captured over the first 5 seconds during the BER measurements

Similarly the SNR, which is represented by the average E_b/N_o or $\tilde{\gamma}_b$, was estimated by using the known symbols. So the average E_s/N_o was computed first and then E_s was related to E_b by $E_b \approx E_s/m$ where m is the number of bits per modulated symbol (i.e. 2 for QPSK and 4 for 16QAM) and $E_s = E\{|s_i|^2\} = 1$.

The noise component, N_o , was determined by computing $|s_i - \tilde{s}_i|^2$ where s_i is the known symbol and \tilde{s}_i is the estimated symbol provided by the ML detector. Again, the noise component was accumulated over an entire FDD slot and averaged in time.

The set of plots in Figure 35 provide the instantaneous SNR (represented in terms of γ_b) computed while collecting BER measurements. The plots show the first 5 seconds of each BER measurement run. The red plots show the instantaneous SNR computed while collecting the BER for the QPSK MISO case and the blue ones show the instantaneous SNR for the 16QAM MISO case. Each instantaneous SNR point on a plot corresponds to the accumulated SNR (both in frequency and time) in an FDD slot. The average SNR, $\tilde{\gamma}_b$, was determined by taking the average of all the instantaneous SNR points during the entire 10 second run.

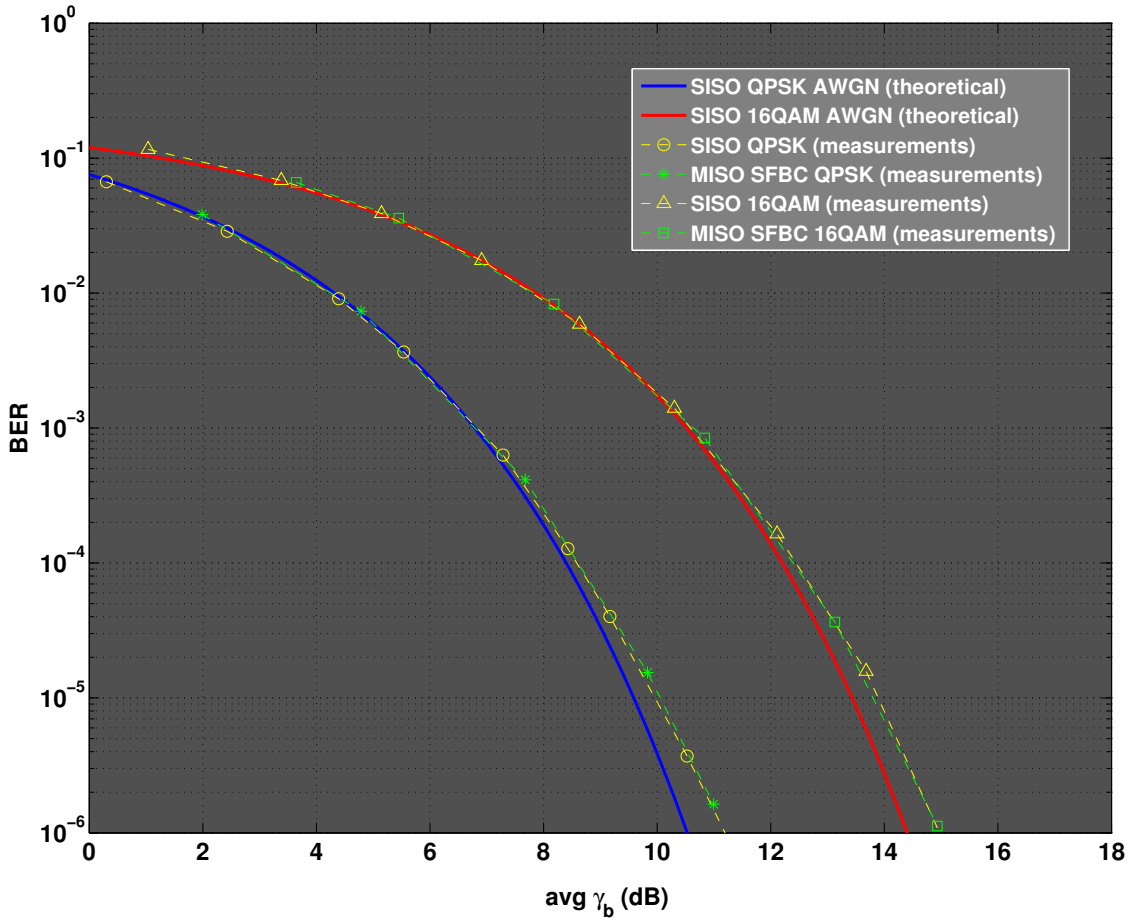


Figure 36: BER measurements results of the MISO system depicted in Figure 26

Figure 36 shows the BER curves used to validate our MISO setup inside the RF anechoic chamber. The x-axis provides the average SNR for each BER point computed. The solid blue and red curves represent theoretical AWGN curves for QPSK and 16QAM respectively. The yellow and green curves correspond to SISO and MISO measurements for each of the modulation schemes. In the MISO case, a 3 dB attenuator was attached to each of the SMA transmit antenna connectors in the USRP boxes. This was done so to keep the same transmit power in both the MISO and the SISO case.

The channel estimation process used to compute the BER measurements averaged out 10 FDD slots in order to reduce the error margin in the channel coefficients estimates. The averaging was done along pilot subcarriers in time but not along subcarriers in the frequency domain. With this channel estimation procedure, the green and yellow BER curves in Figure 36 show that there is an approximate 1 dB system loss at an error rate of 10^{-6} for the two modulation schemes in both the MISO and SISO case with respect to the theoretical AWGN BER curves. The most important characteristics about the plots in Figure 36 is that the SISO and MISO set of measurements exhibit the same BER performance. This condition is expected since antenna diversity techniques do not improve the error rate in non-fading scenarios.

6 Multipath Channel BER Measurements



Figure 37: MISO multipath setup inside Comnet Laboratory

The BER performance benefits of transmit antenna diversity techniques rely heavily on the condition that a rich and uncorrelated multipath fading channel exist for each of the transmission chains. So in order to test the performance of the MISO system in a multipath fading environment, we've created the setup shown in Figures 37 and 38. The test was conducted inside the Comnet Laboratory at Aalto Department of Communications and Networking. The distance between each transmit antenna and the receive antenna was approximately three meters, and the distance separating each transmit antennas was approximately 1.5 meters. To simulate time-varying multipath fading effects, we've placed a vinyl record player in front of each transmit antenna (see the sketch of Figure 38). Each record player held a rectangular piece of metal rotating at 33 revolutions-per-minute (rpm) for antenna 1 and 45 rpm for antenna 2. Additionally, a big metallic plate was placed behind the transmit antennas and the receive antenna (see the pictures on the left side of Figure 38) to emphasise the scattering effects during the measurements. The BER measurements presented in this chapter correspond to the same bandwidth configuration and normal CP used previously but the centre frequency was moved up to 2.48 GHz in order to minimise the interference effects from/to users in the upper bands of the WiFi spectrum. Only 16QAM was used in this measurements.

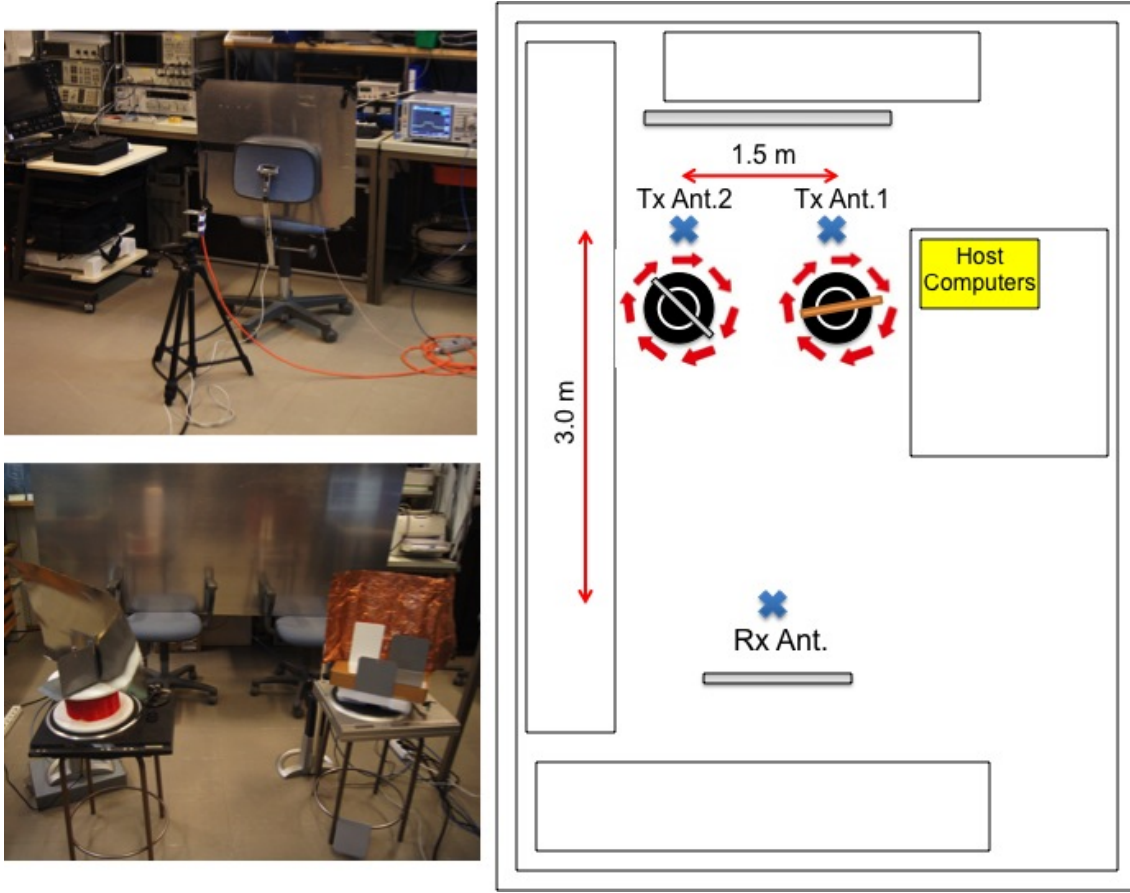


Figure 38: The picture on the right hand shows a sketch of the setup used during the measurements. The pictures on the left show the transmit antennas with the rotating metallic sheets (bottom) and the receive antenna (top)

6.1 Time-Selective Multipath Fading Scenario

The multipath fading scenario experienced by each of the transmission chains in this setup offers great time-selective fading effects yet the fading across subcarriers in the frequency domain is expected to be relatively flat (see Figure 39). The time-selective fading effects come primarily from the fact that the metallic sheets in front of the transmit antennas block the line-of-sight periodically as they spin around. The flat fading effects in frequency are due to the fact that the CP appended to each OFDM symbol provides protection against ISI between adjacent OFDM symbols in the time domain. ISI between adjacent OFDM symbols in the time domain is perhaps the main contributor of frequency-selective fading in OFDM systems when the rms delay spread of the channel is larger than the CP length.

To better understand the CP protection against ISI in our scenario, let us take a closer look at the CP appended to each OFDM symbol when the channel bandwidth configuration is 1.4 MHz. Table 3 defines the CP length of the first OFDM symbol in a slot to be 10 samples and 9 samples for the rest of the OFDM symbols in the slot.

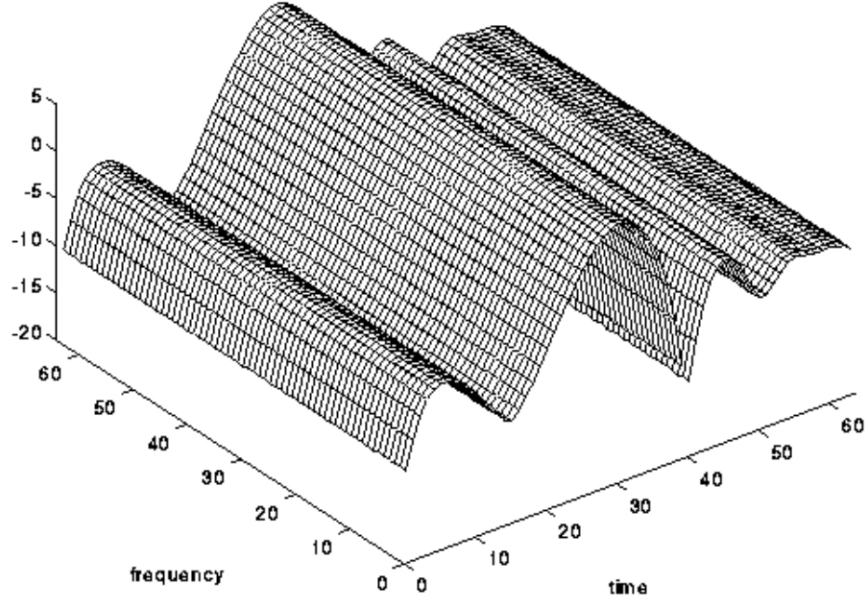


Figure 39: Rapidly fading time-selective channel [3]

So the CP offers an approximate $5 \mu\text{seconds}$ protection against ISI from adjacent OFDM symbols in the time domain. The rms delay spread of an indoor channel is typically around a few tenths of nanoseconds [32, 33, 34, 35, 36]. Therefore, it is unlikely that ISI will occur in this configuration setup.

Figure 40 shows the absolute value of the channel coefficient estimates, $|\tilde{H}_{(k,l)}|$, for each of the transmission chains when the average SNR of the 16QAM modulated data is approximately 12 dB. Once again, the channel coefficients are estimated from pilot subcarrier symbols. The plot at the very top (yellow hue) represents the $|\tilde{H}_{(k,l)}|$ for transmit antenna 1 and the one below it (blue hue), corresponds to transmit antenna 2. As expected, the subcarriers along the frequency axis exhibit relatively flat fading while time-selective fading is clearly present in the time domain. The plot at the very bottom depicts the magnitude profile of the channel coefficient estimates for the two transmission chains along the time axis. The SFBC combiner takes the channel coefficient estimates for each transmit antenna and then provides an estimate of the data based on the combined magnitude of the channel coefficients. This effect can be seen from the two equations in (5.6), where data symbol estimates, $\tilde{S}_{(k,l)}$ and $\tilde{S}_{(k+1,l)}$, are directly proportional to $(|H_{(k,l)}^{(1)}|^2 + |H_{(k,l)}^{(2)}|^2)$. So if channel coefficient $H_{(k,l)}^{(1)}$ experiences a period of deep fade, $H_{(k,l)}^{(2)}$ could potentially compensate for the fading of $H_{(k,l)}^{(1)}$ if it doesn't go through similar deep fading. Similarly, $H_{(k,l)}^{(1)}$ could do the same for $H_{(k,l)}^{(2)}$. This precise effect is the main benefit of using transmit antenna diversity techniques to combat fading in wireless communications.

The phase components of $\tilde{H}_{(k,l)}^{(1)}$ and $\tilde{H}_{(k,l)}^{(2)}$ measured in this setup are constantly changing and it is difficult to visualise their changes in frequency and time. However,

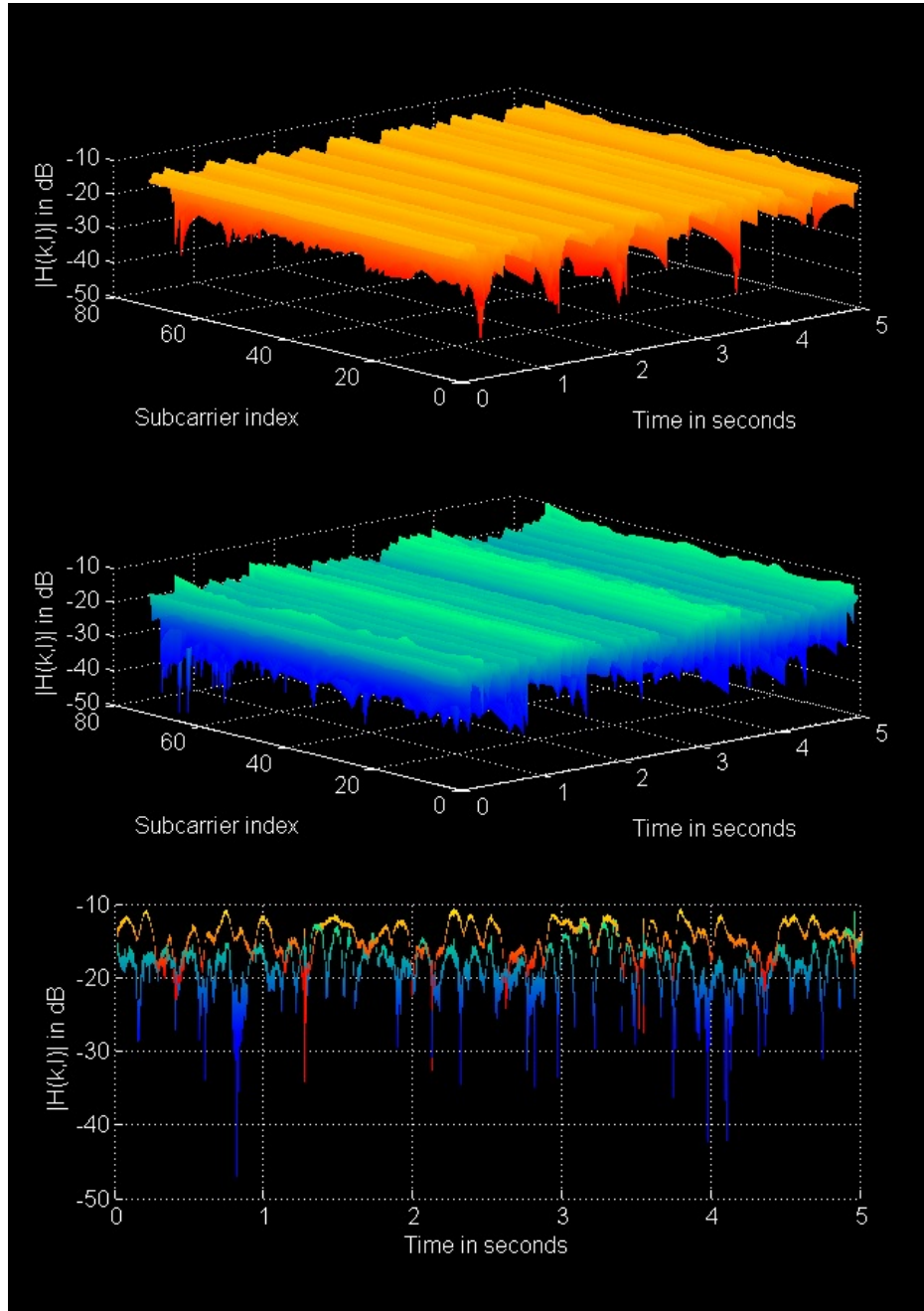


Figure 40: Magnitude of the channel coefficient estimates for tx antenna 1 and tx antenna 2 when the average SNR of the data is approximately 12 dB

if the channel estimation process is accurate, the combiner can properly compensate for the phase offset due to the channel experienced by transmit antenna 1 and transmit antenna 2.

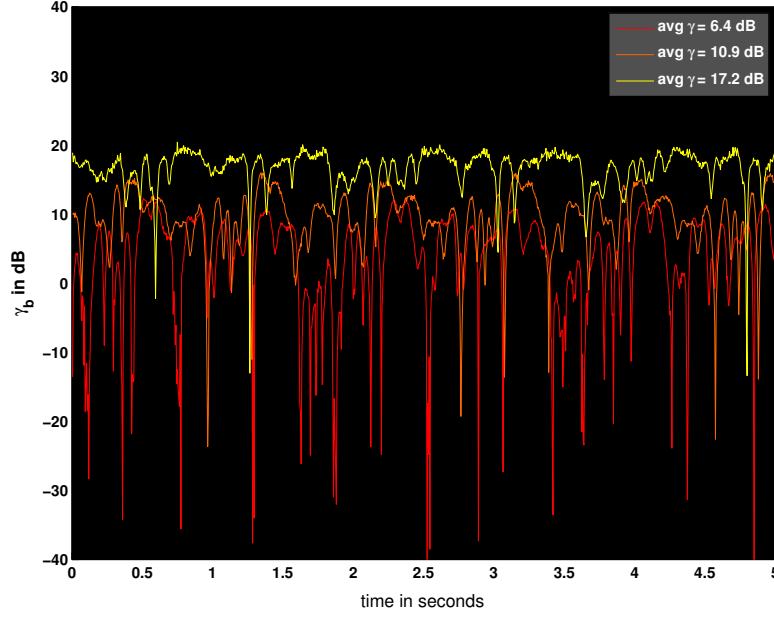


Figure 41: Instantaneous SNR, in terms of γ_b , for the SISO case using transmit antenna 1

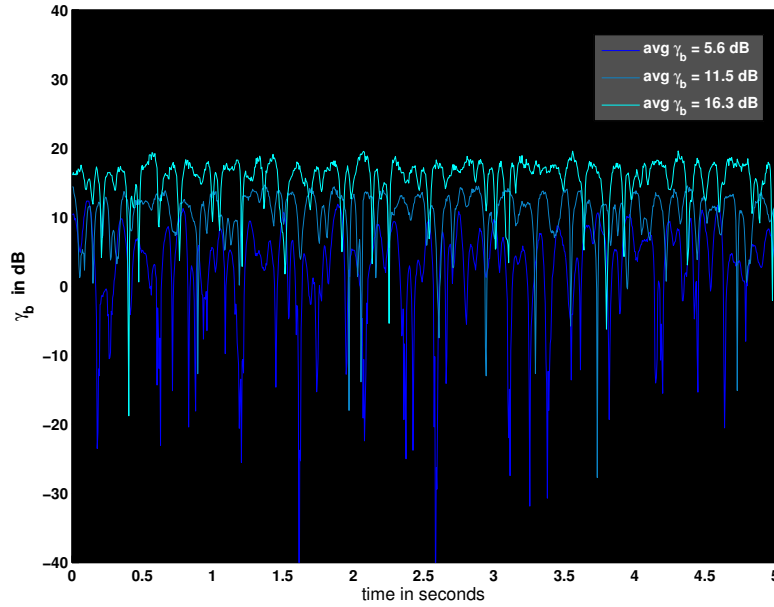


Figure 42: Instantaneous SNR, in terms of γ_b , for the SISO case using transmit antenna 2

6.2 Instantaneous and Average SNR Measurements

Extended periods of deep fading observed in the channel coefficient estimates along the time domain translate to low SNR values (per subcarrier symbol) accumulated over the duration of an FDD slot. As described in the previous chapter, we refer to

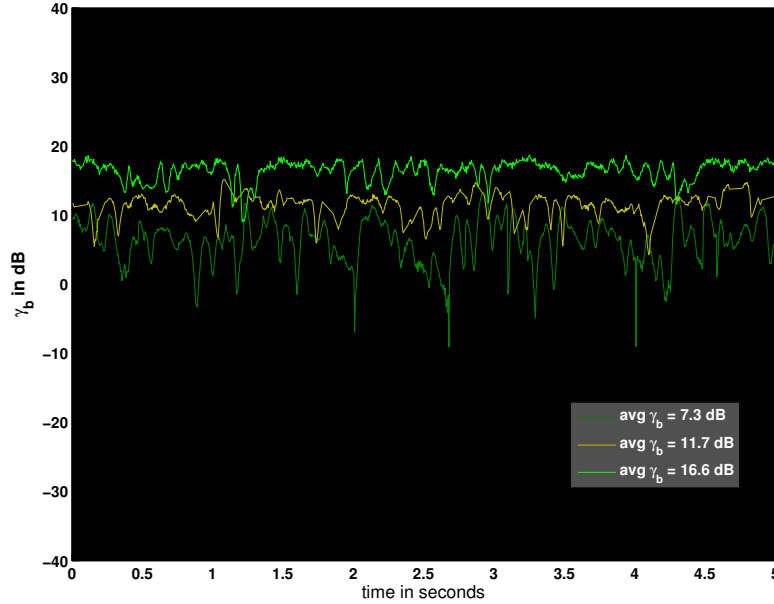


Figure 43: Instantaneous SNR, in terms of γ_b , for the MISO case

these accumulated SNR values as the instantaneous SNR associated to an FDD slot. Figures 41 and 42 show the instantaneous SNR, in terms of γ_b , observed while computing BER measurements for the SISO case. Figure 41 depicts the instantaneous SNR for the SISO transmission chain using antenna 1 and Figure 42 corresponds to the SISO transmission using transmit antenna 2. Each plot showing the instantaneous SNR in the figures is then averaged over a period of about 10 seconds to get an average SNR value. This average SNR value corresponds to one BER point in Figure 44.

The instantaneous SNR plots for the MISO case are shown in Figure 43. Each plot also corresponds to an average SNR value computed over a period of about 10 seconds. An important characteristic about the plots in this figure is that the fading effects are not as pronounced as the ones seen in Figures 41 and 42. Again, this is to be expected since the SFBC combiner smooths out the fading effects by combining the channel responses from the two transmission chains.

6.3 BER Measurements

Figure 44 shows the BER measurements computed using the multipath setup configuration described above. The red and magenta curves in the figure are used as a reference, and they correspond to theoretical BER curves for SISO 16QAM modulation in AWGN channel and Rayleigh, flat-fading channel respectively. The green, yellow, and cyan curves correspond to actual BER measurement results. To generate these set of results, FDD slot averaging of channel coefficient estimates was not

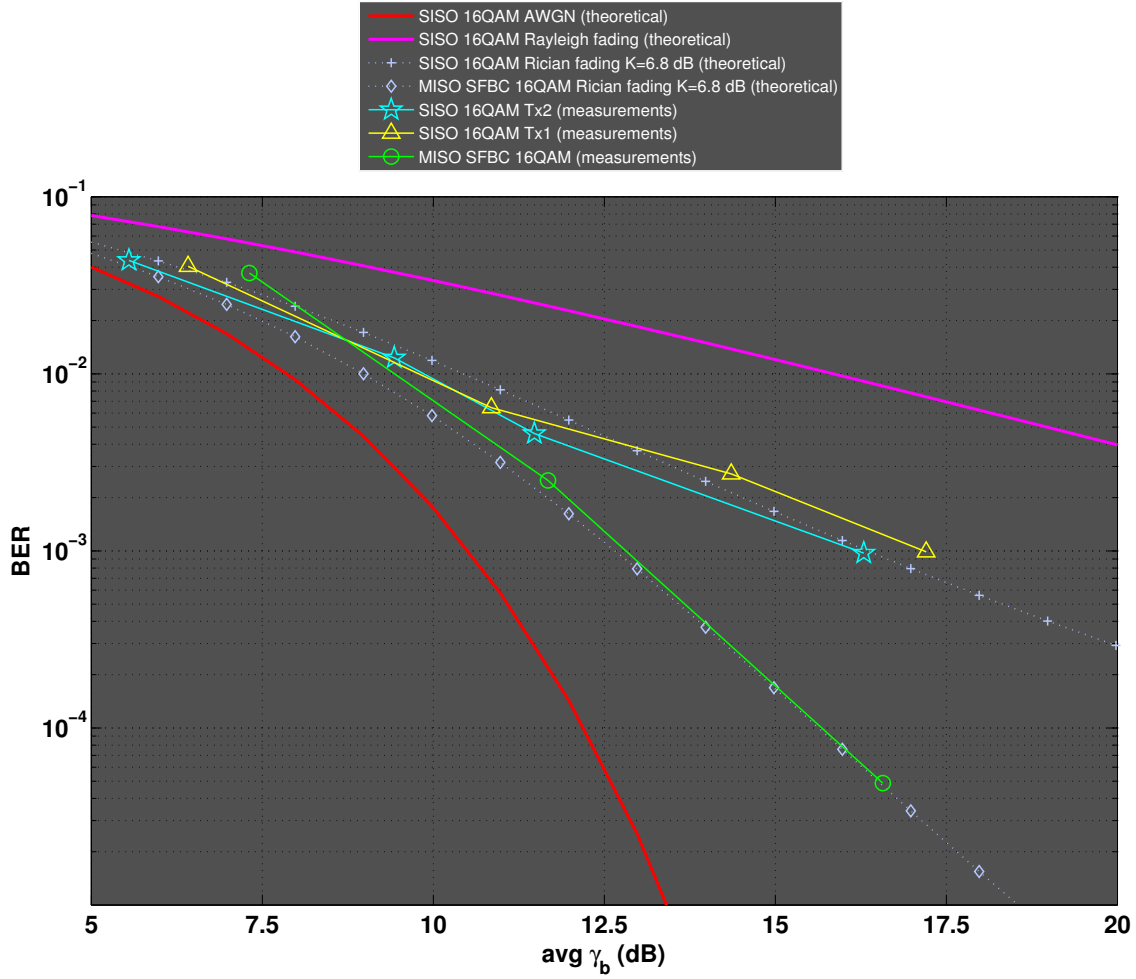


Figure 44: BER measurements results of the multipath fading setup depicted in Figures 37 and 38

necessary since it offered no additional BER improvement. The yellow and cyan curves represent the BER measurement results for the SISO case using transmit antenna 1 and transmit antenna 2 respectively. The green curve represents the BER for the MISO case. Although only three BER points are provided in the figure for the MISO link and four BER points for each SISO case, (with the available data) it is clear that the error rate improvement of the multi-antenna system initiates when the average SNR is above 12 dB.

As mentioned in Chapter 3, an important parameter that quantifies the error rate performance advantage of a multi-antenna system versus a SISO system is the diversity gain factor . To get an insight on the diversity gain achieved by the MISO system used in our measurements, we've made the assumption that the fading environment created with our setup somewhat resembles the Rician flat-fading channel in the time-domain since a periodic, strong line-of-sight multipath component may exist as the metallic sheets in front of each transmit antenna spin

around. We found that the measured BER points somewhat fit the two purple curves showing the theoretical BER curves for Rician fading with $K = 6.8$ dB for both the SISO and the MISO SFBC case. A diversity gain can be observed when comparing the two curves.

7 Concluding Remarks

SDRs offer flexibility and cost-efficiency in wireless system design and implementation. A wireless device can be modified and harnessed to target a specific wireless technology by implementing most or all of the physical layer functionalities entirely in software and a hardware platform that can accommodate a broad frequency spectrum usage and extensive bandwidth.

In this thesis we have demonstrated a simple LTE FDD testbed that utilizes transmit diversity techniques. We've provided a detailed description of the downlink transmission procedure in Chapter 3 and provided BER measurement results inside an RF Anechoic chamber in Chapter 5, where the wireless channel is essentially multipath fading free. The last chapter, Chapter 6, shows the BER measurements results generated using this platform in a multipath-induced environment created in the lab.

To generate the BER measurements results provided in this document, we have synchronized each of the USRP boxes in the transmission side with the same external reference clock. So we can expect synchronous transmission delivery at the receiving end thus simplifying the LTE decoding procedure. Our next research goal is to extend the capabilities of the LTE MISO testbed to handle multiple transmission signals coming from a set of geographically distributed USRP transmitters. Consequently, each transmitter will be driven by its own independent clock to drive sampling timing and carrier frequency up/down conversion; therefore, the synchronisation procedure becomes more elaborate.

References

- [1] 3rd Generation Partnership Project, *3GPP TS 36.101 v11.0.0 - 3rd Generation Partnership Project; Technical Specification Group Radio Access Network; Evolved Universal Terrestrial Radio Access (E-UTRA); User Equipment (UE) Radio Transmission and Reception (Release 11)*, 3rd Generation Partnership Project Std., 2012. [Online]. Available: <http://www.3gpp.org/ftp/Specs/html-info/36101.htm>
- [2] M. S. Akram, “Pilot-based channel estimation in ofdm systems,” master thesis, Modem System Design group at Nokia and Technical University of Denmark, 2007.
- [3] (2013, june) Samples of a rayleigh-fading multipath channel @ONLINE. [Online]. Available: <http://www.wirelesscommunication.nl/reference/chaptr03/channel.htm>
- [4] J. G. Proakis, *Digital Communications*. McGraw Hill Higher Education, 2000.
- [5] A. Goldsmith, *Wireless Communications*. Cambridge University Press, 2005.
- [6] J. D. Parsons, *The Mobile Radio Propagation Channel, 2nd Edition*. Wiley, 2000.
- [7] A. Molisch, *Wireless communications*. Chichester, West Sussex, U.K: Wiley IEEE, 2011.
- [8] T. S. Rappaport, *Wireless Communications: Principles and Practice (2nd Edition)*. Prentice Hall, 2002.
- [9] D. Tse and P. Viswanath, *Fundamentals of Wireless Communication*. Cambridge University Press, 2005.
- [10] B. Sklar, “Rayleigh fading channels in mobile digital communication systems .i. characterization,” *Communications Magazine, IEEE*, vol. 35, no. 7, pp. 90–100, Jul 1997.
- [11] M. K. Simon and M.-S. Alouini, *Digital Communication over Fading Channels (Wiley Series in Telecommunications and Signal Processing)*. Wiley-IEEE Press, 2004.
- [12] S. Alamouti, “A simple transmit diversity technique for wireless communications,” *Selected Areas in Communications, IEEE Journal on*, vol. 16, no. 8, pp. 1451–1458, oct 1998.
- [13] “3gpp global initiative,” <http://www.3gpp.org>, accessed: 2016-06-01.
- [14] C. Cox, *An introduction to LTE LTE, LTE-advanced, SAE, and 4G mobile communications*. Hoboken, NJ: John Wiley & Sons, 2012.

- [15] H. Holma, *LTE for UMTS : OFDMA and SC-FDMA based radio access*. Chichester, U.K: Wiley, 2009.
- [16] C. Johnson, *Long term evolution in bullets*. Northampton, England: Johnson, 2012.
- [17] G. Roche, *LTE-advanced and next generation wireless networks channel modelling and propagation*. Chichester, West Sussex, U.K: Wiley, 2013.
- [18] D. Astely, E. Dahlman, A. Furuskar, Y. Jading, M. Lindstrom, and S. Parkvall, "Lte: the evolution of mobile broadband," *IEEE Communications Magazine*, vol. 47, no. 4, pp. 44–51, April 2009.
- [19] Ettus-Research. Application note: Synchronization and mimo capability with usrp devices. [Online]. Available: http://www.ettus.com/content/files/kb/mimo_and_sync_with_usrp.pdf
- [20] 3rd Generation Partnership Project, *3GPP TS 36.211 v10.0.5 - 3rd Generation Partnership Project; Technical Specification Group Radio Access Network; Evolved Universal Terrestrial Radio Access (E-UTRA); Physical Channels and Modulation (Release 10)*, 3rd Generation Partnership Project Std., 2012. [Online]. Available: <http://www.3gpp.org/ftp/Specs/html-info/36211.htm>
- [21] E. Dahlman, S. Parkvall, J. Skold, and P. Beming, *3G Evolution, Second Edition: HSPA and LTE for Mobile Broadband*. Academic Press, 2008.
- [22] 3rd Generation Partnership Project, *3GPP TS 36.213 v10.6.0 - 3rd Generation Partnership Project; Technical Specification Group Radio Access Network; Evolved Universal Terrestrial Radio Access (E-UTRA); Physical Layer Procedures (Release 10)*, 3rd Generation Partnership Project Std., 2012. [Online]. Available: <http://www.3gpp.org/ftp/Specs/html-info/36213.htm>
- [23] —, "3gpp tr 25.892 v6.0.0 - 3rd generation partnership project; technical specification group radio access network; feasibility study for orthogonal frequency division multiplexing (ofdm) for utran enhancement (release 6)," 3rd Generation Partnership Project, Tech. Rep., 2004. [Online]. Available: <http://www.3gpp.org/ftp/Specs/html-info/25892.htm>
- [24] J. Cooley and J. Turkey, "An algorithm for the machine calculation of complex fourier series," *Mathematics of Computation*, vol. 19, no. 90, pp. 297–301, apr 1965.
- [25] D. Chu, "Polyphase codes with good periodic correlation properties (corresp.)," *Information Theory, IEEE Transactions on*, vol. 18, no. 4, pp. 531 – 532, jul 1972.
- [26] A. J. Viterbi, *CDMA: Principles of Spread Spectrum Communication*. Addison-Wesley, 1995.

- [27] (2013, june) Usrc2 general frequently-asked-questions @ONLINE. [Online]. Available: <http://gnuradio.org/redmine/projects/gnuradio/wiki/USRP2GenFAQ>
- [28] Q. Wang, C. Mehlh hrer, and M. Rupp, "Carrier frequency synchronization in the downlink of 3gpp lte," in *Personal Indoor and Mobile Radio Communications (PIMRC), 2010 IEEE 21st International Symposium on*, 2010, pp. 939–944.
- [29] (2013, june) Usrc n200 datasheet @ONLINE. [Online]. Available: https://www.ettus.com/content/files/07495_Ettus_N200-210_DS_Flyer_HR.pdf
- [30] M. Ibnkahla, *Signal Processing for Mobile Communications Handbook*. CRC Press, 2005.
- [31] J. Hou and J. Liu, "A novel channel estimation algorithm for 3gpp lte downlink system using joint time-frequency two-dimensional iterative wiener filter," in *Communication Technology (ICCT), 2010 12th IEEE International Conference on*, 2010, pp. 289–292.
- [32] H. Hashemi and D. Tholl, "Analysis of the rms delay spread of indoor radio propagation channels," in *Communications, 1992. ICC '92, Conference record, SUPERCOMM/ICC '92, Discovering a New World of Communications., IEEE International Conference on*, 1992, pp. 875–881 vol.2.
- [33] H. MacLeod, C. Loadman, and Z. Chen, "Experimental studies of the 2.4-ghz ism wireless indoor channel," in *Communication Networks and Services Research Conference, 2005. Proceedings of the 3rd Annual*, 2005, pp. 63–68.
- [34] G. Durgin, V. Kukshya, and T. Rappaport, "Wideband measurements of angle and delay dispersion for outdoor and indoor peer-to-peer radio channels at 1920 mhz," *Antennas and Propagation, IEEE Transactions on*, vol. 51, no. 5, pp. 936–944, 2003.
- [35] P. Nobles and F. Halsall, "Delay spread and received power measurements within a building at 2 ghz, 5 ghz and 17 ghz," in *Antennas and Propagation, Tenth International Conference on (Conf. Publ. No. 436)*, vol. 2, 1997, pp. 319–324 vol.2.
- [36] M. Varela and M. Sanchez, "Rms delay and coherence bandwidth measurements in indoor radio channels in the uhf band," *Vehicular Technology, IEEE Transactions on*, vol. 50, no. 2, pp. 515–525, 2001.